UNIVERSITY OF CALIFORNIA SAN DEIGO

Silicon Photonic Devices Enabling High-Speed Low-Energy Optical Interconnect

A dissertation submitted in partial satisfaction of the
requirements for the degree Doctor of Philosophy

in

Electrical Engineering (Photonics)

by

Jin Zhang

Committee in charge:

Stojan Radic, Chair
Joseph E. Ford
Miroslav Krstic
Bill Ping-Piu Kuo
Zhaowei Liu
George C. Papen

2020

The Dissertation of Jin Zhang is approved, and it is acceptable in quality and form for publication on microfilm and electronically:

_____

_____

_____

_____

_____

_____

Chair

University of California San Diego

2020

DEDICATION

To my family and friends

for their love and support

TABLE OF CONTENTS

LIST OF FIGURES

LIST OF TABLES

LIST OF ABBREVIATIONS

SiP	Silicon Photonics
APD	Avalanche Photodetector/Photodiode
PAM	Pulse Amplitude Modulation
QAM	Quadrature Amplitude Modulation
AI	Artificial Intelligence
IoT	Internet of Things
CAGR	Compound Annual Growth Rate
SOI	Silicon-on-Insulator
CMOS	Complementary Metal-Oxide-Semiconductor
MUX	Multiplexer
DEMUX	Demultiplexer
WDM	Wavelength Division Multiplexing
TPA	Two Photon Absorption
FCA	Free Carrier Absorption
MZ	Mach-Zehnder
MZI	Mach-Zehnder interferometer
HOM	High Order Modulation
SOA	Semiconductor Optical Amplifier
SE	Spectral Efficiency
ArMMI	Arbitrary Ratio Multimode Interference
FDTD	Finite Difference Time Domain
GI	General Interference

PI	Paired Interference
DC	Direct Current
EO	Electro Optical
PIC	Photonic Integrated Circuits
BOX	Buried Oxide
MPW	Multi-Project Wafer
ASE	Amplified Spontaneous Emission
GC	Grating Coupler
SNR	Signal Noise Ratio
TIA	Transimpedance Amplifier
RCE	Resonant Cavity Enhanced
IME	Institute of Microelectronics
SEM	Scanning Electron Microscope
MCW	Multi-Contact Wedge
PC	Polarization Controller
MZM	Mach-Zehnder Modulator
EDFA	Erbium Doped Fiber Amplifier
VOA	Variable Optical Attenuator
VNA	Vector Network Analyzer
ISS	Impedance Standard Substrates
SOLT	Short-Open-Load-Thru
DCA	Digital Communication Analyzer
ESA	Electrical Signal Analyzer

LNA	Low Noise Amplifier
PSD	Power Spectral Density
NF	Noise Figure
DAC	Digital-to-Analog Converter
OMA	Optical Modulation Amplitude
UI	Unit Interval
DSP	Digital Signal Processing
FEC	Forward Error Correction
BER	Bit Error Ratio
LO	Local Oscillator
IMDD	Intensity-Modulation-Direct-Detection
CD	Chromatic Dispersion
PMD	Polarization Mode Dispersion
IF	Intermediate Frequency
RTO	Real Time Oscilloscope
OSNR	Optical Signal-to-Noise Ratio
RIN	Relative Intensity Noise
ISI	Inter-Symbol Interference
OSA	Optical Spectrum Analyzer
LMS	Least-Mean-Square
HDFEC	Hard Decision Forward Error-Correction
SACM	Separate-Absorption-Charge-Multiplication
CR	Coupling Ratio

ER	Extinction Ratio
FPM	Four-Photon Mixing
HNLF	Highly Nonlinear Fiber
FOM	Figure of Merit
SPM	Self-Phase Modulation
XPM	Cross-Phase Modulation
NFOM	Nonlinear Figure of Merit
NLSE	Nonlinear Schrödinger Equation
FFT	Finite-Fourier-Transform
FCD	Free Carrier Dispersion
RMS	Root Mean Square
PC	Phase Conjugation
MI	Modulation Instability
BS	Bragg Scattering
ITLA	Integrated Tunable Laser
BPF	Band Pass Filter
RIE	Reactive-Ion Etching
EDA	Electronic Design Automation
DRC	Design Rule Checks
EME	Eigenmode Expansion
PRBS	Pseudorandom Bit Sequence

ACKNOWLEDGEMENTS

First and foremost, I would like to express my deepest gratitude to my advisor, Professor Stojan Radic, for his support, guidance, trust, and understanding. He offers me the freedom to explore on my research without rushing me for the results. He motivates me into research work with his own dedicated work passion. No matter how early I make it to the lab, he is always already in his office working. He generously supports all the scientific and technical conferences I attend. His attitude and qualities, both personally and professionally, have taught me a lot and help me in an immeasurable way. Besides, I would like to thank all my committee members: Professor Joseph Ford, Professor Miroslav Krstic, Professor Zhaowei Liu, Professor George Papen, and Doctor Bill Ping-Piu Kuo, for their constructive discussions and contributions into this dissertation.

I would like to express my especial gratitude to Dr. Bill Ping-Piu Kuo, one of the most talented and knowledgeable researchers I have ever encountered, for his insight on scientific topics and tremendous help with my research work. Whenever I want to discuss with him my research progress and problems, he would make the time for me no matter how busy he is. His openness to discussion and in-depth knowledge sharing help me make steady improvements on my projects.

I would like to thank all my colleagues in our lab, who not only provide valuable help on my research but also enlighten my daily life. Many thanks to Dr. Ana Pejkic for her patient help in my early multicast and supercontinuum generation experiment. She gives me a lot of knowledge on operation of the lab equipment. Dr. Liangshun Han, with his extensive knowledge and focused hardworking style, provides me valuable help on many aspects. It is such a pleasure to discuss with him from time to time about either the

general technology or a specific problem I encounter. During my coherent detection experiments, Dr. Nikola Alic and Dr Eduardo Temprana provide valuable suggestions and help on specific DSP functionalities, which I feel sincere gratitude for. Along this long journey, I have received countless help from all the past and present members of the lab: Dr. Lan Liu, Dr. Daniel Esman, Dr. Kevin Young, Huan Hu, Motohiko Eto, Elham Serahati, and Jason Leng. I would like to thank all of them for their discussions and encouragements.

I would like to express my deepest love and gratefulness to my family – my father Jifa Zhang, mother Guomin Ge, and my brother Ce Zhang, for their unconditional love and supports for all my decisions in my life. It is their love and encouragement that gives me the continuous strength when I feel frustrated.

Chapter 3, in part, is a reprint of the material as it appears in 2018 Conference on Lasers and Electro-Optics (CLEO), pp. 1-2. IEEE, 2018, titled "Arbitrary Ratio, Wavelength-insensitive 2× 2 MMI Coupler in SOI with Enhanced Fabrication Tolerance", by Jin Zhang, Liangshun Han, Bill Ping-Piu Kuo, and Stojan Radic. Chapter 3 also contains in part materials accepted for publication as it may appear in the IEEE/OSA Journal of Lightwave Technology, titled "Broadband Angled Arbitrary Ratio MMI Couplers in SOI with Enhanced Fabrication Tolerance", by Jin Zhang, Liangshun Han, Bill P.-P. Kuo, and Stojan Radic. The dissertation author was the primary investigator, and the primary author of these articles.

Chapter 4, in part, is a reprint of the material as it appears in Conference on Lasers and Electro-Optics, OSA Technical Digest (Optical Society of America, 2020), paper STh3O.2, titled "High-Speed Low-Voltage Waveguide-Integrated Ge-on-Si Avalanche

Photodiodes", by Jin Zhang, Ana Pejkic, Bill Ping-Piu Kuo, and Stojan Radic. Chapter 4 also contains in part materials accepted for publication as it may appear in the IEEE/OSA Optics Express, titled "64Gbs PAM4 and 160Gbs 16QAM Reception Using Low-Voltage Si-Ge Waveguide-Integrated APD", by Jin Zhang, Bill P.-P. Kuo, and Stojan Radic. The dissertation author was the primary investigator, and the primary author of these articles.

Chapter 5, in part, is a reprint of the material as it appears in Asia Communications and Photonics Conference, pp. ATh2H-5. Optical Society of America, 2016, titled "Wavelength multicasting of 4/16QAM channel in a dual-pump two-stage silicon mixer", by Jin Zhang, E. Temprana, BP-P. Kuo, N. Alic, and S. Radic. The dissertation author was the primary investigator, and the primary author of this article.

VITA

2014 Bachelor of Science, Optical Engineering, Zhejiang University, China

2017 Master of Science, Electrical Engineering (Photonics), University of California San Diego, USA

2020 Doctor of Philosophy, Electrical Engineering (Photonics), University of California San Diego, USA

PUBLICATIONS

Journal articles:

Jin Zhang, Bill P.-P. Kuo, and Stojan Radic, "64Gbs PAM4 and 40GBaud 16QAM Modulation for a Low-Voltage Si-Ge Waveguide APD." Optics Express, 2020.

Jin Zhang, Liangshun Han, Bill P.-P. Kuo, and Stojan Radic, "Broadband Angled Arbitrary Ratio MMI Couplers in SOI with Enhanced Fabrication Tolerance." Journal of lightwave technology, 2020.

Conference proceedings:

Jin Zhang, Ana Pejkic, Bill Ping-Piu Kuo, and Stojan Radic. "High-Speed Low-Voltage Waveguide-Integrated Ge-on-Si Avalanche Photodiodes." in Conference on Lasers and Electro-Optics, OSA Technical Digest (Optical Society of America, 2020), paper STh3O.2.

Jin Zhang, Liangshun Han, Bill Ping-Piu Kuo, and Stojan Radic. "Arbitrary Ratio, Wavelength-insensitive 2× 2 MMI Coupler in SOI with Enhanced Fabrication Tolerance." In 2018 Conference on Lasers and Electro-Optics (CLEO), pp. 1-2. IEEE, 2018.

Jin Zhang, E. Temprana, BP-P. Kuo, N. Alic, and S. Radic. "Wavelength multicasting of 4/16QAM channel in a dual-pump two-stage silicon mixer." In Asia Communications and Photonics Conference, pp. ATh2H-5. Optical Society of America, 2016.

Han, Liangshun, Bill P-P. Kuo, Motohiko Eto, Ana Pejkic, **Jin Zhang**, Nikola Alic, and Stojan Radic. "Silicon Photonic 50GHz Wavelength (De) Multiplexer with Low Crosstalk and Flat Passband." In CLEO: Science and Innovations, pp. STu4B-3. Optical Society of America, 2018.

ABSTRACT OF THE DISSERTATION

Silicon Photonic Devices Enabling High-Speed Low-Energy Optical Interconnect

by

Jin Zhang

Doctor of Philosophy in Electrical Engineering (Photonics)

University of California San Diego, 2020

Professor Stojan Radic, Chair

The exponential growth in data center IP traffic entails rapidly evolving standards and optical transceiver solutions. The 200GbE and 400GbE standards were approved by the IEEE task force in 2017. Even higher speeds above 800GbE, 1.0TbE, and even 1.6TbE are forecasted to become standards a couple of years from now. To cope with the enormous

aggregated data rate demands, highly parallel pluggable optical transceiver modules based on silicon photonics technology have been proved to be the platform of choice due to their cost effectiveness and high yield, simultaneously conditioned with tremendous challenges in practical and low-power developments for the data center space.

This dissertation work explores possible solutions in three aspects. Wavelength multiplexing utilizing the nonlinear properties of the silicon waveguides is explored and experimentally demonstrated to be a valid solution to enable integrated multiple parallel wavelengths in SiP platform. Besides, wavelength and fabrication insensitive arbitrary ratio multimode interference couplers are proposed and demonstrated, enabling the design of broadband wavelength (de-)multiplexing filter circuits. The design of high-speed avalanche photodetectors with improved detection sensitivity is another exploration to lower the overall power consumption. Validated system performance improvements using avalanche photodetectors through experimental demonstrations with high-order modulation formats of both 4-level pulse amplitude modulation and coherent quadrature amplitude modulation prove the advancement in satisfying future interconnect demands.

Chapter 1 Introduction

1.1 Motivation

The global IP data traffic, largely driven by new wireless applications, cloud storage and computing, video streaming, virtual and augmented reality traffic, artificial intelligence (AI), and internet of things (IoT), increases with a 36 percent compound annual growth rate (CAGR) from 2005, which is expected to reach 396 exabytes per month by 2022, up from 122 exabytes per month in 2017 [1]. On the other hand, the world's data centers consumed 205 terawatt-hours of electricity in 2018, which is about 1% of all electricity consumed worldwide that year [2]. While the overall electricity efficiency is expected to improve, it is not enough to cope with $\approx$36% annual growth rate for global IP traffic. As a result, the global electricity demand of data centers would keep increasing and is shown in Figure 1.1 (b) from 2010 to 2030, where the overall electricity efficiency is expected to improve by 15% per year in the best scenario, by 10% in the expected and by 5% in the worst-case scenario [3]. Thus, the infrastructure for tomorrow's information and communication technology requires not only higher interconnect bandwidth but also more energy-efficient data communications to accommodate the increasing amount of data traffic.

Integrated photonics is the key technology to break the I/O interconnect bottleneck in both the bandwidth and energy consumption [4]. There are three key material platforms that are explored for monolithic integration, which are Indium phosphide (InP) [5], silicon nitride (SiN) [6], and silicon-on-insulator (SOI) [7]. The InP platform enables the integration of various passive and active photonic components. However, the lack of

compatibility with the complementary metal-oxide-semiconductor (CMOS) process made it lack the potential for low-cost and mass production. The SiN platform is hard to realize high-speed modulation, unless hybrid integration with other materials is employed. Overall, the SOI platform, with its CMOS fabrication compatibility and high-speed modulation and detection function availability, is the most promising for low-cost and high-density photonic integration as the waveguide size and bending radius are much smaller than those on the InP and SiN platforms.

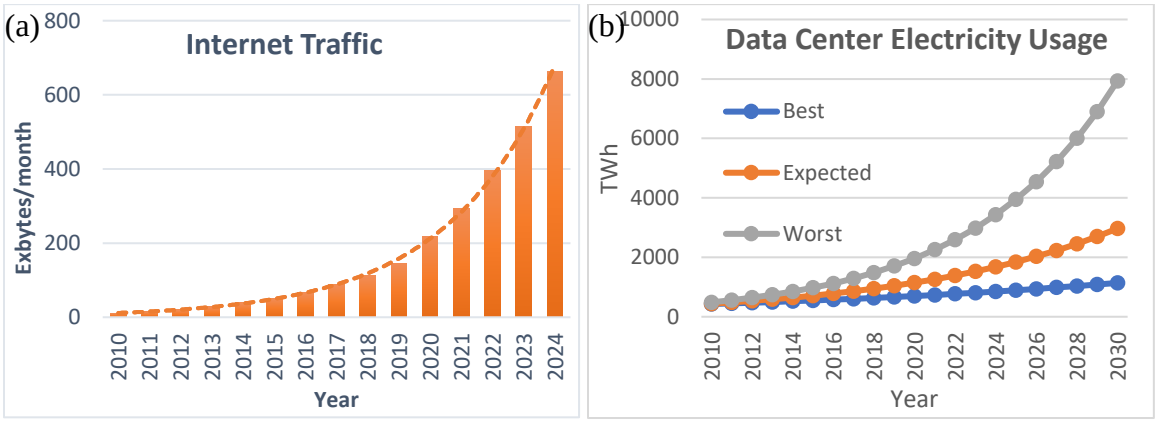

Figure 1.1 (a) Global internet traffic trend and prediction; (b) global electricity demand of data centers 2010–2030 [3] (annual electricity efficiency improvement: best (15%), expected (10%), and worst (5%)).

Over the last two decades, driven by its tremendous market potential, silicon photonics draws vast interest, both in academic and industry [8]. The share of SiP-based optical transceivers is projected to increase from 14% in 2018-2019 to 45% by 2025 [9]. Key components like high-speed modulators, photodetectors, and multiplexers/demultiplexers (MUX/DEMUX) have demonstrated tremendous performance improvements. Silicon photonics modulators based on plasma dispersion effect have demonstrated at data rate of > 100 Gb/s with both Mach-Zehnder (MZ) structure [10] and ring resonator structure [11]. Ge-on-Si PIN photodetectors have been

demonstrated with more than 40 GHz bandwidth [12], [13]. Broadband MUX/DEMUX for Wavelength Division Multiplexing (WDM) are demonstrated in designs using cascaded Mach-Zehnder interferometer (MZI) [14] and arrayed waveguide grating [15]. The indirect band structure of silicon poses challenges on the source and gain functionality directly in silicon, heterogeneous integration [16], [17] have been investigated to resolve the laser source bottleneck which enable complete functionality in silicon photonics platform. On-chip frequency comb generation is another technology enabling multiple coherent laser sources. Restricted by effects like two photon absorption (TPA) and free carrier absorption (FCA), most of the current demonstrations in SiP are in the mid-infrared range [18], [19]. Besides the work on improving individual device performances, techniques such as WDM and advanced modulation scheme (e.g., pulse amplitude modulation (PAM), quadrature amplitude modulation (QAM)) are utilized to increase the aggregated link data rates beyond the device bandwidth performances.

Generation of multiple optical carriers is a very important part of a WDM transmitter, in terms of both overall chip complexity and power consumption. An on-chip frequency comb is preferred over an integrated laser array as it is a more compact and scalable solution. It also offers a locked frequency spacing with mutual coherent lines that can be exploited for techniques like super-channel Nyquist-WDM to further increase the overall spectral efficiency (SE). Existed demonstrations of WDM comb source in Si mainly rely on modulation technique, either with a ring modulator [20] or a MZM [21]. On the other hand, silicon is a material with high nonlinear index. With proper dispersion profile engineering and nonlinear absorption effects mitigation, WDM comb source could be generated efficiently relying on the nonlinear effects of silicon waveguides.

The use of high-order modulation (HOM) formats poses more stringent challenge on the transmission distance in a power-limited system like datacom while maintaining low levels of power consumption and small package sizes [22]. As HOM increases transmission speed, it generally shortens the transmission distance due to the limitation of launch power in the transmitter. This issue can be resolved by using fiber amplifiers or semiconductor optical amplifiers (SOAs) to boost the power of optical signals. The drawback is that these amplifiers consume large amounts of power. Furthermore, integrating an SOA into an optical receiver will require a large area in optical transceivers, posing further challenges on small form factor integration that is already under stringent conditions. Thus, although the use of the optical amplifiers will extend the transmission distance, they cannot meet the requirements of low power consumption and small transceiver size in datacom systems. Avalanche photodiodes (APDs), with demonstrated high sensitivity attributed to their internal avalanche gain [23], [24], offers a more attractive alternative solution to effectively reduce the optical link power budget, simultaneously with small device size similar with a normal photodetector.

Inspired by all these opportunities and challenges, this dissertation explores the designs and experimental demonstrations of silicon photonic devices and techniques that enable high-bandwidth low-power-consumption next generation short-reach optical interconnects.

1.2 Dissertation Overview

This dissertation investigates the design of silicon photonic devices including arbitrary ratio multimode interference (ArMMI) couplers, Ge-on-Si APDs, and silicon waveguides for efficient nonlinear wavelength multicasting that enable high-speed low-

energy optical interconnect, in aspects from theoretical derivations, numerical model simulations, experimental characterizations to concluded discussions.

Chapter 2 serves as a review of the relevant background regarding the current silicon photonics foundry processes, including the software simulation techniques used for the device design and circuit modeling, which forms the foundation for all the presented designs in this dissertation.

Chapter 3 proposes a new design of broadband angled ArMMI couplers and experimentally demonstrates the improvement on fabrication deviation resilience. Following the presentation of the devices' physical working principles and design innovations, the performance of the proposed new design is firstly numerically modeled with finite difference time domain (FDTD) simulations to show its improvement on wavelength and fabrication insensitivity. The performance improvements are further validated by dedicated experimental multi-chip measurements of the fabricated devices, followed by further demonstrations on the application of the device to a cascaded Mach-Zehnder filter circuit.

In Chapter 4, the design, characterization, and system implementation of waveguide-integrated Ge-on-Si APDs are demonstrated. Followed by the physics of avalanche gain principles, the material impact ionization properties of Ge and Si are reviewed. Relying on foundry-provided fabrication services with zero modification, the design and numerical simulation of the APDs with a PIN structure are investigated. The fabricated APD devices are characterized with direct-current (DC) measurement to get the dark current, responsivity and gain, noise spectral density measurements to extract the excess noise factor, and small-signal measurements to inspect the electro-optical (EO)

bandwidth. Further large-signal detection experiment with high-order modulation formats including both PAM4 modulation and coherent detection (16QAM) are also demonstrated, showing sensitivity improvement with multiplication gain provided by the APDs.

Chapter 5 proposes and demonstrates a novel concept for scalable wavelength multicasting based on multi-stage, loss- and dispersion-managed silicon mixer waveguide. The waveguide design in consideration of nonlinearity and dispersion is introduced, followed by numerical calculations of the proposed multicast concept. Afterwards, experimental demonstrations of a dual-stage mixer using two pumps and a QAM-modulated signal are presented to validate the multicast signal quality. Further comparisons between the experimental results and the numerical simulations show high consistency.

Finally, Chapter 6 summarizes this dissertation and discusses the future work.

Chapter 2 Silicon Photonics Technology Overview

While the transmission of data using optical methods has been in place for many decades, the photonic integrated circuits (PIC), especially when based on silicon, is much younger — at most, 20 years old. Since then, silicon photonics has become one of the leading technological solutions for PIC designs. This chapter will cover the background for SOI-based silicon photonics and current fabrication services available at commercial foundries, which form the foundation for all the device designs in following chapters as they are all designed relying on fabrication technology offered by foundries. The two types of chip-fiber coupling methods are also briefly introduced as both of them are implemented in the following chapters. The software simulation solvers used for design and modeling are discussed as well.

2.1 Silicon-on-Insulator Platform Overview

It is at the end of the 1980s and in the early 1990s that SOI-based silicon photonics becomes one of the main types of material platforms for compact integrated optics. As is shown by the sketch of the basic SOI material platform in Figure 2.1, silicon with high refractive index (n = 3.47 at 1550 nm) is surrounded by low-index silicon dioxide (n = 1.445 at 1550 nm) to achieve optical mode confinement inside Si. This large index contrast enables optical mode confinement in waveguides formed with compact dimensions on the order of a few hundred nanometers.

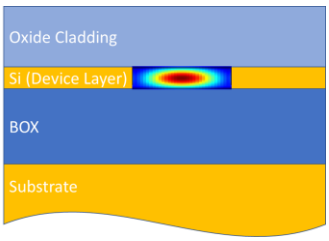

Figure 2.1 SOI material platform illustration.

Current SOI-based platforms that are most-commonly used for academia and industry are with a top Si device layer thickness of 220 nm and a buried oxide (BOX) thickness of 1 - 3 μm. The BOX thickness is defined for efficient optical mode confinement in the Si and the Si thickness is optimized for single-mode operation in telecommunications wavelengths. The 220 nm thickness has become a standard widely used in-particular by multi-project wafer (MPW) foundries and foundry service providers.

Silicon is, of course, not the only material system used for PICs and, in some cases, is not the best material system. Other systems, like SiGe, SiC, or InP, sometimes provide device performance advantages over silicon for specialized applications. However, the proliferation of silicon-based electronic ICs means that there is an unsurpassed infrastructure for silicon-based PICs to leverage the fabs, tooling, and supply chains already in place. This gives a significant advantage to silicon photonics in terms of commercialization, mass production, and integration with electronic components. Besides this, silicon photonics material platform offers other key advantages. Crystalline silicon is an exceptionally good optical material, with very low absorption at wavelengths longer than 1200 nm. Moreover, the refractive index contrast between silicon and its natural oxide silicon dioxide is high, enabling tight mode confinement and compact device feature size for large scale integration of photonic components on a chip.

2.2 Silicon Photonics Foundry Services

There are range of foundries offering silicon photonics MPW services from “passives only” to “full integration flows” using standardized platforms for concept validation and prototyping, such as Imec, IME, TowerJazz, AIMPhotonics, and so on. With the foundry lines to facilitate a fabless model, cost and accessibility for silicon photonics

research and development are drastically reduced by avoiding the associated expense in maintaining a silicon fabrication facility. Sharing of the costs for photomask and wafer processing through MPW shuttles further reduces the cost.

Photonic designers in the field of fabless silicon photonics work with a bottom-up approach for research and development, starting with the fabrication technology and materials offered by the specific foundry line and taking these as a starting point to develop integrated photonic devices, which offers a high degree of flexibility at the leading edge. Building a PIC on silicon photonics platform requires a number of basic components: passive devices to move light in, out, and around the chip (waveguides) and to split the light power (couplers); modulators to convert electrical signals to optical ones; detectors to convert optical signals to electrical ones; and a light source (which currently is often off-chip). Figure 2.2 shows a schematic cross section of a generic integrated technology platform consisting of both passives and active devices. The common offered function and fabrication capabilities include:

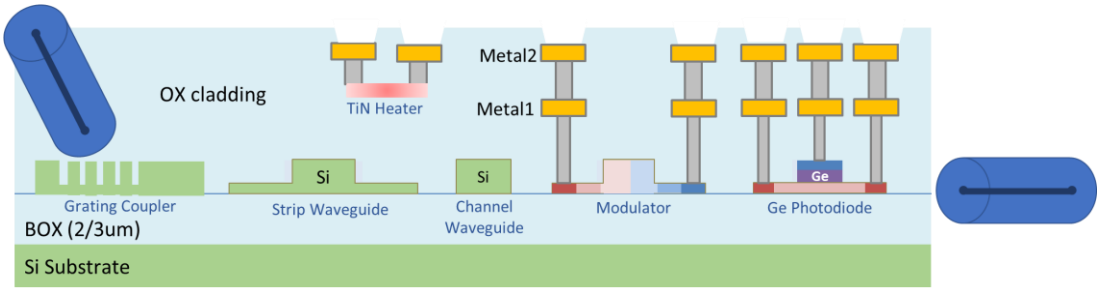

Figure 2.2 Cross section schematic of a SOI platform where key building blocks such as Si passives, Si modulator, Ge PD, thermal heater, and fiber coupling access are shown.

1) Partial and full Si etching steps to form passive devices such as strip waveguide, channel waveguide, grating couplers, edge couplers, etc. The patterning of the waveguiding layer (usually with photolithography and reactive-ion etching, RIE) needs to be optimized for pattern fidelity and sidewall roughness in order

for the passive devices to function as designed and to minimize loss through sidewall scattering.

2) Multiple ion implantations to achieve p / n doping with various dopant concentrations for constructing active devices such as phase shifters, modulators, photodetectors, switches, and filters.
3) Ge epitaxial growth step after the implants in silicon regions and an activation annealing step to develop Ge photodiodes and avalanche photodiodes.
4) Resistive heater using TiN film or implanted Si regions for thermal optical tuning.
5) Multiple metallization layers (2 - 3) to connect the doped Si/Ge/heater with the surface metal pads for electrical bias application and signal probing.

The optical light coupling from the fiber to the silicon photonics chip and vice versa can be accomplished via vertical coupling, edge coupling, or evanescent coupling (illustrated in Figure 2.3). As stated before, silicon waveguides are with dimensions of 500 nm × 220 nm, which is 2300 times smaller than standard single mode fiber with core diameter of 9 μm. The huge mode mismatch and effective index mismatch need to be mitigated with both silicon waveguide design and optical fiber engineering to enable low-loss fiber-chip coupling.

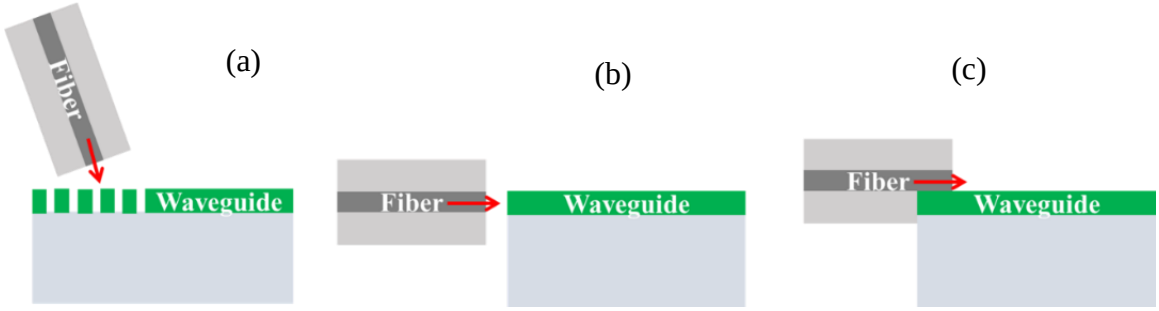

Figure 2.3 Illustrations of optical I/O coupling schemes: (a) vertical coupling, (b) edge coupling, and (c) evanescent coupling.

In vertical coupling, a passive photonic device called a grating coupler redirects light from a waveguide up to a fiber oriented normal (with a tilted angle to avoid back reflection) to the surface of the PIC. As grating coupling couples light in the vertical direction, it can be put anywhere on a chip, which provides flexibility in the design as well as enables wafer-scale automated testing. Moreover, the alignment tolerances between grating couplers and fiber arrays are much larger than edge couplers. The fabrication of grating couplers does not require post-processing, which reduces the fabrication complexity. Unlike the edge couplers, grating couplers could only operate at a specific operation wavelength range and polarization.

Alternatively, a fiber can be positioned parallel to the waveguide for light coupling. Edge coupling using invert tapers in silicon waveguides and lensed fibers is capable of delivering broadband high-efficiency coupling with an insertion loss below 0.7 dB, after careful alignment [25]. In addition, edge coupling is not polarization sensitive resulting in efficient coupling of both TE and TM polarizations. However, it can only be placed at the edge of the chips, and the implementation of such designs requires complicated fabrication processes and high-resolution optical alignment, which increase device processing and package cost.

Evanescent couplers serve as another coupling scheme in silicon photonics, where the fiber is brought very close to a waveguide through a deep trench so that the modes of the fiber and the waveguide overlap, allowing for efficient coupling [26]. An added advantage of the evanescent technique is the ability to form an optical connection at any point on the PIC surface, rather than at the PIC edge or facet, as with other fiber coupling. This design is at a relatively early stage of development.

2.3 Software tools for silicon photonics

PIC design and modeling can leverage the many decades of investment in electronic design automation (EDA) tools as many challenges of integrated photonics mirror those of integrated electronics. However, due to fundamental differences between photonics and electronics, there are other challenges that are specific to photonics and cannot be solved with existing tools and approaches.

One important difference is the size of devices compared to the wavelength. In most integrated optical applications, the free space wavelength is 1 - 2 μm (150 - 300 THz frequency), which is much smaller than the typical device feature sizes. In contrast, the free space wavelength in most electronic applications is typically larger than 3 cm (10 GHz frequency), which is much larger than modern electronic devices. This difference in scale compared to the wavelength poses different challenges for photonic designs. The operating principle behind many photonic devices (modulators, filters, etc.) is constructive and destructive interference, which requires precise phase control of the light traveling along the different waveguides. As a result, photonic devices are both large (compared to the wavelength) and yet extremely sensitive to nm scale errors in geometry, as well as environmental factors such as temperature. Another challenge posed by photonics is that shapes are nonrectilinear and follow non-Manhattan geometries. Waveguides that are 500 nm wide can cause unacceptably high reflections and loss if misconnected by only nanometers, which are challenging for existing EDA software both in terms of layout and design rule checks (DRC).

2.3.1 Physical simulation of components

Full 3D physical simulation is required for designing and optimizing individual photonic components. There are 3D physical simulation solvers ranging from electromagnetic, charge transport, to heat transport simulations. Moreover, the electromagnetic solvers consist of eigenmode solvers to solve waveguide modes, finite-difference time-domain (FDTD) and eigenmode expansion (EME) solvers for devices such as grating couplers and multimode interferometers (MMIs). Furthermore, it is required to apply multiple solvers for specific component designs; for instance, solving a photodiode requires an FDTD solver to calculate the optical absorption distribution as well as a charge transport solver to determine the carrier and current density as a function of bias voltage. Commercially available software like Lumerical offers a broad range of solver products (FDTD Solutions, MODE Solutions, DEVICE, and INTERCONNECT) that cover all physical simulation needs for integrated photonics, which is used for most of the components design in this dissertation.

2.3.2 S-parameter-based simulation of circuits

The 3D physical simulation allows for parameter extraction including electrical, optical, and thermal results, which are utilized to build compact models to realize rapid simulation of circuits and systems containing many components in the frequency and time domains. The extracted component performances in frequency domain is represented by S-parameters, which can be imported in circuit simulators like Lumerical INTERCONNECT for photonic circuits analysis. As an example, the S-parameter-based circuit simulation is applied in chapter 3 section 3.5 (Figure 3.21).

2.3.3 Transient simulation of circuits

Time domain simulation is used to capture the transient response of a circuit. In typical photonic circuits such as a datacom link, laser sources are either directly modulated or externally modulated with modulators, using electrical signals in frequencies of tens of GHz. The photonic transient simulation can be applied to calculate the eye diagram or constellation diagram for advanced modulation formats for data communications modeling, as shown in Chapter 4 section 4.4 (Figure 4.26). Further information such as bit error ratio (BER) estimates can then be obtained by using a Gaussian method to estimate the signal BER from the eye diagram.

2.4 Summary

In this chapter, the advancements of silicon photonics that enables large-scale low-cost PIC designs are briefly discussed. Moreover, the components of the PIC foundry industry ecosystem are described, with a specific discussion on the optical I/O coupling schemes between the silicon chip and optical fibers, which form the foundation for all the designs in the following chapters. The software simulation methods used for component and circuit designs in this dissertation are covered.

Chapter 3 Arbitrary Ratio Multimode Interference Couplers

3.1 Background

Wavelength-invariant optical coupler with arbitrary coupling ratio is one of the most fundamental elements in any PIC designs [27], especially in photonic circuits supporting data communication applications, such as wavelength multiplexing/demultiplexing [28], [29] and signal switching [30], [31]. Directional coupler classes can provide arbitrary coupling ratio [32] and have been widely implemented in various PIC designs. While its simplest form features low complexity design, this approach suffers from severe chromaticity and is highly sensitive to dimensional deviations inherent with imperfect lithography and etching during fabrication processes [33]. In contrast, multimode interference (MMI) couplers offer both wide, wavelength-insensitive bandwidth and considerably better tolerance to fabrication variations and errors. However, their main drawback is widely recognized: these devices allow for only five discrete coupling ratio choices [34]–[36].

Multiple approaches have been proposed and demonstrated to overcome this limitation, with varying success. One strategy relies on tuning the local index of the multimode waveguides. Widened- and narrowed-body MMIs with arbitrary ratios were first realized at a single wavelength in [37] and then broadband in [38]; tunable MMIs were demonstrated by applying thermal tuning in [39], [40]; multimode waveguide hologram with different etching depth to achieve index modulation was described in [41]. While arbitrary coupling ratios could be realized, these methods impose stringent requirements on fabrication accuracy and etching resolution. In an alternative approach, two MMIs were cascaded in a Mach–Zehnder interferometer (MZI)-like structure, without localized control

within multimode waveguides. Various implementations had been demonstrated, including using a cladding-filled gap in [42] in silica, adding two connecting waveguides with unequal width in [43] in InAlAs, and utilizing two waveguides with linearly tapered width in [44] in 4 μm thick SOI. All these designs require additional waveguide connections scaled at approximately 100 μm in length, resulting in larger device footprint. An alternative technique uses an angled connection and was first demonstrated in planar silica optics in [45] and later in GaAs–AlGaAs in [46], relying on a bent connection to impose a differential phase shift among the images without extending the length of the device. The same angled design scheme also relieves the requirements for tight width control of the phase shift waveguides as in MZI approach. However, only single wavelength results were reported [45], [46] with none in SOI, and no evaluation of the wideband performances and fabrication sensitivity were reported so far.

Consequently, the primary goal of this chapter is to study a newly proposed angled arbitrary ratio MMI coupler design based on 220 nm SOI platform with detailed numerical and experimental analysis on its wavelength independence and fabrication tolerance advancements.

3.2 Working Principles and Design Considerations

MMI couplers work on self-imaging principle, via which the input field profile is reproduced in single or multiple images at periodic intervals along the propagation direction of the multimode waveguide [35]. For a step-index multimode waveguide of width W_{MMI} (shown in Figure 3.1) which supports *m* lateral modes with mode numbers ν = 0, 1, ... (m - 1), the propagation constants β_υ of the supported modes show a nearly

quadratic dependence with the mode number ν. The beat length of the two lowest-order modes L_π is defined as: [35]

$$L_\pi = \frac{\pi}{\beta_0 - \beta_1} \simeq \frac{4 n_r W_e^2}{3\lambda_0} \tag{3-1}$$

where n_r is the ridge index of the multimode waveguide, W_e is the effective width which satisfies $W_e \simeq W_{MMI}$ for high index contrast waveguides as in SOI platform, and λ_0 is the center wavelength.

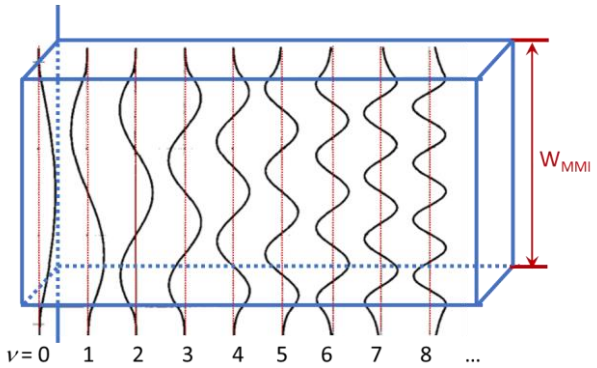

Figure 3.1 Multimode slab waveguide with width W_{MMI} and multiple supported lateral modes.

For devices working on general interference (GI) [35], at a propagation distance of L,

$$L = \frac{p}{N}(3L_\pi) \tag{3-2}$$

where $p \geq 0$ and $N \geq 1$ are integers with no common divisor, N images of the input field are formed inside the multimode waveguide. Here p indicates the imaging periodicity, with $p = 1$ corresponding to the shortest device in company with the lowest loss. Specially for $N = 2$, two images will be reproduced at a distance of $3/2\, L_\pi$.

Besides the general interference, MMI couplers can be realized in another fashion where only some of the guided modes in the multimode waveguide are excited by the input field(s). By launching an even-symmetric input field at $1/3\, W_e$ away from the multimode

waveguide edge, selective modes of every third (ν = 2, 5, 8, ...) would not be excited. In this way, paired interference (PI) is realized with the image reconstructing length only $1/3$ of the general interference case (Eq. 3-2), resulting in devices with smaller feature sizes that benefit for large scale integration [35].

Straight-line MMI couplers designed with either general interference or paired interference principles, however, cannot in general achieve any desired splitting ratio but just 5 discrete non-trivial values, namely 15/85, 28/72, 50/50, 72/28, and 85/15 [36].

One way to realize MMI couplers with arbitrary coupling ratios is to cascade two 3-dB MMI couplers with a phase shift section in between [47], as illustrated by the notional topology shown in Figure 3.2. By selecting an appropriate differential phase shift $\Delta\Phi_d$ between the two phase-shifter arms in accordance with Eq. 3-3, any desired coupling ratio can be attained and is related to $\Delta\Phi_d$ by cosine law as:

$$\eta = \frac{P_{cross}}{P_{cross} + P_{bar}} = \cos^2\left(\frac{\Delta\Phi_d}{2}\right) \qquad 3\text{-}3$$

Here the coupling ratio η is defined as the ratio of cross-port output power to the total output power $\eta = {P_{cross}}/{P_{cross} + P_{bar}}$. With $\Delta\Phi_d$ varying from 0 to π, a full coupling ratio range of 0% to 100% can be addressed in principle.

Figure 3.2 Simplified layout of arbitrary ratio MMI coupler.

Figure 3.3 illustrates the means for introducing the differential phase shift $\Delta\Phi_d$ in conventional angled MMI coupler design [45]: a miter joint is made at $3/2\ L_\pi$ away from the input. At this position, two self-images of the input field are formed, each sharing half

of the input power [35]. The self-images experience an optical length difference within the angled junction, and thus the differential phase shift is introduced. The self-imaging length L_π is defined as the beat length of the two lowest order modes as in Eq. 3-1.

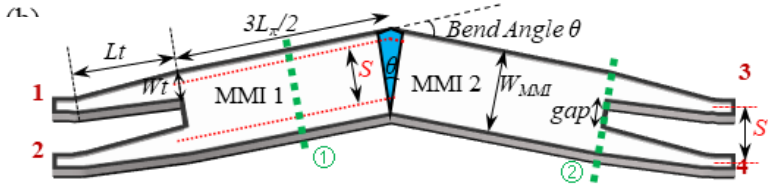

Figure 3.3 Schematic of the conventional angled MMI. *Lt*: access waveguide taper length; *Wt*: taper end width; W_{MMI}: multimode waveguide width; *S*: input/output waveguide separation.

The $\Delta\Phi_d$ added by the bend section can be estimated as:

$$\Delta\Phi_d \simeq \frac{2\pi n_{eff}}{\lambda} \cdot S \cdot 2\sin(\frac{\theta}{2}) \qquad 3\text{-}4$$

where S represents the center-to-center input(output)-waveguide separation, θ is the bend angle, and n_{eff} is the effective index of the reproduced input mode. From Eq. 3-3 and Eq. 3-4, it can be seen that any coupling ratio can be achieved with selection of the bend angle θ.

Besides unrestricted coupling ratio selectability, an ideal optical coupler must be able to maintain its coupling ratio across broad bandwidth, as ratio deviation across wavelength leads to loss / extinction ratio dispersion across the operating band of wideband devices such as wavelength filters and switches [14]. The imaging length L_π of MMI couplers, however, is inherently wavelength dependent as indicated by Eq. 3-1. While the impact of such wavelength dependency in a straight-line MMI is only seen over a bandwidth larger than 200 nm [19], the miter joint in an angled MMI coupler heightens the sensitivity of imaging-length shift in coupling ratio. As illustrated by the electric field distributions in Figure 3.4. To show this wavelength dependence effect, we simulate the

electric field evolution across the entire device with a bend angle corresponding to 180° differential phase shift $\Delta\Phi_d$ (i.e., 0% coupling ratio) using 3D-FDTD model. The electric field results are visualized in Figure 3.4 (a), while Figure 3.4 (c-e) plot the local field distributions in the connecting bend region at different wavelengths. As shown, the self-imaging location swings from beyond the joint at shorter wavelength (1500 nm) to before the joint at longer wavelength (1600 nm) than the designed operating wavelength (1550 nm). The shift in self-imaging location alters the amount of differential phase shift, thereby causing a deviation of coupling ratio. Worse, the focal point shift disrupts the output-side imaging process, which leads to increased excess loss.

Similarly, dimensional deviations of waveguide thickness (which change n_r in Eq. 3-1) and waveguide width W_{MMI} also impose shifts in imaging length, consequently leading to coupling ratio drift and excess loss increase in presence of fabrication error, implying that fabrication tolerability improvement is essential for the conventionally designed device.

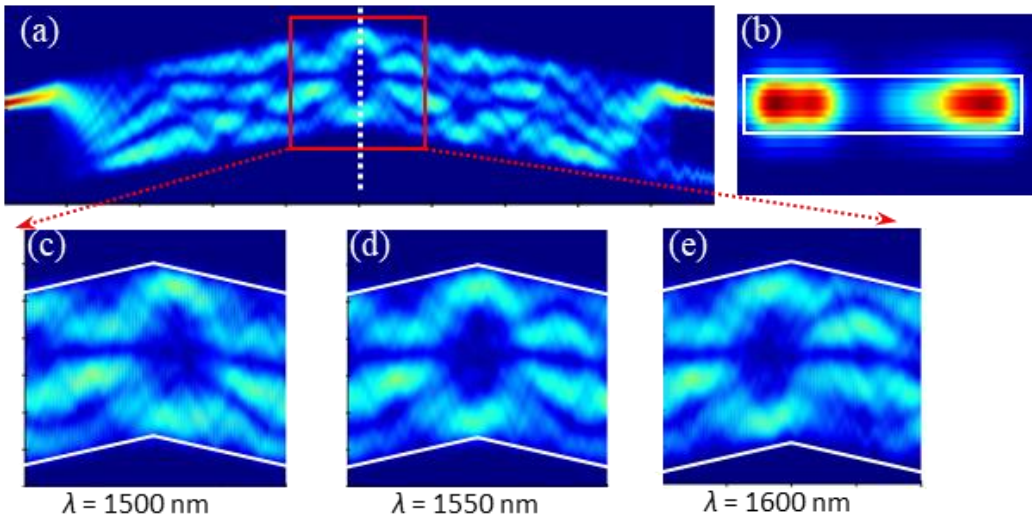

Figure 3.4 (a) Electric field distributions of the conventional angled MMI. (b) Reproduced mode profile at the middle of the device marked in white dotted line in (a). (c-e) Zoomed-in field distributions in the bend region at 1500 nm, 1550 nm, and 1600 nm, separately.

3.3 New Design Proposal, Simulation, and Tolerance Optimization

Realizing the chromaticity and fabrication deviation sensitivity issues of the conventional angled MMI couplers, a new design seeking to address both using optimized launch and angled junction design is proposed, as illustrated in Figure 3.5.

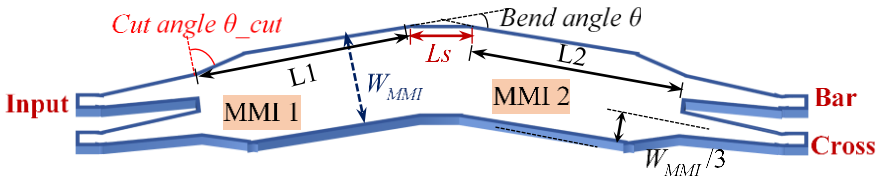

Figure 3.5 Schematic of the proposed new angled MMI design

The devices are designed on SOI platform with 220 nm Si layer thickness and 3 μm buried oxide thickness and are intended for TE0 mode operation. The devices are designed for 220 nm SOI platform with 3 μm buried oxide and are intended for TE_0 mode operation. The fully-etched multimode waveguide body within the coupler structure are 4.8-μm wide and support up to 15 TE modes, of which the first 12 modes (Figure 3.6) satisfy the quadratic index relationship required for high-quality self-image formation [35], a pre-requisite for low-loss MMI devices. The excitation of modes with even higher orders should be avoided in order to reconstruct the images and lower the loss.

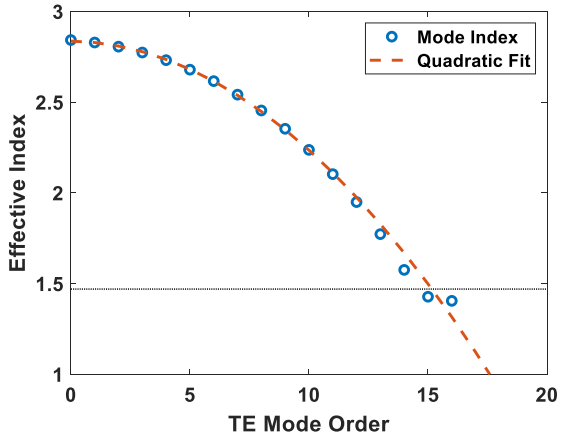

Figure 3.6 Mode indexes of the supported modes of multimode waveguides with 4.8 μm width; dashed line shows the 2nd-order polynomial fit.

Instead of general-interference (GI) designs used in [45] and [48], the new design employs paired-interference (PI) design [35], which offers distinct advantages. Firstly, by exciting only a subset of the supported modes (i.e., TE_m modes satisfying $m = 3n - 1$ are not excited, where n is any positive integer) [35], PI design reduces imaging length by a factor of 3 when compared to GI designs of the same multi-mode body width, thus reducing overall footprint and allowing for large scale, dense integration. Secondly, the centrally-located PI ports (centered at $W_{MMI}/3$ and $2W_{MMI}/3$) dictate that the image reproduction occurs in closer proximity to the centerline of the multimode body [35] than the self-images in the equivalent GI design, as shown in Figure 3.4. The reduction of side-wall guiding effect on the self-images eliminates the needs for miter joint to maintain self-image quality as in GI designs, therefore creating new possibility for bend junction optimization to mitigate wavelength and geometry sensitivities inherent to the highly-localized nature of a miter joint.

Figure 3.7 demonstrates the electric field distribution of the new design with beveled bend that leverages the advantage of PI design to reduce the sensitivity of coupling ratio to self-imaging length deviation. As seen in Figure 3.7, the beveled bend design maintains the self-image quality of a PI MMI coupler, as the image field has largely decayed at the waveguide edges (Figure 3.7 (b)). This represents a stark contrast to GI MMI design where the image field is intense at the edges (Figure 3.4 (b)) and thus, the beveled corner would have significantly disrupted the subsequent output-side image formation due to mode mismatch. The benefits of the beveled joint are well explained by Figure 3.7 (c – e): despite the lateral drift in self-imaging length due to wavelength (or geometry) shifts, the images remain confined inside the flat multimode body in which the

optical length are identical for both images, thereby decoupling the differential phase shift from self-imaging length drift. The constant guiding conditions in the flat body further reduce output-side image distortion due to self-imaging length drift, as suggested by the stable field pattern beyond the self-images when the input wavelength is varied.

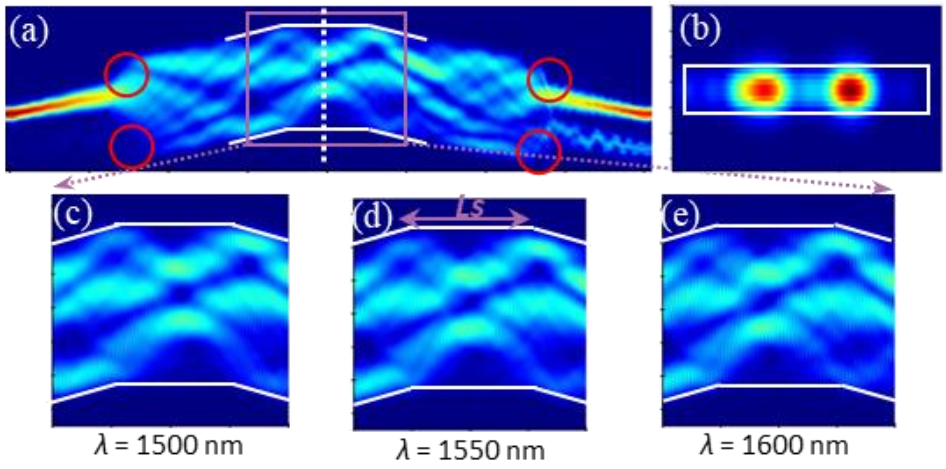

Figure 3.7 (a) Electric field distributions of the new angled MMI. (b) Cross-section mode profile at the middle of the device marked in white dotted line in (a). (c-e) Zoomed in field distributions in the bend region at 1500 nm, 1550 nm, and 1600 nm, separately.

Although subject to wavelength dependency imposed by Eq. 3-1, the new design still offers wider-band phase matching to allow for more achromatic and fabrication-tolerant devices. As a result, the coupler with beveled bend demonstrates three-times lower coupling ratio drift than the equivalent design with miter bend across the extended C-band. The coupling ratio spectral responses of the new design with beveled bend and the conventional design with miter bend are shown in Figure 3.8 for reference.

The new design further aims to suppress spurious reflections, as excess reflections degrade signal quality by generating in-band crosstalk and may cause oscillation in on-chip / off-chip gain blocks. Since the field intensity at the corners adjacent to the input and output ports of PI MMI is weak (marked by red circles in Figure 3.7 (a)), these corners of

the multimode body are trimmed to a specific angle (θ_cut in Figure 3.5) in order to suppress stray light reflection [49].

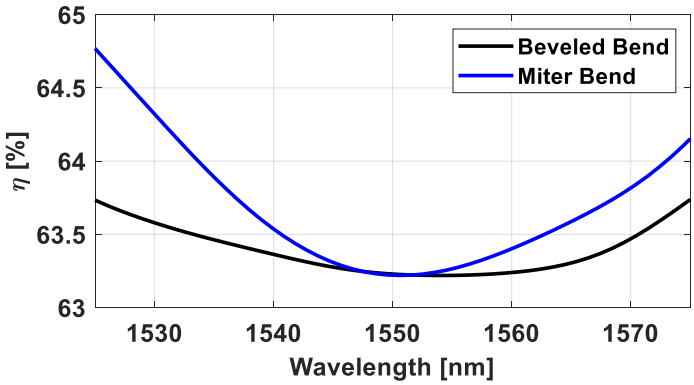

Figure 3.8 Comparison of coupling ratio spectral responses with beveled and miter connections.

To further illustrate the reduction in loss and reflection, the field evolutions without and with the cut edge θ_cut are plotted in Figure 3.9 on the left and right sides respectively, clearly showing that the reflection for designs with the θ_cut is decreased.

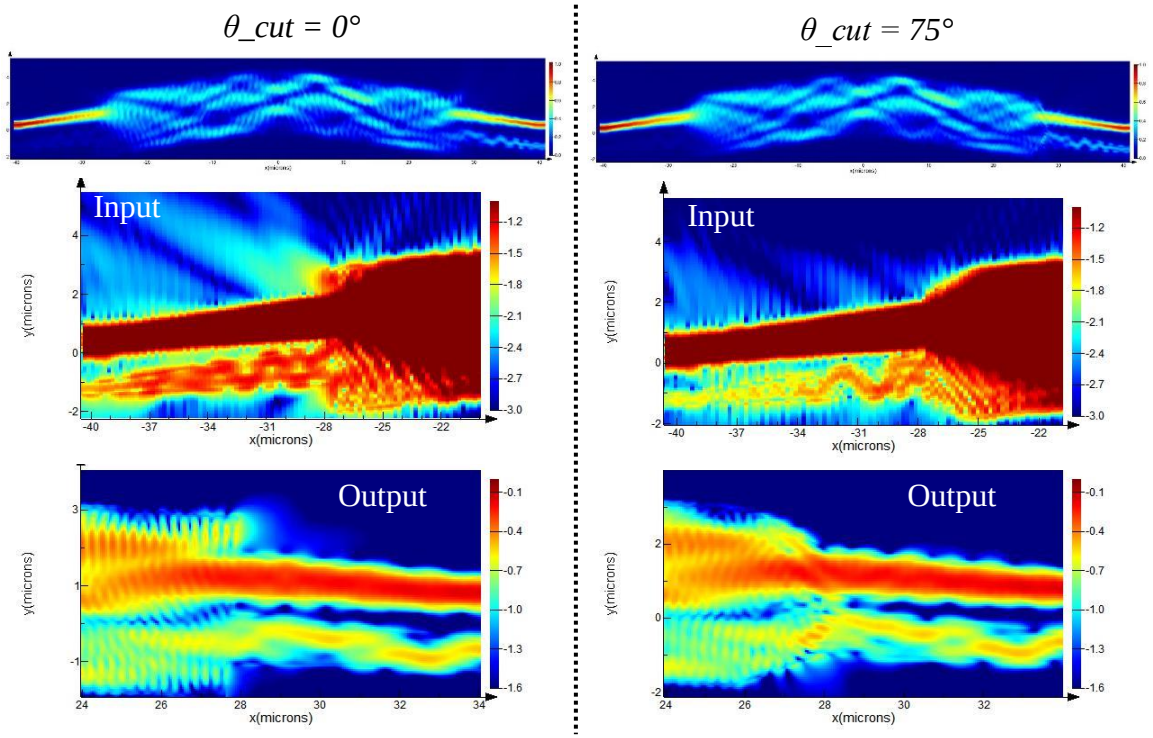

Figure 3.9 Comparison of field evolution with and without the edge cut angle (left: without θ_cut; right: with θ_cut).

The field scattering loss at the input/output edge facets are also reduced. The extracted values from FDTD simulations indicate a loss reduction of 0.2 dB (Figure 3.10 (a)) and a decreased reflection to less than 0.03% (Figure 3.10 (b)) across the extended C band with the corner cut.

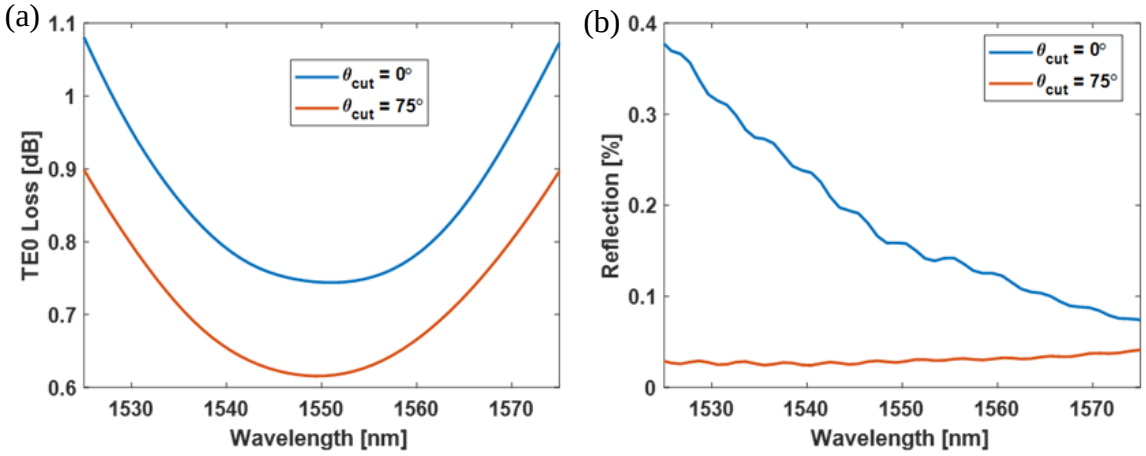

Figure 3.10 (a) Loss and (b) reflection values for designs with and without *θ_cut*.

As demonstrated above, the sensitivities of coupling ratio and excess loss of angled MMI couplers are jointly defined by the multi-mode waveguide body, and input / output mode-matching tapers. This section describes the optimization process for input / output tapers, with focus on the impact and mitigation of fabrication errors.

In presence of geometry deviation, the self-imaging process of the MMI coupler is distorted due to the departure from the ideal quadratic index relationship among the excited modes [34]. To evaluate the impact of fabrication error in various input / output launch designs, the image (total) phase error is modeled from modal phase error [50], [51]. Equation (3-1) shows that deviations of the MMI width δW and the ridge index δn_r (caused by device thickness deviations δt) lead to imaging length deviation δL from the designed length L, as:

$$\delta L/L = 2\,\delta W/W + \delta n_r/n_r \tag{3-5}$$

Assuming the input tapers excite modes that follow the quadratic index relationship in the multi-mode waveguide, the imaging length shift δL is equivalent to introduction of phase errors $\delta\Phi_m$ among the excited m^{th}-order guided modes [51]:

$$\delta\phi_m = \frac{m(m+2)\pi}{3}\frac{\delta L}{L_\pi} \tag{3-6}$$

The modal phase error $\delta\Phi_m$ contributes to imaging errors at the output. Therefore, the following total phase error $\delta\Phi$ is chosen as the criterion for performance robustness analysis, which is calculated as

$$\delta\Phi = \arg\left[\sum_m c_m \exp(j\cdot\delta\phi_m)\right] \tag{3-7}$$

where c_m is the field excitation coefficient of the m^{th}-order mode [35].

Following practical fabrication margins expected in commercial foundries, ±10 nm deviations in both Si layer thickness and waveguide width are chosen as the fabrication process corners for the following robustness analysis. Note that while ±10 nm width deviations introduce a variation of $|2\delta W/W| = 0.00416$, larger variation of $|\delta n_r/n_r| = 0.0074$ is introduced with ±10 nm thickness deviations via direct mode calculation. Therefore, with the aforementioned process corner articulation, Si layer thickness variation is recognized as the dominant limitation. We also note that while the use of rib multimode waveguide body may improve self-imaging quality by reducing the modal phase deviations from the ideal quadratic conditions [52], variations in the partial etch depth would introduce significant variations to imaging length *L*: a 10-nm shift in partial etch depth from the target (80 nm) value results in 1.17% change in *L*. Consequently, partial etch is not used in the proposed design.

Next, we analyze the total phase error for designs possessing various taper width values. The minimum taper width is chosen to prevent excitation of non-quadratic phase modes (i.e., modes of order > 11 in Figure 3.6 (b)) in order to minimize mismatch loss due to imaging error [51], whereas the maximum taper width is selected to minimize unwanted coupling of fundamental modes in adjacent tapers. The taper length (10 μm) is chosen to guarantee adiabatic transfer of power from single-mode access waveguides to the fundamental mode at taper output. The mode excitation coefficients c_m are derived from overlap integrals between the cross-sectional fields obtained from 3D-FDTD simulations and the supported modes at the locations ① and ② as labeled in green in Figure 3.3, which respectively yield the excitation coefficients for only the input-side MMI (MMI1) and the entire multimode body. The total phase error $\delta\Phi$ due to the stated fabrication error is subsequently calculated for each taper design at locations ① and ②, corresponding to the phase error accrued in a single MMI segment and two MMI segments plus the bend structures. The phase errors $\delta\Phi_m$ were calculated by substituting Eq. 3-5 into Eq. 3-6.

The calculated total phase error $\delta\Phi$ at the center wavelength of 1550 nm for the conventional (CON) and the new (NEW) designs with different taper widths are plotted in Figure 3.11 (a). The bend angles in both designs correspond to the maximum angle θ_{max} required to provide full (0 – 100 %) coupling ratio coverage. Note that θ_{max} is invariant to taper width in PI designs as the port-to-port (and consequently image-to-image) separation S is fixed at $W_{MMI}/3$, whereas in the conventional GI-based designs, the port-to-port separation S, and therefore θ_{max}, change with taper width. The plots in Figure 3.11 (a) clearly depict two general trends: First, the total phase error decreases with increasing taper width, as a result of fewer modes being excited in the MMI region [35]. Second, the new

designs reduce the phase error by at least a factor of two compared to conventional designs of the same taper width. While GI MMI accepts wider taper width and thus can regain part of the total phase error margin, the PI-based new design is able to maintain its lead over the entire taper width range.

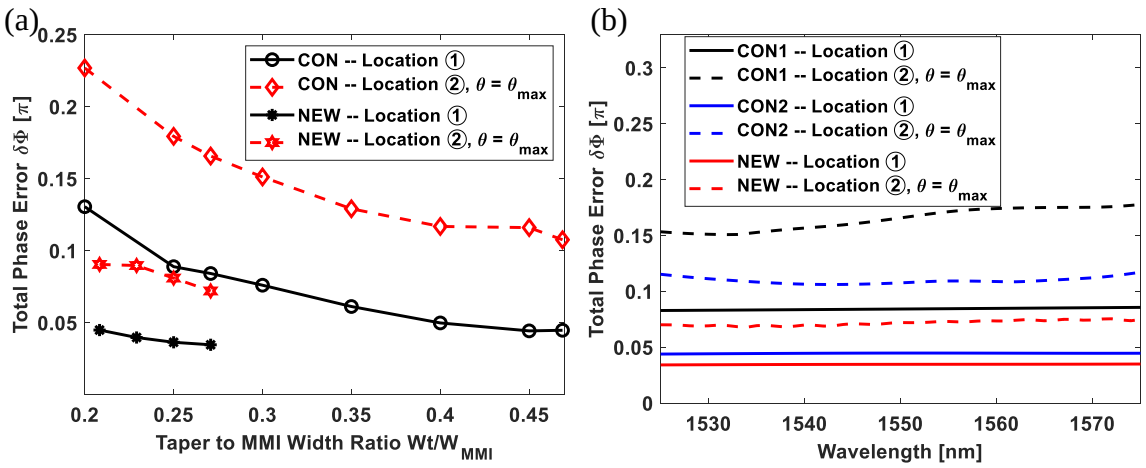

Figure 3.11 (a) Calculated phase error $\delta\Phi$ at 1550 nm as a function of taper to MMI width ratio, the results after MMI 1 are plotted in black and after MMI 2 are plotted in red. (b) Spectral dependence of phase error for selected designs as marked in (a).

A similar performance lead was observed in the wavelength domain, as depicted in Figure 3.11 (b) where the total phase errors of the optimal new design (i.e., that with the widest taper width, labelled as NEW), as well as an equivalent conventional design with the same taper width (CON1) and an optimal conventional design (CON2) corresponding to the minimum phase error of the conventional design, are plotted against operating wavelength. The new design not only provided a lower phase error at nominal (1550 nm) wavelength, but also a lower wavelength dependence over extended C-band. The results are plotted in Figure 3.11 (b), clearly showing that not only does the new paired design have the least phase error, but also show the least wavelength dependence.

Besides phase error analyses, comparisons of the coupling ratio spectral responses when subject to fabrication deviations for the three designs are also modeled. Devices with

a coupling ratio of 63% are shown in Figure 3.12 as an example, with solid lines corresponding to the target performance, dashed and dash-dotted lines corresponding to responses when subject to -10 nm and +10 nm thickness and width deviations. It is apparent from these comparisons that the new design possesses both improved spectral flatness and enhanced fabrication tolerance.

Besides phase error analyses, the new design is further compared against the selected conventional designs (CON1, CON2) in terms of coupling ratio variations due to fabrication deviations and wavelength shift. Devices with 63% coupling ratio are shown in Figure 3.12 as an example, with solid lines corresponding to the target performance, dashed and dash-dotted lines showing responses when subject to -10 nm and +10 nm thickness and width deviations. As shown in Figure 3.12, the new design exhibits 3.3× less variations across process corners and wavelengths, when compared to the optimal conventional design. It is apparent from these comparisons that the new design possesses both improved spectral flatness and enhanced fabrication tolerance.

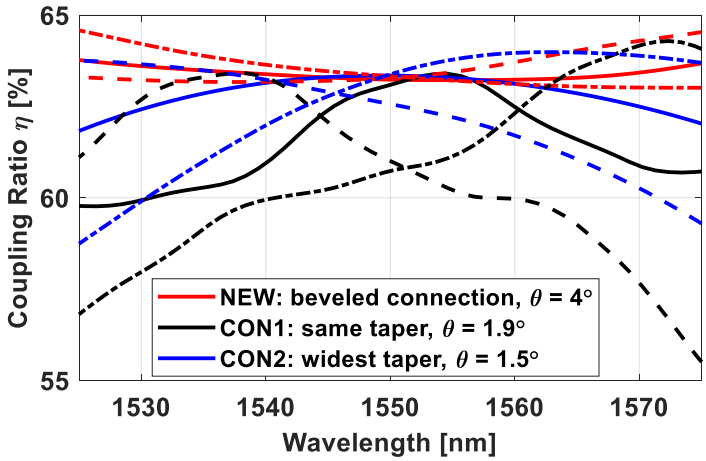

Figure 3.12 Comparison between the spectral responses of the three design cases when subject to dimensional deviations. (Solid: as designed; dashed: -10 nm thickness and width deviations; dash-dotted: +10 nm thickness and width deviations)

The final design parameters of the new design are listed in Table 3.1 All structures are based on fully etched channel waveguides to simplify fabrication and eliminate uncertainties caused by etch depth deviations. Single mode waveguides with 450 nm width are tapered to 1.3 μm width using 10 μm long linear taper and then connected to the input-side MMI (MMI 1). MMI 1 is jointed with the output-side MMI (MMI 2) via a beveled bend with a 5 μm long straight segment, and subsequently coupled to output single-mode access waveguides through linear tapers. Selected designs with various bend angles θ are integrated with vertical grating couplers (GCs) in a test chip layout for fabrication.

Table 3.1 Final ArMMI device design parameters

Parameters	Design Values
W_{MMI}	4.8 μm
L1/L2	24.3 – 24.5 μm
Ls	5 μm
θ_cut	75°
θ	0 - 9°
Wt	1.3 μm

3.4 Device Characterization and Analysis

The proposed devices were fabricated on SOI wafers with 220-nm-thick device silicon layer and 3 μm buried oxide layer using a commercial 180 nm foundry process. Newly designed devices were fabricated using commercial 180 nm foundry process. Figure 3.13 show the microscope images of the of a test set comprising four devices-under-test (DUT), each connected to four GCs for insertion loss and coupling ratio measurements. Two sets of back-to-back connected grating couplers are positioned on both the left and the right sides of the angled MMIs for GC-to-fiber coupling loss extraction, as well as for

guiding fiber array alignment, as marked in Figure 3.13 (a) with red rectangles. By simultaneously monitoring the coupling loss and optimizing the coupling efficiency of the two directly connected GCs, it is possible to minimize the fiber array alignment uncertainty and support more accurate device characterization results.

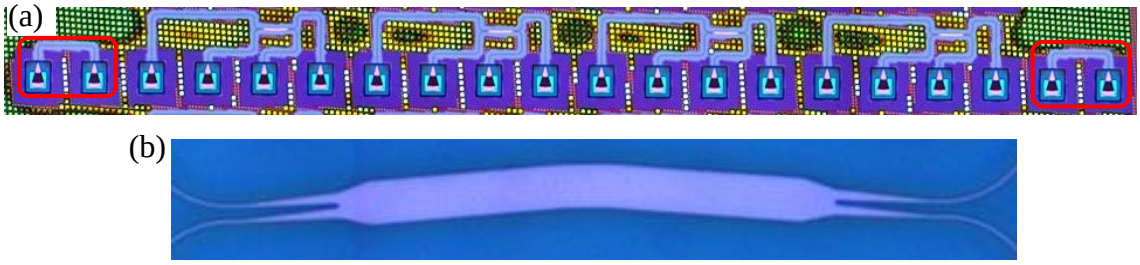

Figure 3.13 Microscope images of the fabricated devices: (a) layout for coupling; (b) device with 9° bend angle.

Fabricated devices were characterized experimentally measuring the port-to-port transmission using a broadband amplified spontaneous emission (ASE) source in C-band. The coupling ratio was calculated by dividing the output power from the cross port by the total output power, as defined in Section 3.2. The insertion loss was calculated using the difference between the input power and the total output power: $IL = -10\,log(\frac{P_{cross}+P_{bar}}{P_{in}})$.

Five tiles distributed across a test wafer were measured. Each tile carried 12 DUT designed with different θ values. The coupling ratio results at 1550 nm were extracted and plotted as a function of bend angle θ in Figure 3.14 (a) (red). Full coupling ratio range were attained within 9° bend angle. Measured coupling ratio averages (red) and standard deviations (green bars) suggest that the numerical model accurately predicted the coupling ratio *ab initio*, and the uniformity across wafer was remarkable. The excellent agreement between model versus hardware data demonstrated by the new coupler represents a major advantage over commonly-used directional couplers, in which the coupling lengths are

significantly influenced by process (e.g. etch bias and sidewall profile angle) and therefore, extraction of such must rely hardware measurements from stable, frozen processes.

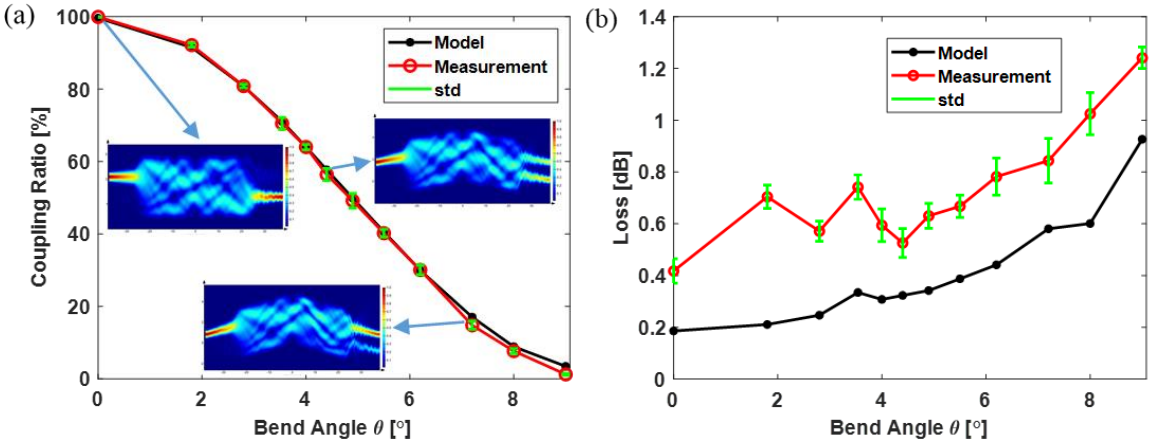

Figure 3.14 Simulation and experiment results of (a) coupling ratio and (b) insertion loss at 1550 nm with different angle θ. Insets in (a) are field profiles for selected θ values

Measured and modeled loss data at 1550 nm were plotted in Figure 3.14 (b), with green bars showing the standard deviations. The GC-to-fiber coupling loss had been deembedded in the reported data. The measured loss exhibited good agreement with the simulation results across the entire coupling ratio range, with discrepancy of less than 0.4 dB. The loss deviation from model was attributed to a drift of mean silicon thickness post-fabrication, and in part to fiber-to-chip coupling loss variations. However, we note that the measured insertion loss across all the devices remained below 1.2 dB. Compared with the straight-line MMI coupler with 0° bend, the device with a 9° bend showed 0.8 dB more loss.

The measured wavelength dependence of the new angled MMI couplers (θ = 0°, 1.8°, 2.8°, 3.54°, 4.4°, 4.9°, 5.5°, 6.2°, 7.2°, 8°, 9°) in terms of coupling ratios and loss were plotted in Figure 3.15 (a) and (b) respectively.

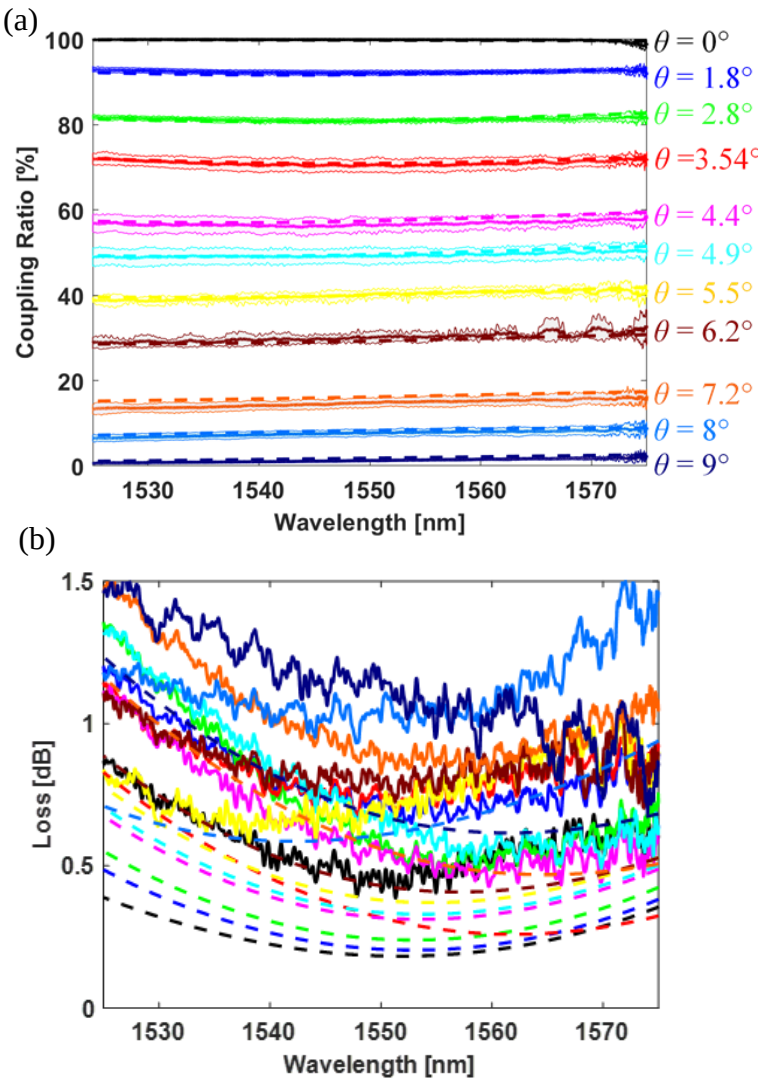

Figure 3.15 Measured wavelength dependence of (a) coupling ratio and (b) insertion loss for deferent θ (solid lines: experiment; dashed lines: simulation; patch plots show standard deviation of measurements).

The experimental results of coupling ratio are plotted in Figure 3.15 in solid lines with patch plots showing their standard deviations, while the simulation results are plotted in dashed lines with the same color. Similar to the single-wavelength plots in Figure 3.14, the measured coupling ratios and loss across wavelength matched that of the modeled results, once again verifying the proposed devices' insensitivity towards process bias. The worst-case loss was 1.5 dB over the extended C band.

The wavelength sensitivity of the designed couplers is further quantified using the coupling ratio deviation $\Delta\eta$, defined as the range of coupling ratios across wavelength and all devices with the same bend angle:

$$\Delta\eta = \left|\eta(\lambda_1) - \eta(\lambda_2)\right|_{\max} \qquad 3\text{-}8$$

where λ_1, λ_2 are wavelengths in 1525 nm and 1575 nm range. The calculated $\Delta\eta$ results are plotted in Figure 3.16 (a) as a function of nominal coupling ratios at 1550 nm, showing less than 2.3% maximum coupling ratio spectral variations for all devices and wavelengths. This should be compared with directional couplers fabricated on similar substrate, which typically exhibits ratio deviations in excess of 20% [53]. The ±1 dB bandwidth, as defined in [54], is much wider than the extended C band and could not be accessed experimentally. In fact, using the method outlined in [54], the calculated spectral variation for the device with coupling ratio of 50% and bend angle of 4.9° is only 0.1 dB in the extended C band. FDTD simulation results shown in Figure 3.16 (b) indicate the ±1 dB bandwidth wider than 250 nm.

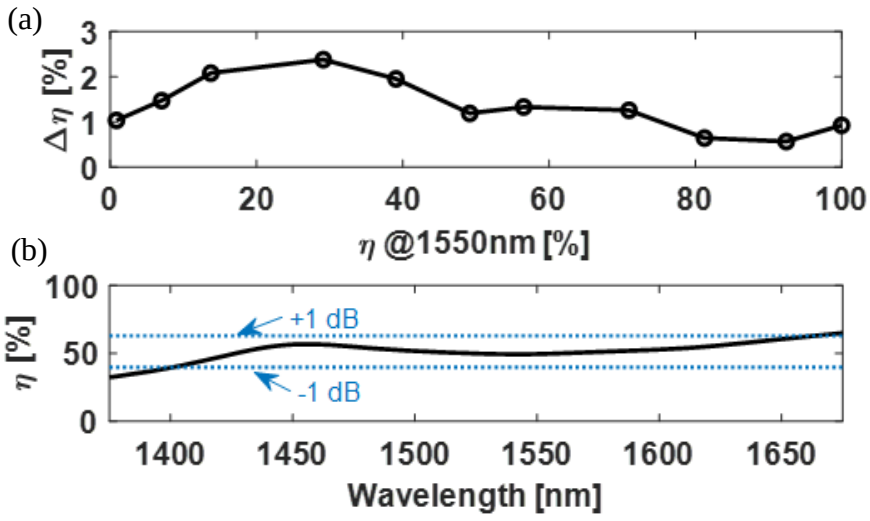

Figure 3.16 (a) Measured maximum coupling ratio variations in 1525 nm - 1575 nm band. (b) Simulated coupling ratio spectral response of 50% design.

Measured wideband loss also shows consistency with simulation, as demonstrated in Figure 3.15 (b): measurement results are plotted in solid lines while the simulation results are in dashed lines. All devices experience loss lower than 1.5 dB over the extended C band.

With experimental measurement results validating the accuracy of the model, we further extend the analysis of performance robustness against fabrication errors for the new coupler design. As stated earlier, ±10 nm deviation was used for both Si thickness and device width to characterize the fabrication process corners. The coupling ratio and loss variations caused by fabrication deviations are then calculated to quantify the performance robustness and are defined as:

$$\delta\eta(\lambda) = \eta_{dev}(\lambda) - \eta(\lambda) \tag{3-9}$$

$$\delta IL(\lambda) = IL_{dev}(\lambda) - IL(\lambda) \tag{3-10}$$

where $\eta(\lambda)$ and $IL(\lambda)$ represent the coupling ratio and loss for the target design, while $\eta_{dev}(\lambda)$ and $IL_{dev}(\lambda)$ are coupling ratio and loss for the designs exposed to fabrication deviations.

For the device with coupling ratio of 50% and bend angle of 4.9°, calculated $\delta\eta(\lambda)$ and $\delta IL(\lambda)$ at center wavelength are plotted in Figure 3.17 (a) and (b) separately. The design showed less than 1.3% (0.1 dB) coupling ratio variation and 0.3 dB loss variation across all possible fabrication deviations within the defined process corners. Figure 3.17 (a) also indicates that while the maximum $\delta\eta(\lambda)$ introduced by width deviations is 0.58%, a maximum $\delta\eta(\lambda)$ of 0.99% is introduced with thickness variations, which agrees well with the previous analysis.

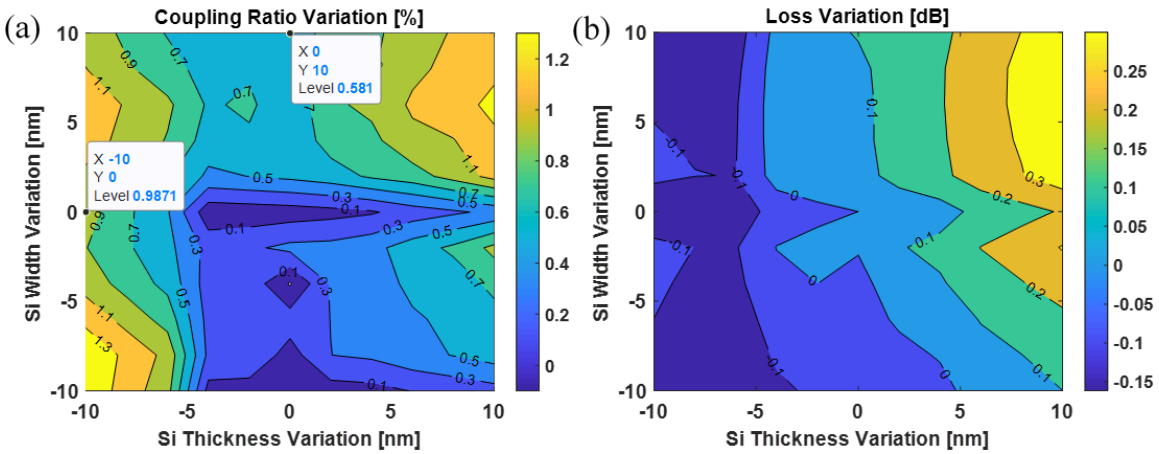

Figure 3.17 (a) Coupling ratio and (b) insertion loss variations at 1550 nm wavelength for 50% coupling design (bend angle θ = 4.4°) under ±10 nm Si thickness and width variations.

The wideband coupling ratio variations of devices when subject to dimensional deviations in designs with different bend angles are shown in Figure 3.18. The solid lines correspond to devices meeting the target design, dashed lines and dash-dotted lines indicate devices with -10 nm and +10 nm thickness and width deviations that represent two extreme values for the process corner definition. While relatively increased deviations are observed with wavelengths further away from the center wavelength (1550 nm), the overall coupling ratio variations remain small across the extended C band and fabrication process corners. As an example, the maximum $\delta\eta(\lambda)$ across the extended C band for the devices with 50% coupling ratio is 2.1% (0.17 dB) for -10 nm thickness and width deviations; the same design when subject to 10 nm thickness and width deviation shows maximum $\delta\eta(\lambda)$ of 1.4% (0.11 dB). Standard 220 nm SOI wafer rarely experiences thickness deviations as large as ±10 nm as defined here; in [53] thickness variations of ±2 nm were measured across a 300 mm wafer. Thus, practical coupling ratio deviations are expected to be even smaller than those shown in Figure 3.18.

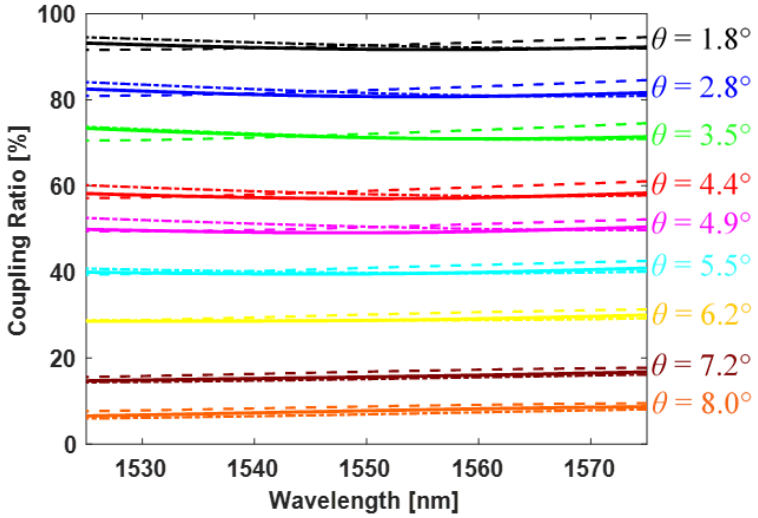

Figure 3.18 Coupling ratio spectral responses under the worst variation conditions: solid: as designed; dashed: -10 nm thickness and width variation; dash-dotted: +10 nm thickness and width variation.

3.5 Device Application for Cascaded MZI Filter Design

The proposed and demonstrated new design of broadband fabrication-insensitive arbitrary ratio MMI couplers are ready to be implemented in various PIC designs. This section demonstrates one potential application: cascaded Mach-Zehnder wavelength filters for WDM (de-)multiplexing [14].

The 2-channel wavelength splitting filter is designed with two delay stages [14]. The waveguide layout and transmission spectra of the wavelength splitter are shown in Figure 3.19 (a, b) and (c) separately. The coupling ratio (CR) requirements for the three connecting optical couplers are marked in Figure 3.19 (a) and (b) for two types of design configurations. As the basic MMI couplers cannot achieve coupling ratio values of 8%, 29%, 71%, and 92%, directional couplers are the coupler of choice for all the demonstrated results of cascaded Mach-Zehnder wavelength filters [14]. The coupling ratio wavelength sensitivity problems of directional couplers limit the broadband extinction ratio (ER) of the

designed wavelength filter, which can be relieved via designing with the new proposed broadband ArMMI couplers.

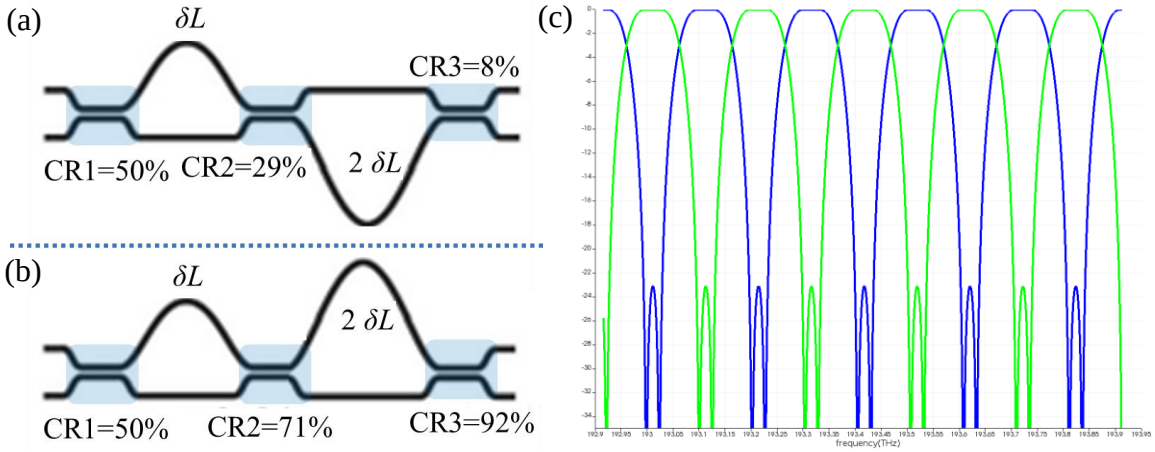

Figure 3.19 The waveguide layout (a, b) and transmission spectra (c) of the 2-channel wavelength splitter.

The coupling ratio and loss performances of the required optical couplers for the wavelength filter design with designs both in directional coupler scheme and ArMMI scheme are first modeled and calculated in 3D-FDTD simulations. The resulting coupling ratio performances in the extended C band are shown in Figure 3.20 (a), clearly indicating the spectral flatness and wavelength insensitivity of the new ArMMI designs. In terms of loss results (Figure 3.20 (b)), while the ArMMI couplers show 0.2 - 0.8 dB more loss than directional couplers, the loss are bound within 0.9 dB for all devices in the extended C band, which suffice most of the application requirements. For special design scenarios where loss matters more than spectral flatness, directional couplers may be chosen over ArMMI couplers.

The numerical modeling of the 2-chanel wavelength filter is implemented in Lumerical INTERCONNECT, with the schematic connection illustrated in Figure 3.21. The coupling ratio and loss results of the couplers are loaded to the circuit model via three

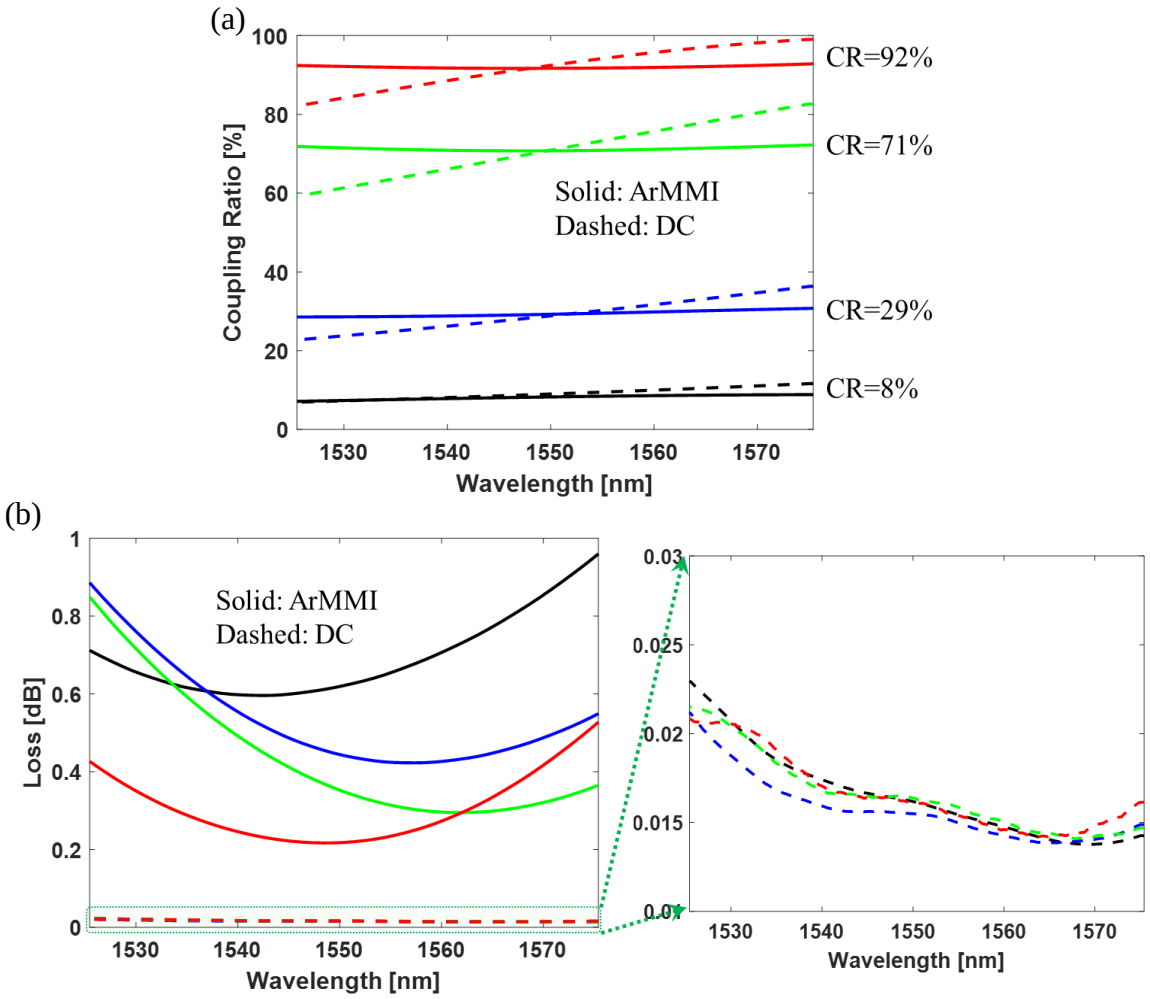

Figure 3.20 The calculated coupling ratio (a) and loss (b) spectral results for ArMMI coupler (solid) and directional coupler (dashed) designs.

S-parameter elements (SPAR_1, SPAR_2, SPAR_3), which are generated from the former FDTD calculations. The waveguide elements import the frequency-dependent properties (such as the effective index, loss, group index, dispersion, etc.) of the connecting waveguide directly from MODE simulations to characterize the silicon waveguide, leading to more accurate simulation results. We design the wavelength filter with a channel spacing of 100 GHz, which corresponds to a length difference of 340 μm between the long and the short waveguide arms (δL in Figure 3.19 (a) and (b)).

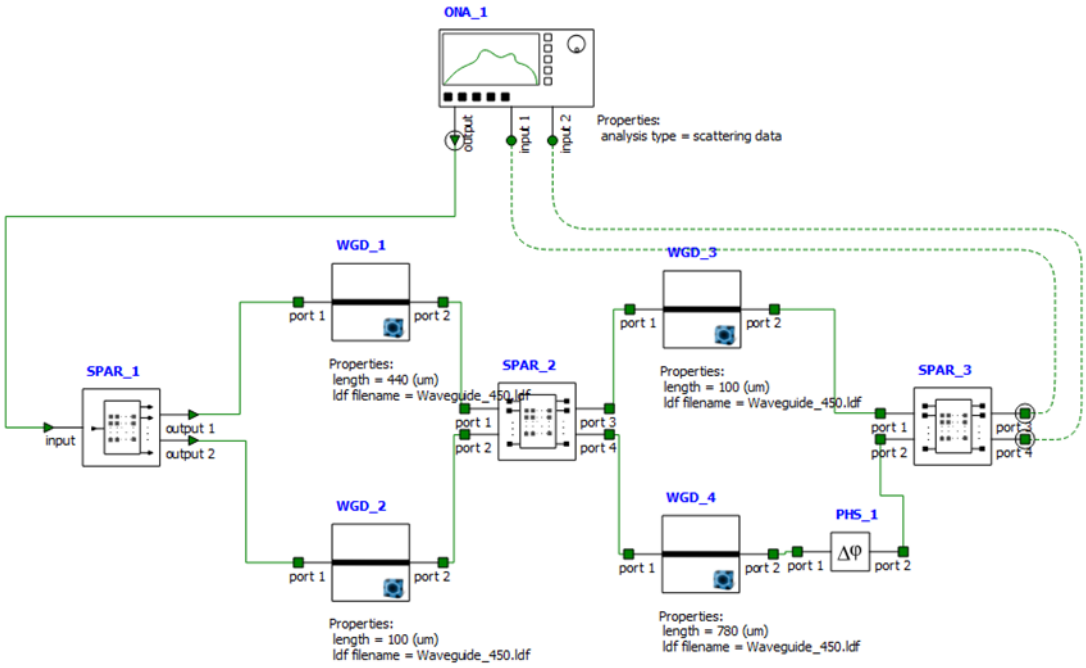

Figure 3.21 The schematic connection of the 2-channel wavelength filter design in Lumerical INTERCONNECT.

The numerically modeled output spectra of the 2-channel wavelength filter designed with both directional couplers and ArMMI couplers are plotted in Figure 3.22 (a, b) and (c, d) separately, with markers representing the extinction ratio (cross talk) levels. Due to the coupling ratio wavelength sensitivity problems of directional couplers, designs with both 29%-8% (Figure 3.19 (a)) and 71%-92% (Figure 3.19 (b)) concatenations show large amount of decrease in extinction ratio away from the center wavelength (1550 nm). As a contrast, designs with ArMMI couplers (Figure 3.22 (c) and (d)) demonstrate much less extinction ratio wavelength dependence, benefiting from the broadband coupling ratio properties. Design in ArMMI couplers with 71%-92% concatenation (Figure 3.22 (c)) show the best performance with both large extinction ratio and wavelength insensitivity. The degraded performance of ArMMI design with 29%-8% concatenation (Figure 3.22 (d)) mainly results from the increased loss of the couplers with larger bend angles.

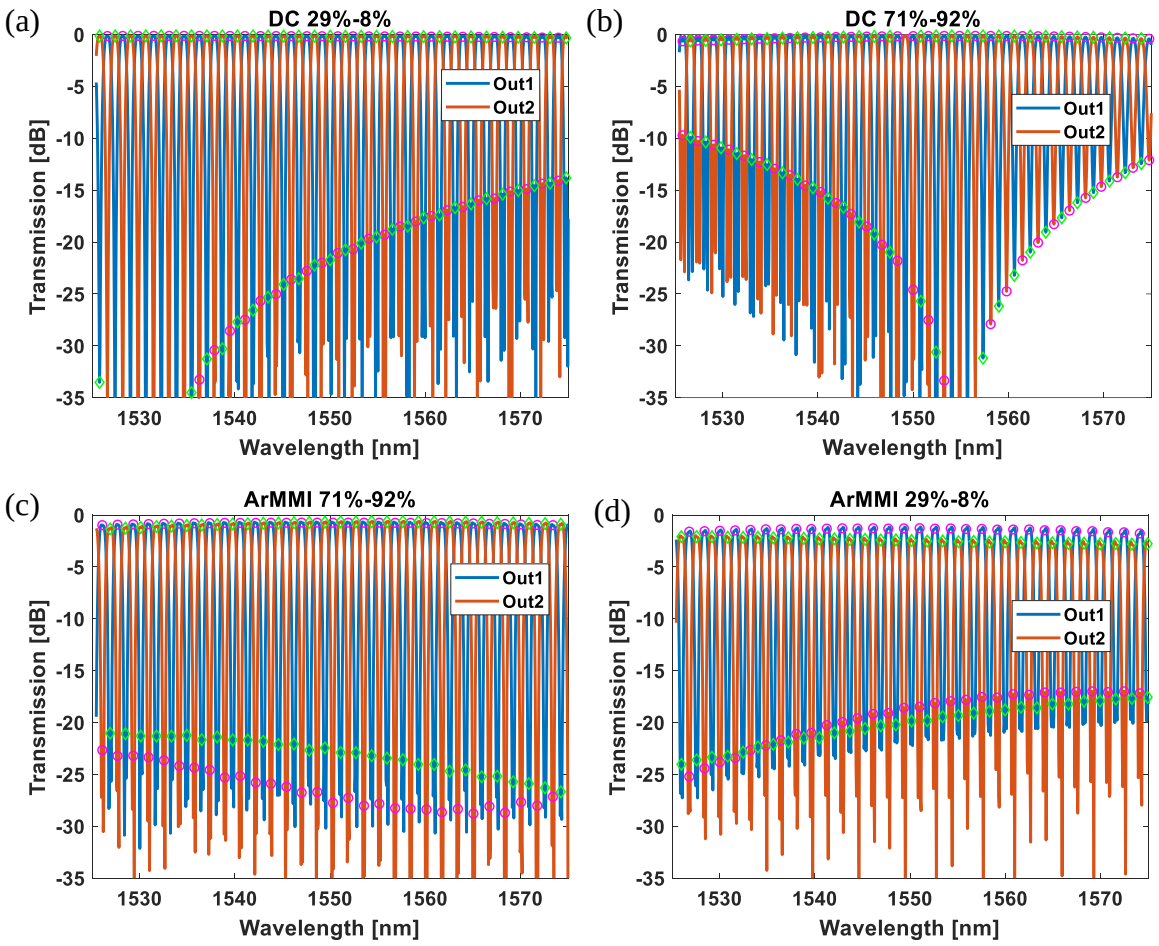

Figure 3.22 The numerical modeled output spectra of the 2-channel wavelength filter designed with both directional couplers (a, b) and ArMMI couplers (c, d).

The 2-channel wavelength filter designs were fabricated in a commercial foundry run using 180 nm process. The layout is shown in Figure 3.23. We only adopted the 29%-8% concatenation design (Figure 3.19 (a)) for our test.

Figure 3.24 show the measured output spectra for our test designs with both directional couplers (Figure 3.24 (a)) and ArMMI couplers (Figure 3.24 (b)) in the 29%-8% concatenation scheme, with markers showing the extinction ratios. The measured spectra agree with the modeled results shown in Figure 3.22. From the comparison, it can be seen that wavelength filters designed with ArMMI couplers are of less spectral dependence. Furthermore, as mentioned in the former modeling parts, the design with

ArMMI couplers in 71%-92% concatenation scheme is expected to possess better performances in terms of loss, extinction ratio, and wavelength insensitivity than in 29%-8% concatenation scheme.

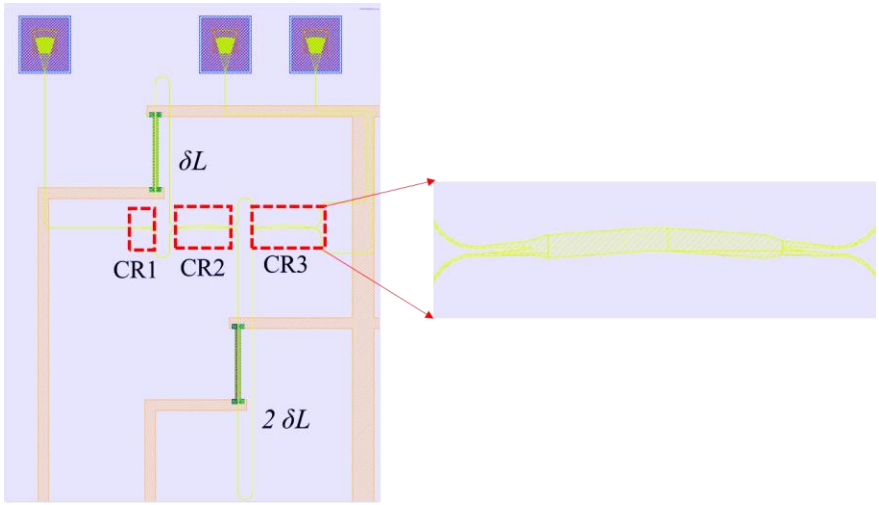

Figure 3.23 Layout of the tested 2-channel wavelength filter. Zoom-in view shows one ArMMI coupler.

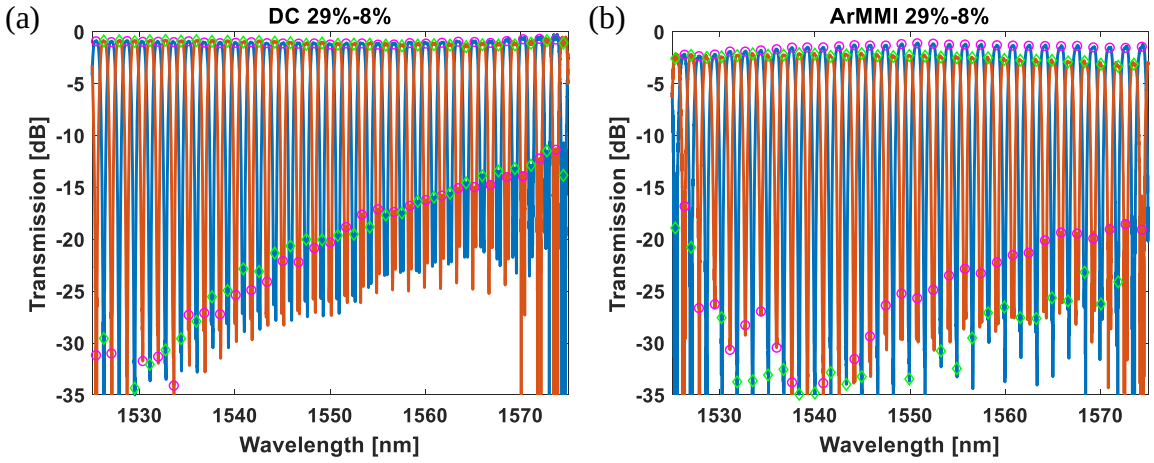

Figure 3.24 Measured output spectra of the 2-channel wavelength filter designed with: (a) directional couplers, and (b) ArMMI couplers.

In summary, in this section the proposed new ArMMI couplers are demonstrated with both numerical modeling and experimental characterization results to be implemented in cascaded Mach-Zehnder wavelength filters for WDM (de-)multiplexing to improve the working bandwidth.

3.6 Summary

To summarize, in this chapter we have proposed and demonstrated a new angled MMI coupler design to achieve arbitrary coupling ratio over wide operating bandwidth.

Theoretical analyses, including physical principle, mathematical derivation, and numerical simulation, were presented in detail for the new design proposal, modeling, and parameter optimization.

Experimental characterizations on the fabricated devices confirm improved fabrication tolerance compared to the conventional device while retaining high level of broadband achromaticity. One promising application for a 2-channel cascaded Mach-Zehnder wavelength filter was numerically studied and experimentally implemented. The devices are readily implemented in PIC designs that are compatible with commercial SOI foundry process and pose a viable, wideband alternative to conventional directional couplers.

Chapter 3, in part, is a reprint of the material as it appears in 2018 Conference on Lasers and Electro-Optics (CLEO), pp. 1-2. IEEE, 2018, titled "Arbitrary Ratio, Wavelength-insensitive 2× 2 MMI Coupler in SOI with Enhanced Fabrication Tolerance", by Jin Zhang, Liangshun Han, Bill Ping-Piu Kuo, and Stojan Radic. Chapter 3 also contains in part materials accepted for publication as it may appear in the IEEE/OSA Journal of Lightwave Technology, titled "Broadband Angled Arbitrary Ratio MMI Couplers in SOI with Enhanced Fabrication Tolerance", by Jin Zhang, Liangshun Han, Bill P.-P. Kuo, and Stojan Radic. The dissertation author was the primary investigator, and the primary author of these articles.

Chapter 4 Ge-on-Si Avalanche Photodiode

As mentioned in Chapter 1, avalanche photodiode (APD) with its internal multiplication gain is an ideal option for improving the receiver sensitivity and dynamic range with concomitant increases in loss margins and decreases in the power consumption of the detection system compared to pin photodiodes [55]. This chapter focuses on the design and characterization of Ge-on-Si APD devices with foundry-compatible fabrications.

In this chapter we will explain how an APD works and what are the important parameters for evaluating and optimizing its performances. We will present the major design approaches of the APD device relying on foundry fabrication afterwards, followed by the fabricated APD device characterizations including DC opto-electrical, small signal S-parameter, and noise measurements. Moreover, the APD devices are evaluated in high-order modulation detection experiments of both PAM4 and 16QAM with further analyses on the performance improvements with gain.

4.1 Background

We will first overview the physics that hold significant importance in designing APD devices.

4.1.1 Impact Ionization

A photodetector is an opto-electric device that converts light photons into electric current. The photocurrent generation mechanism of an APD is the same as that of a normal photodiode: photons incident in the device generate electron-hole pairs in the absorption layer, on condition that the photons have enough energy larger than the bandgap of the absorbing materials.

While the mechanism by which carriers are generated in an APD is the same as a photodiode, APD has unique function to multiply the generated carriers. When these generated free carriers (electrons and holes) are accelerated by a high electric field in the depletion layer with a reverse voltage till they gain sufficient energy, they promote another electron (hole) from the valence (conduction) band into the conduction (valence) band in a process called impact ionization. It is an important charge generation mechanism which occurs in many semiconductor materials. Both the energy and momentum are conserved during this process. The consecutive generation of electron-hole pairs may repeat several times, causing an incident photon to generate multiple electron-hole pairs. Consequently, these consecutive impact ionization events produce avalanche multiplication gain in APD devices.

The minimum energy required for impact ionization is defined as the ionization threshold energy E_i, which depends on the band structure and band gap of the material. To have the impact-ionization effect to occur, the carrier energy must exceed the ionization threshold energy. While practical modeling on determination of E_i depends on many complex factors, it has been shown that the minimum energy required for the particle to initiate an ionization is $1.5E_g$ under condition that the effective masses of both holes and electrons are assumed equal, where E_g is the bandgap [56].

The ionization rates (or coefficients) for electrons and holes, denoted respectively by α and β, are defined as the reciprocal of the average distance traveled by an electron or a hole to create an electron-hole pair measured along the direction of the electric field [57], which are important factors in determining the multiplication mechanism. In general, the ionization rates depend not only on the local electrical field but also on the 'history' of the

particle. Thus a 'non-local' ionization model is needed to accurately model the impact ionization effects. In the meanwhile, a local model in which the ionization rates depend only on the local electrical field serves sufficiently as a first approximation. Mathematically, the ionization rates satisfy Chynoweth's law and are given in [58] as:

$$\alpha = a_n \exp\left(-b_n / E\right) \tag{4-1}$$

$$\beta = a_p \exp\left(-b_p / E\right) \tag{4-2}$$

where $a_{n,p}$ and $b_{n,p}$ are material-specific constants and E is the electric field.

The ratio between the hole and electron impact ionization rate is referred as the impact ionization ratio, or k-value, as:

$$k = \frac{\beta}{\alpha} \tag{4-3}$$

It is preferred to have either electrons ($\alpha \gg \beta$) or holes ($\beta \gg \alpha$) to enter the high electric field region to generate strong impact ionization to lower the multiplication noise, which would be talked in detail in the following 4.1.3 section.

4.1.2 Multiplication Gain

The consecutive chain of impact ionization events as stated in section 4.1.1 produce avalanche multiplication gain in APD devices, which is defined as the ratio of the current flowing through the device in the presence of impact ionization to the current in the absence of carrier ionization under identical conditions. In the following text, we use a diode model in the way that the electron will travel in the electric field to the right and the hole to the left (see Figure 4.1). After a transmission distance of dx in the electric field, the electron will get an average of αdx ionization collisions and the hole will create an average of βdx collisions, which generate additional electron-hole pairs and achieve gain consecutively.

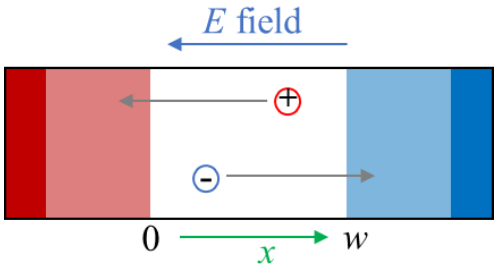

Figure 4.1 Schematic of diode model used and the multiplication region boundary conditions

For the pure electron-initiation case where only electrons are initially entering the high electric field region, the avalanche gain is given by: [57]

$$M_n = \left\{1 - \int_0^w \alpha \exp\left[-\int_0^x (\alpha - \beta)dx'\right]dx\right\}^{-1} \qquad 4\text{-}4$$

where w is the width of the electric field multiplication region (see Figure 4.1).

Similarly, the pure hole-initiated avalanche gain is given by:

$$M_p = \left\{1 - \int_0^w \beta \exp\left[\int_x^w (\alpha - \beta)dx'\right]dx\right\}^{-1} \qquad 4\text{-}5$$

The avalanche breakdown voltage is defined as the voltage at which the multiplication goes to infinity and can numerically be found by equating to zero the denominator of Eq. 4-4 and Eq. 4-5.

For the more general cases, where electrons and holes both participate in the ionization initiation process, the multiplication $M(x)$ generated at position x as a result of one initial electron-hole pair could be written as: [59]

$$M(x) = 1 + \int_0^x \alpha M(x')dx' + \int_x^w \beta M(x')dx' \qquad 4\text{-}6$$

By solving this equation, $M(x)$ can be eventually expressed as:

$$M(x) = \frac{\exp\left[-\int_x^w (\alpha - \beta)dx'\right]}{1 - \int_0^w \alpha \exp\left[-\int_{x'}^w (\alpha - \beta)dx''\right]dx'} \quad 4\text{-}7$$

4.1.3 Multiplication Excess Noise

Another factor that forms one important design consideration is the excess noise, due to its degradation in the signal noise ratio (*SNR*). As explained by McIntyre's classical noise model [59], the ionization rate of each carrier is not uniform and has statistical fluctuations, making impact ionization a stochastic process. Multiplication noise known as excess noise (relative to shot noise) is therefore added during the multiplication process, which is represented by the excess noise factor given by: [59]

$$F(M) = M \cdot k + (1-k) \cdot (2 - \frac{1}{M}) \quad 4\text{-}8$$

where M is the mean multiplication gain and k is the impact ionization ratio as defined in Eq. 4-3. It should be pointed out that the deduction of Eq. 4-8 is based on the local model of impact ionization and assumes uniformity of the multiplication region.

The excess noise factor is plotted in Figure 4.2 as a function of multiplication gain (Eq. 4-8) for various values of k-factor. It can be seen that the excess noise at a given value of M is lower if it is arranged in a way that most of the carriers entering the high-field region are the ones of the stronger ionizing type (electrons for $\alpha \gg \beta$ case or holes for $\beta \gg \alpha$ case). Besides selecting a semiconductor material with favorable ionization k-ratio, scaling the multiplication region to exploit the non-local aspect of impact ionization forms another way to achieve lower excess noise [60], [61]. For APDs designed on Ge-on-Si platform, a lower k-factor is desirable for high-performance APDs in terms of gain-bandwidth product and the excess noise [62].

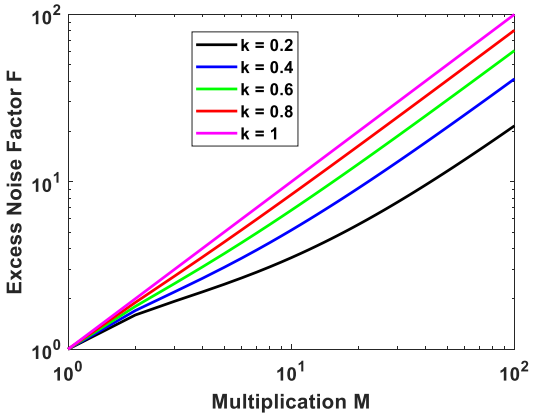

Figure 4.2 Excess noise factor (F) plotted as a function of multiplication gain (M) for various values of k.

The excess noise factor of an APD device is determined by measuring the dark / photo noise spectral density. The APD spectral noise current in dark condition is determined by its leakage current I_d under reverse bias condition. The total leakage current comprises of the surface leakage current I_{ds} and the gain multiplied bulk leakage current I_{db}, as:

$$I_d = I_{ds} + I_{db} \cdot M \tag{4-9}$$

Taking the further degradation by the excess noise factor F in Eq. 4-8 into consideration, the total noise spectral current for an APD in dark condition is given by:

$$i_N = \left[2q\left(I_{ds} + I_{db} \cdot M^2 F \right) B \right]^{1/2} \tag{4-10}$$

where q is the electron elementary charge, B is the measurement bandwidth.

When the APD is illuminated by the signal light with power P, the total noise will be the sum of the detector dark noise and the signal gain-multiplied shot noise, as expressed by:

$$i_{Nt} = \left[2q\left(I_{ds} + I_{db} \cdot M^2 F + R_0 P \cdot M^2 F \right) B \right]^{1/2} \tag{4-11}$$

where R_0 is the primary responsivity at $M = 1$.

It can be seen from Eq. 4-11 that in the absence of other noise sources, an APD provides a *SNR* result that is $F^{1/2}$ worse than a PIN detector. The noise of a practical detection system, however, is more dominated by circuit noise, transimpedance amplifier (TIA) noise, and thermal noise. Therefore, APDs can produce a better overall system *SNR* than a PIN detector in cases where the APD internal gain boosts the signal level without dramatically affecting the overall system noise.

4.1.4 Bandwidth

Another key characteristic to consider when designing an APD is the bandwidth, which is a measure of how fast the APD can transform the optical signal to electrical signal effectively and ultimately determines the bitrate of optical receivers for optical-fiber communication systems. The bandwidth of an APD is limited by a combination of the RC (Resistance-Capacitance) time constant, transit time effect, and avalanche build-up time effect [63].

The RC time constant is determined by the equivalent circuit parameters of photodiode. The intrinsic response of a photodiode can be modeled as a current source in parallel with a junction capacitor, as shown by the equivalent circuit in Figure 4.3.

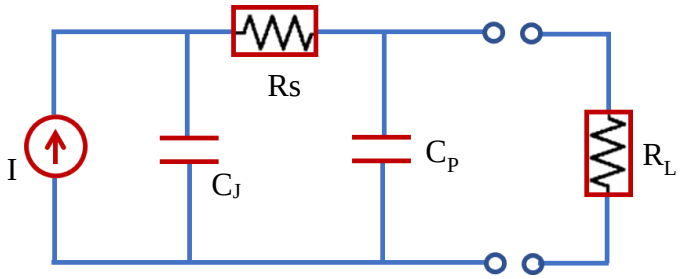

Figure 4.3 Equivalent circuit model of a photodiode

The junction capacitance C_J is defined by the edge of the depletion region (or space charge region). The series resistance R_S is due to the ohmic contact resistances and bulk

resistances. In addition, there is parasitic capacitance C_P which depends on the metallization geometry and the circuits. The electrical RC-limited bandwidth can be expressed as:

$$f_{RC} = \frac{1}{2\pi RC} = \frac{1}{2\pi(R_L + R_S)(C_J + C_P)} \quad \text{4-12}$$

where R_L is load resistance to terminate the photodiode. To improve the RC-limited bandwidth, the junction capacitance should be reduced, for example by decreasing the device length for waveguide evanescently coupled structure. This in turn, will reduce the device quantum efficiency (responsivity). Therefore, it is important to understand the performance limiting factors, and find a compromise in them.

Besides the RC limitation, the transit time that the photogenerated carriers take to travel across the device and reach the electrical contacts also limits the bandwidth. The transit-time limited bandwidth is given by:

$$f_\tau = \frac{0.44}{\tau} \quad \text{4-13}$$

where τ is the carrier transit time across the depletion region to be collected by the electrodes. In designing APD devices, it is preferred to engineer the electric field to ensure the carriers transiting at saturation velocity in the absorption region to reduce the transit time and increase the bandwidth. One advantage of the waveguide-structure APD is that the tradeoff between carrier transport distance and optical path length can be relaxed. In other words, the tradeoff between carrier transit time and responsivity can also be relaxed.

In addition to the above-described limitations, APDs have another performance-limiting factor affecting the speed: the avalanche build-up time. As carriers (electrons and holes) passing through the avalanche region collide repeatedly with the crystal lattice, it

takes a longer time for these carriers to move a unit distance than that required to move in areas outside the avalanche region. This added avalanche build-up time also slows the APD bandwidth response, especially at a higher gain.

Based on the linear-transport equations in the multiplication region of a PIN APD [64], the device bandwidth as a function of the multiplication gain has been studied with exact solutions. The results show that for DC gain $M_0 > {}^{\alpha}/_{\beta} = {}^{1}/_{k}$, the bandwidth response can be approximated by:

$$M(\omega) \approx \frac{M_0}{\left[1+\omega^2 M_0^2 \tau_1^2\right]^{1/2}} \qquad 4\text{-}14$$

where τ_1 is the effective transit time approximated by $\tau_1 \approx Nk\tau$, with τ the actual carrier transit time across the avalanche multiplication region, and N a number varying slowly between ${}^{1}/_{3}$ and 2 with different k values. M_0 is the DC multiplication gain of the APD, which is expressed for the PIN APD as:

$$M_0 = \frac{(\alpha-\beta)\exp\left[(\alpha-\beta)w\right]}{\alpha-\beta\exp\left[(\alpha-\beta)w\right]} \qquad 4\text{-}15$$

with w representing the avalanche region length (Figure 4.1).

In the case where the DC gain $M_0 < {}^{\alpha}/_{\beta}$, the bandwidth slowing effect induced by the ionization build-up time is small and the bandwidth of an APD would be mainly restricted by the transit time and RC time limitation.

4.1.5 Impact Ionization Properties of Si and Ge

There are extensive literatures on ionization coefficients of Si and Ge materials [58], [65], [66]. The a_n, a_p, b_n, b_p parameters in Eq. 4-1 and Eq. 4-2 for Si and Ge materials are summarized in Table 4.1Table 4.1.

Table 4.1 Impact ionization parameters (a_n, a_p, b_n, b_p) for Si and Ge [65], [66].

	Electric field	Electrons		Holes	
	$E(V/cm)$	$a_n(cm^{-1})$	$b_n(V/cm)$	$a_p(cm^{-1})$	$b_p(V/cm)$
Si	$1.75 \times 10^5 - 4 \times 10^5$	7.03×10^5	1.231×10^6	1.582×10^6	2.036×10^6
	$4 \times 10^5 - 6 \times 10^5$	7.03×10^5	1.231×10^6	6.71×10^5	1.693×10^6
Ge	$1.75 \times 10^5 - 6 \times 10^5$	4.9×10^5	7.9×10^5	2.15×10^5	7.1×10^5

The impact ionization coefficients of electrons (α) and holes (β) together with the ionization coefficient ratio (k-ratio) of both Si and Ge are plotted in Figure 4.4 as a function of inverse electric field intensity. It can be seen beyond doubt that Si is a more ideal material for impact ionization in that the electron ionization coefficient is significantly greater than the hole ionization coefficient ($k \ll 1$). As a result, impact ionization happened in Si is regarded as a low-noise multiplication process. In fact, Si APDs with very low excess avalanche noise are commercially available working in 600 - 900 nm wavelength range. However, with a bandgap energy of 1.12 eV (cutoff wavelength 1130 nm), Si itself cannot absorb and detect light in optical communication band.

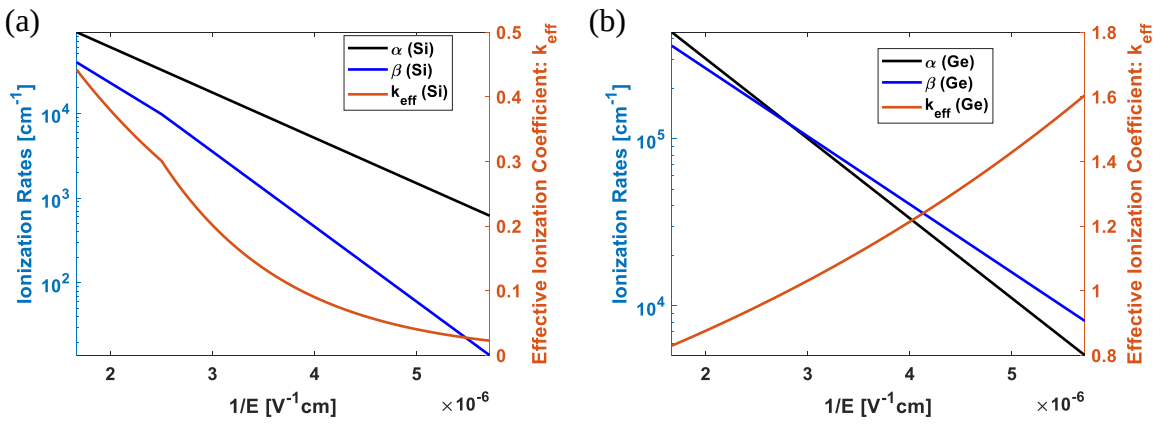

Figure 4.4 Ionization rates (left) and effective ionization index (right) versus reciprocal electric field in Si (a) and Ge (b); curves are obtained from the experimental data of [65], [66].

On the other hand, Germanium is an appealing absorbing material in the communication band for use in silicon-based PICs because it can be integrated into a CMOS line relatively easily, which is offered currently by most of the commercial silicon photonics foundry lines. The bulk Ge material with a bandgap of 0.67 eV is absorbing in the entire 1310 nm window and much of the C and L bands. Moreover, the tensile strain added during the deposition process further increases the absorption in longer wavelengths [67]. Therefore, Ge is the material of choice for light absorption in silicon photonics platform. While Ge has a relative large k value (Figure 4.4 (b)), lowering the noise of Ge APD is achievable through engineering the electric field and multiplication width to exploit the non-local aspect of impact ionization [68].

The effect that decreases the excess noise relative to the bulk material with the non-local nature of impact ionization is referred to as the "dead space" effect [69]. The dead space refers to the distance that a carrier travels before gaining the ionization threshold energy to impact ionize. When the dead space becomes a significant fraction of the multiplication layer thickness, the probability distribution function, which is the probability per unit length that a carrier ionizes at a specific distance from the injection point or the point where it is created by another impact ionization event, narrows. This in turn makes the gain process more deterministic and decreases the excess noise.

4.2 Ge-on-Si Avalanche Photodiode Design

The former section finishes the background preparations of APDs, this section will present the design and modeling of Ge-on-Si APDs. The target of this section is to design Ge-on-Si APDs relying on zero-change commercial foundry fabrication services to achieve favorable tradeoff between dark current, responsivity/gain, bandwidth and excess noise

characteristics for high speed receivers designed for high order modulation detection applications.

In terms of light coupling configurations, there are two types of light injection schemes: normal incidence [63], [70] and waveguide integration [71]. As illustrated in Figure 4.5 (a), one main problem for the normal incidence design is that it suffers from trade-offs between transit distance (speed) and absorption length (efficiency). Designing for higher bandwidth favors thinner Ge absorption layer for shorter transit time, which on the other hand results to lower absorption that decreases the responsivity. Although resonance cavity enhanced (RCE) structure [72] can be used to increase the efficiency, ultimately it is still bounded by the tradeoff. Moreover, it is not suited for large-scale PIC integration.

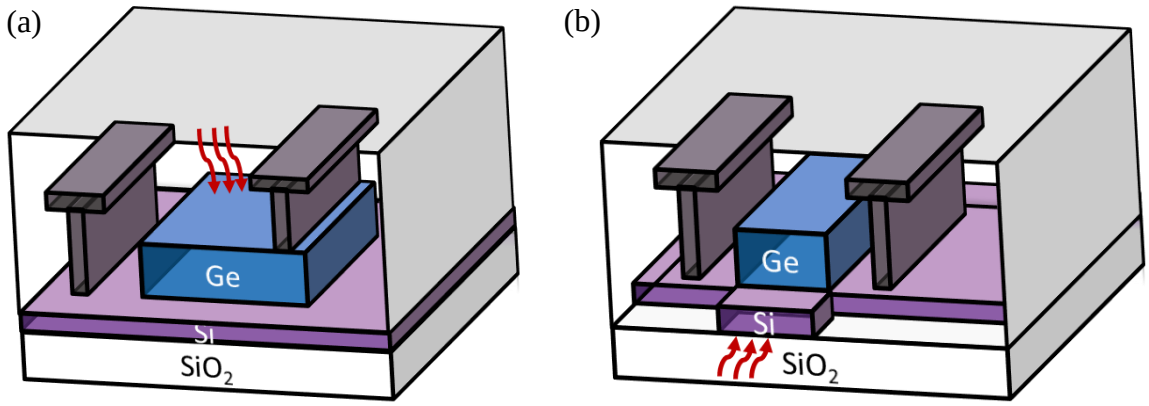

Figure 4.5 Photodetector light injection scheme: (a) vertical (b) waveguide coupling.

Waveguide integrated design (Figure 4.5 (b)), where injected light evanescently couples from low index waveguides (Si, $n = 3.44$) to high index waveguides (Ge, $n = 4.25$), as illustrated in Figure 4.6, allows for separate optimization for the absorption efficiency and the response speed. Moreover, the butt-coupled waveguide connection promises large scale PIC integration. Therefore, our APD designs presented in the following section are with waveguide integrated structure.

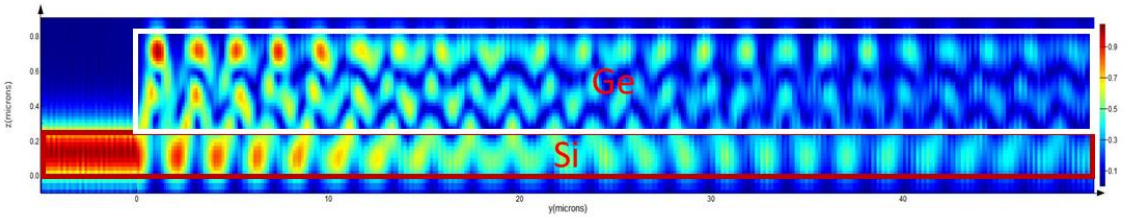

Figure 4.6 Evanescent light coupling in Ge-on-Si waveguide integrated photodetector.

A majority of demonstrations on waveguide-integrated Si-Ge APDs are based on separate-absorption-charge-multiplication (SACM) structure to reduce excess noise by confining carrier multiplication in Si to utilizing the good ionization properties of Si [63], [71], [73]–[78]. The SACM approach, however, requires epitaxial silicon growth for field control and multiplication layer formation [63], [71], [73]–[77], which is incompatible with standard photonics processes optimized for dual-polarization operation [79]. Another demonstration type [78], while requires no epitaxial silicon growth, shows limited bandwidth (~10 GHz) due to reduced drift velocity resulted from the weak electric field in the Ge absorption layer and silicon charge layer. On the other hand, while Ge APDs are generally considered to suffer from higher multiplication noise in germanium, these devices can achieve high gain using carrier multiplication close to avalanche breakdown [80], and noise could be effectively suppressed by manipulating the electric field and multiplication distribution [60], [81], [82]. Demonstrations with lateral PIN [81] and vertical PIN [82] structures all show improved sensitivity performances, however, at limited data rates of 10 Gbps.

Recognizing these limitations, we investigate the lateral PIN-based Ge-on-Si APDs fabricated in a standard silicon photonic foundry with zero process modification, which are capable of delivering high gain, large bandwidth and low noise, allowing for high-order

modulation detection of both multi-level pulse amplitude modulation (PAM) and quadrature amplitude modulation (QAM).

The schematic of the designed APD with lateral PIN junction structure is shown in Figure 4.7. A pair of shallow implants (p/n) with $10^{18} cm^{-3}$ peak impurity concentration are used to form a p-i-n junction in silicon to minimize free carrier optical absorption in contact implants (p++ / n++). The contacts reside on top of Si, which is different from the design in [81]. There are three design parameters that are of critical importance to optimize the APD performances in terms of responsivity/gain, bandwidth, and excess noise factor, which are the Ge waveguide width W, the Ge waveguide length L, and the Si intrinsic width W_i (Figure 4.7).

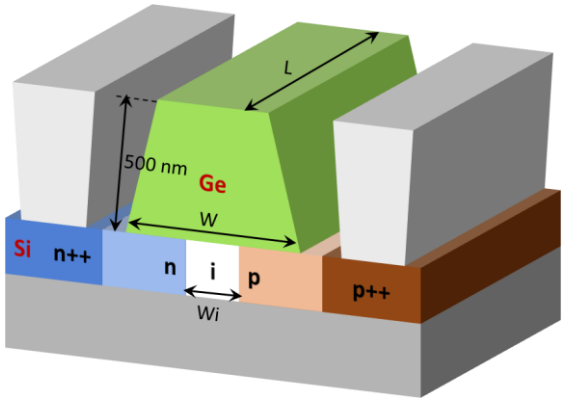

Figure 4.7 Schematic view of the designed APD with lateral PIN structure.

The primary responsivity of the APD is determined by the Ge waveguide width W and length L. The FDTD simulation results of the total absorbed power ratio inside Ge are plotted as a function of W and L in Figure 4.8 (a) and (b) separately. The total absorbed optical power increases with Ge width from 1 μm to 2 μm and then stays flattened. If we assume a quantum efficiency of $\eta = 1$, the corresponding responsivity R (defined in Eq. 4-16) for Ge waveguide with 2 μm width and 50 μm length is 0.98 A/W with the 78% absorption ratio.

$$R = \frac{I}{P} = \frac{q\eta}{h\nu} = \frac{q\eta\lambda}{hc} = \frac{\eta\lambda}{1.24}(A/W) \qquad \text{4-16}$$

Here q is the elementary charge, h is the Planck constant, ν is the photon's frequency, c is the speed of light in vacuum, and λ is the photon's wavelength.

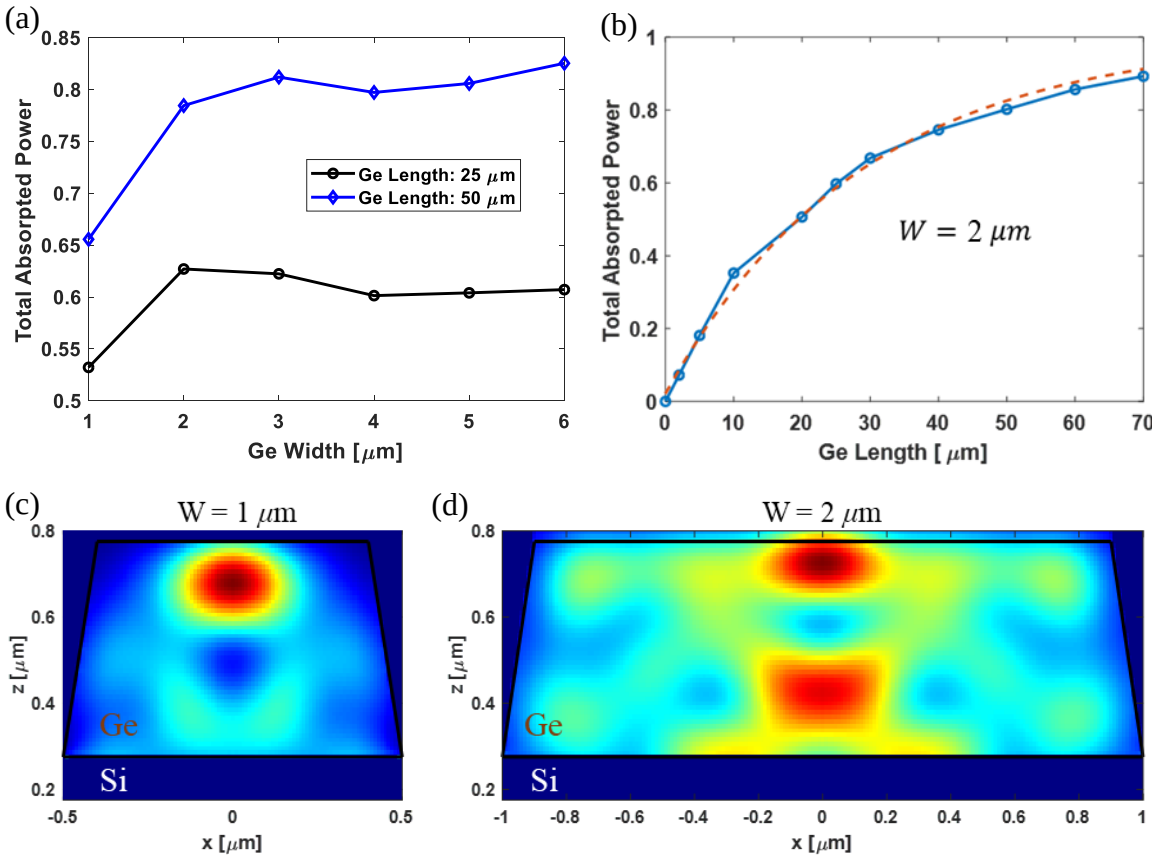

Figure 4.8 FDTD simulation results of the total absorbed power ratio as a function of (a) Ge waveguide width W and (b) length L. Optical absorption distribution inside Ge for (c) W = 1 μm and (d) W = 2 μm.

The total absorbed optical power in Ge waveguide versus waveguide length L is shown in Figure 4.8 (b), together with the $1 - \exp(-\alpha L)$ curve fitting. The good fit between the calculated data points and the exponential function indicates the evanescent coupling nature. A device length between 30 μm and 50 μm offers a great absorption efficiency while maintaining the high response speed. The overall cross-section optical

absorption distribution inside Ge for devices of length L = 50 μm, width W = 1 μm and 2 μm are illustrated in Figure 4.8 (c) and (d) respectively.

The intrinsic width in Si W_i plays vital importance in defining the multiplication performance of the APD, including gain, breakdown voltage, and excess noise factor. In order to see the effects of W_i, we did a parameterized study of the design with 1 μm width, 50 μm length and various W_i values. Figure 4.9 plots the modeled dark/photo current results and the corresponding gain responses as a function of reverse voltages with various intrinsic width W_i under -20 dBm input power. The breakdown voltage increases with the intrinsic width due to the larger depletion region. As the intrinsic width increases, the curve reaching breakdown becomes more gradual, which is a performance merit in consideration of the system bias stability. The maximum achievable gain increases with larger intrinsic width due to the enlargement of the multiplication region, as can be seen by the field distributions in Figure 4.10 and the impact generation distributions in Figure 4.11. It should be pointed out that the modeled maximum gain point may not be exact due to the convergence issue with numerical simulation but serves as a good approximation.

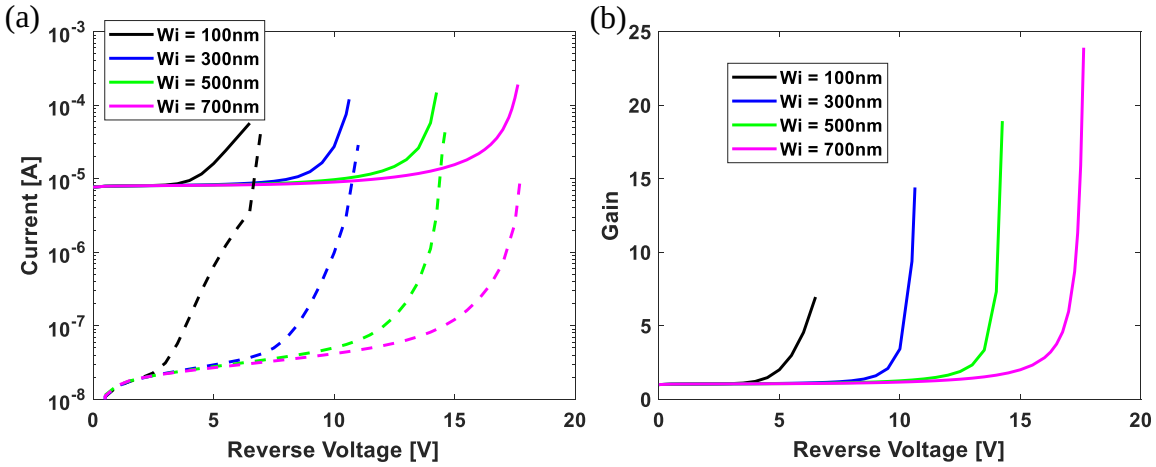

Figure 4.9 Simulation results of the dark/photo current (a) and gain (b) with various intrinsic width *Wi* as a function of reverse bias voltage.

Figure 4.10 (a-d) plot the modeled electric field distributions with quiver arrows representing the vector field directions at the breakdown voltage under various intrinsic width W_i, showing that the high electric field region is mainly distributed within the lower 200-nm Ge at the Ge-Si interface. This electric field confinement results in the impact ionization events restraining at the lower 200-nm Ge (Figure 4.11), which effectively decreases the excess noise relative to the bulk material with the non-local nature of impact ionization called the "dead space" effect [69].

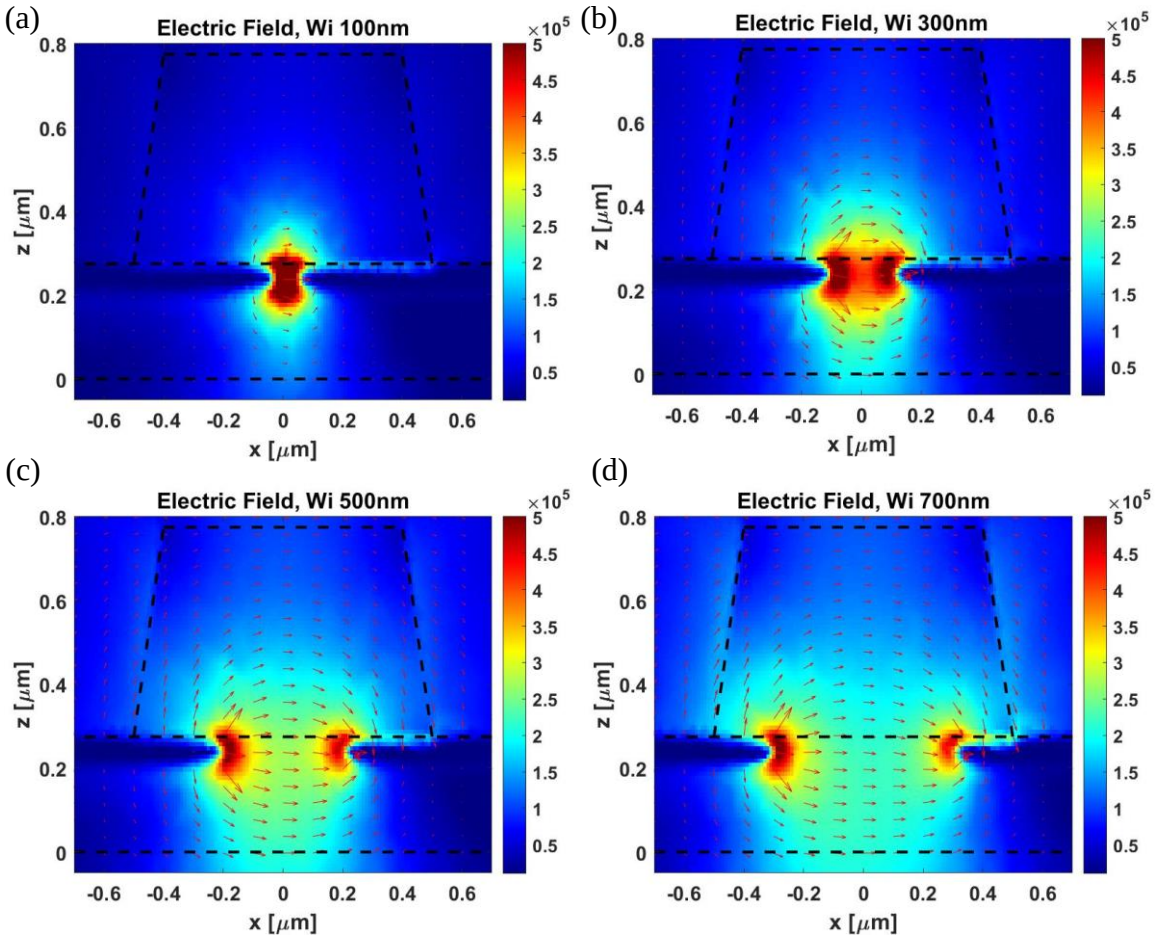

Figure 4.10 Simulation results of the electric field distribution for designs with various *Wi*: (a) *Wi* = 100 nm; (b) *Wi* = 300 nm; (c) *Wi* = 500 nm; (d) *Wi* = 700 nm.

When the intrinsic width is too narrow as for the $W_i = 100\ nm$ design shown in Figure 4.10 (a) and Figure 4.11 (a), there exists limited high electric field depletion area

for carrier impact ionization to happen, limiting the achievable avalanche multiplication gain (Figure 4.9 (b)). On the other direction, if the intrinsic width is too large as illustrated in Figure 4.10 (d) and Figure 4.11 (d) for the $W_i = 700\ nm$ design, the Ge edge corner at the Ge-Si interface would suffer from high electric field, causing the device susceptible to edge breakdown.

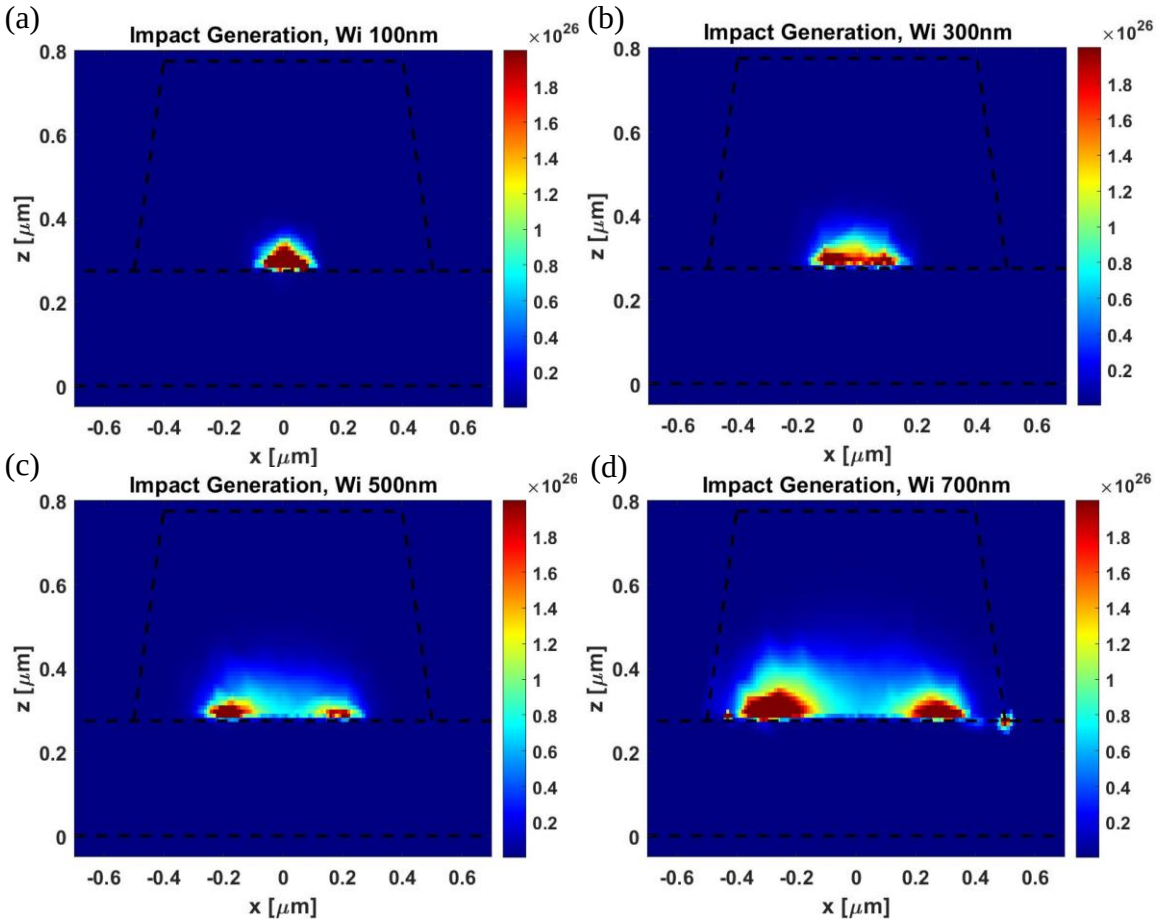

Figure 4.11 Simulation results of the impact generation distribution for designs with various *Wi*: (a) *Wi* = 100 nm; (b) *Wi* = 300 nm; (c) *Wi* = 500 nm; (d) *Wi* = 700 nm.

With all the afore-mentioned design considerations, we put two designs to get fabricated in a commercial foundry run. The design parameters for the fabricated Ge-on-Si waveguide APDs are summarized in Table 4.2.

Table 4.2 Lateral PIN APD device design parameters

Designs	Width W [μm]	Length L [μm]	Intrinsic Wi [nm]
APD1	1	50	120
APD2	1	50	500

4.3 APD Experimental Characterizations

The device fabrication is implemented at Institute of Microelectronics (IME), Singapore using 0.18-*u*m silicon photonics process without Si epitaxial growth. The scanning electron microscope (SEM) image of one fabricated device is shown in Figure 4.12 (a). The device-under-test also includes a Si waveguide taper for efficient evanescent coupling of the input light to the Ge crystal, as well as Al metal connection to the exposed metal pads. Grating couplers (SEM image shown in Figure 4.12 (b)) are used for light coupling to the APD devices.

(a) (b)

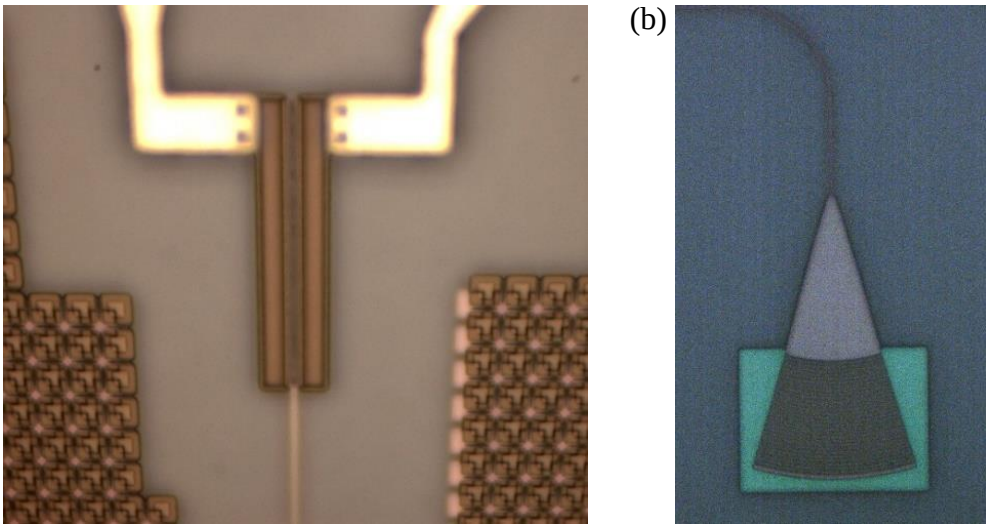

Figure 4.12 SEM image of one fabricate APD device (a), and the grating coupler connected for light coupling (b).

4.3.1 Dark/Photo Current and Responsivity/Gain Performances

The dark current and photo current vs. voltage (VI) characteristics of the fabricated APD devices are measured under room temperature condition. For photocurrent measurements and gain calculations, we use a coupled laser power of -20 dBm. The fiber-GC coupling loss at 7 dB/facet has been de-embedded from the optical input power. The devices are contacted using a set of multi-contact wedge (MCW) probe needles from GGB industries to apply the bias voltage.

Dark current vs. reverse bias voltage results for APD1 and APD2 are shown in Figure 4.13 (a). Both devices show a low dark current of less than 20 nA under bias voltage within 3V and the typical increase of the dark current with further increasing the bias voltage. We measure the device dark current up to 100 μA and define the corresponding voltage as the breakdown voltage. The breakdown voltage of APD1 is 8.3 V and increases to 12.5 V for APD2, which agrees with our model simulation in section 4.2.

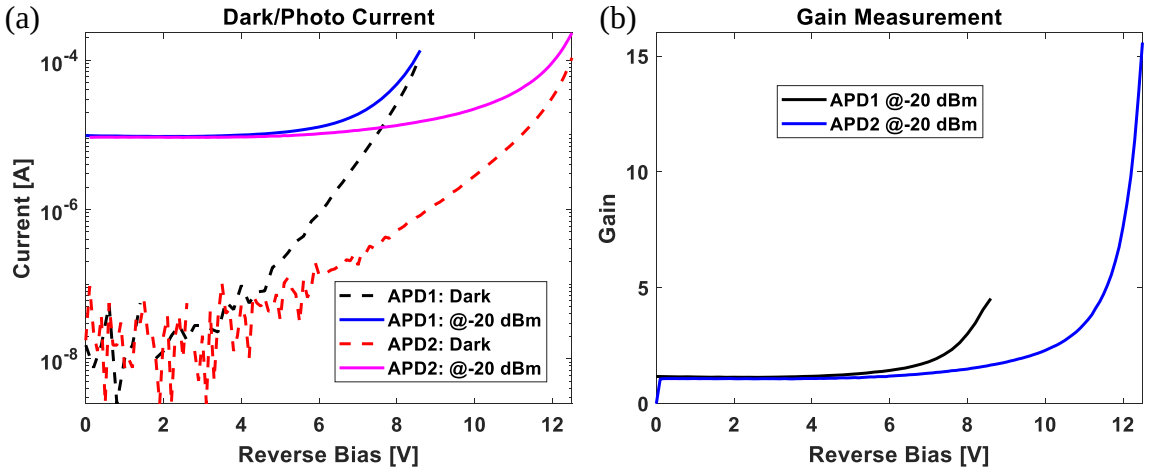

Figure 4.13 Measured dark and photo current (a) and extracted multiplication gain (b) versus reverse bias voltage for fabricate APD devices.

The photo current measurements with -20 dBm coupled light power for APD1 and APD2 are also shown in Figure 4.13 (a). Based on the dark/photo current measurements,

the multiplication gain for the APD devices can be calculated (Figure 4.13 (b)). The multiplication-gain under reverse bias voltage V is defined as the ratio between the photo current measured at V and the photo current measured at V_0. V_0 is the corresponded voltage at unity gain, where the second derivative of the photo current with respect to bias voltage equals zero. The extracted primary responsivity at unit gain for both devices are within 0.9 - 0.95 A/W range. Since the amount of light coupled into the device is referenced with the nearby directly connected grating couplers, there exist a certain ambiguity in the exact coupled light power and variations along the time period to sweep the bias voltages, as illustrated in Figure 4.14 for the monitored coupling loss variations during the measurement. As a result, there exist the variation values in the 0.9 - 0.95 A/W range for the calibration of the APD primary responsivity.

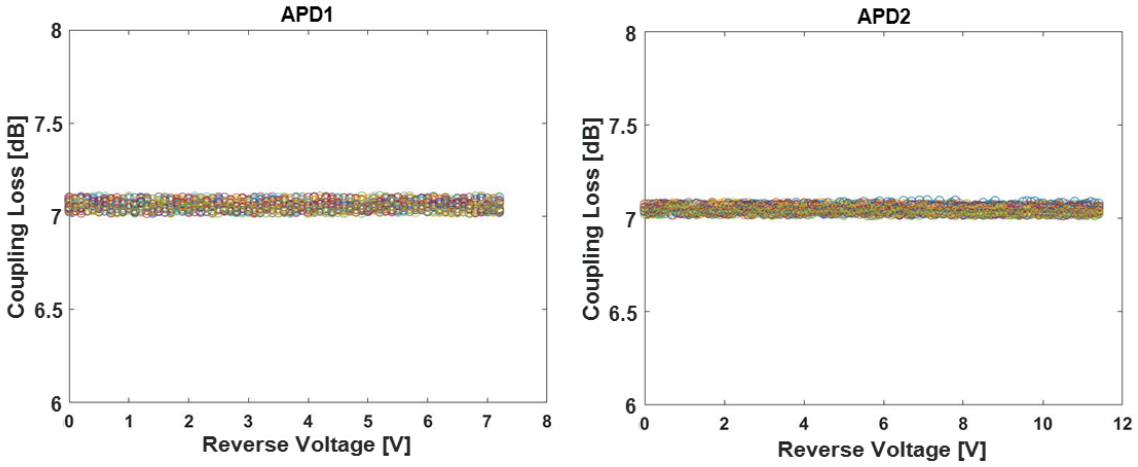

Figure 4.14 Monitored fiber array-grating coupler coupling loss variations during the time period of the experimental characterizations.

The measured multiplication gain (Figure 4.13 (b)) of APD1 under -20 dBm coupled light power is 5 and increases to 16 for APD2, which is attributed to the enlargement of the intrinsic multiplication region width, agreeing with the numerical modeling in section 4.2.

Moreover, we characterized the APD responses under different input power levels to show its linearity performance. Here, linearity is defined as the output photocurrent response against optical input power. In general, there are three factors degrading the linearity of APDs and that of other photodiodes at high input power level, which are thermal issue during high-power operation, the space-charge effect, and the phonon scattering effect.

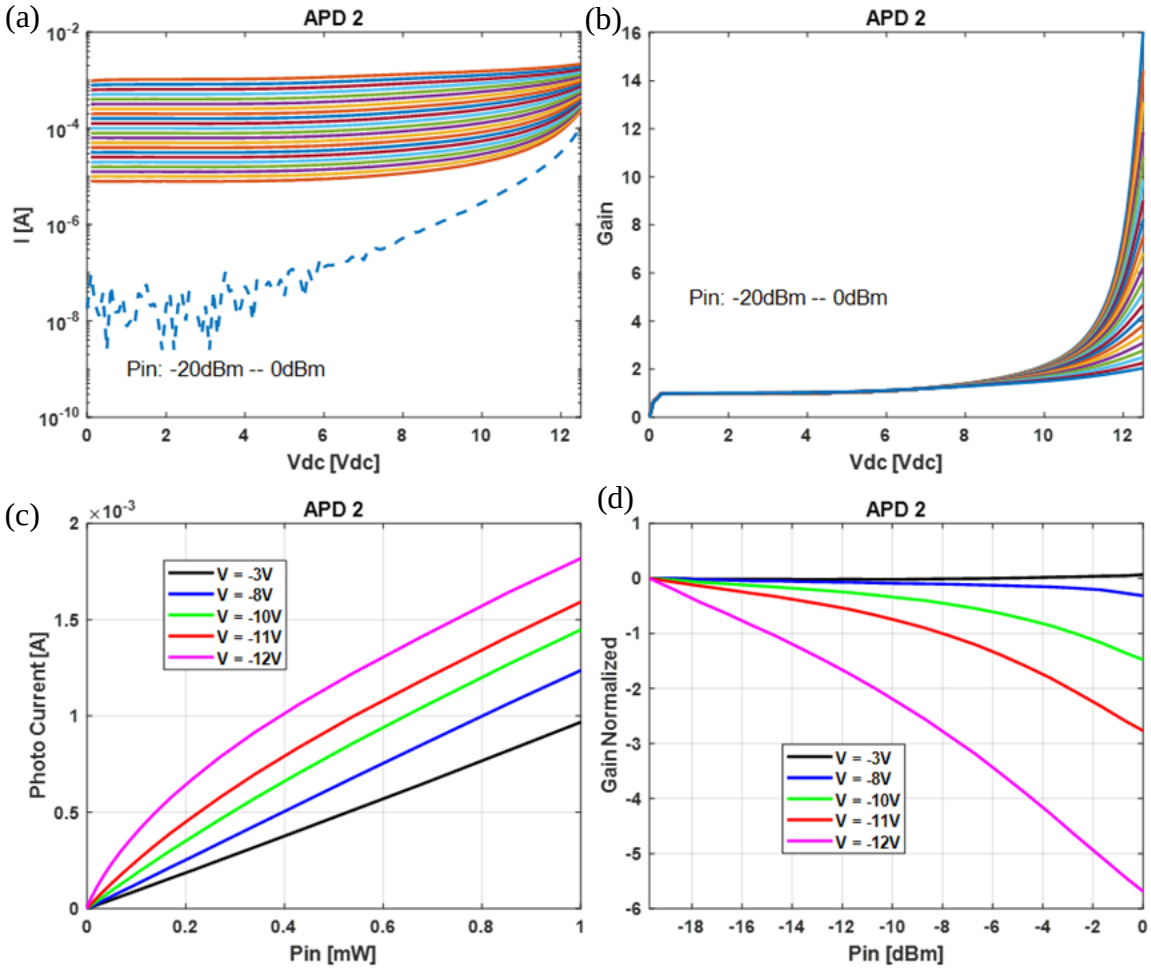

Figure 4.15 Input power dependence of output photocurrent and gain for APD 2.

Figure 4.15 (a) plots the photocurrent versus reverse voltage response for APD2 with input power varying from -20 dBm to 0 dBm. The corresponding multiplication gain are extracted and plotted in Figure 4.15 (b), showing the gain reduction with higher input

power. Figure 4.15 (c) illustrates the photocurrent versus the input power in the linear scale and Figure 4.15 (d) plots the dB-scale multiplication gain reduction as a function of input power, under various bias voltages. The 1-dB compression points where the optical input power provides an output photocurrent compressed by 1 dB from the ideal linear response are -15 dBm (@-12V), -8 dBm (@-11V) and -3 dBm (@-10V), respectively.

4.3.2 Bandwidth and Gain-Bandwidth Performances

The measurement setup for the frequency domain characterizations is shown in Figure 4.16. Small signal S21 parameters are measured using an Agilent high speed vector network analyzer (VNA). The bias voltage is applied using a DC power supply connected to the internal bias-T of the VNA. Cascaded erbium doped fiber amplifier (EDFA) and variable optical attenuator (VOA) are connected for controlling the input power coupled to the APD. The APDs are connected to one port of the VNA by high frequency cables and a Cascade GSG probe card specified for DC to 40 GHz application. Before the S parameter measurement of the device, the setup is calibrated with an impedance standard substrate (ISS) using the short-open-load-thru (SOLT) process including the high frequency cable and probe card, which ensures greater accuracy and better repeatability in S parameter measurements with VNA.

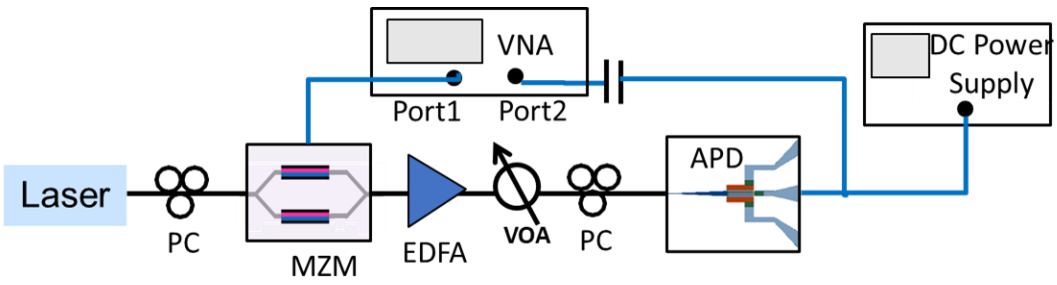

Figure 4.16 Setup for bandwidth measurement (PC: Polarization Controller; MZM: Mach-Zehnder Modulator; EDFA: Erbium Doped Fiber Amplifier; VOA: Variable Optical Attenuator; VNA: Vector Network Analyzer).

Figure 4.17 shows the normalized S21 measurement results for APD1 and APD2 at various bias voltages separately. The measurements are performed from 40 MHz to 40 GHz with 1601 points and an averaging factor of 100. The normalization is done with reference to responses at 40 MHz. The frequency response of the connected Mach-Zehnder modulator (MZM) has been de-embedded from the recorded data. The bandwidth of APD1 is more than 35 GHz under avalanche mode with various multiplication gain values. We measure the S21 parameter up to 8 V bias voltage corresponding to a gain value of 2.9, till which level no slowing effect of carrier build-up time is observed. For APD2, the bandwidth first increases to 33 GHz at 9 V bias, then decreases to 26 GHz with further raising the bias voltages. The decrease of the response speed with higher multiplication gain is attributed to the longer avalanche build-up time [64].

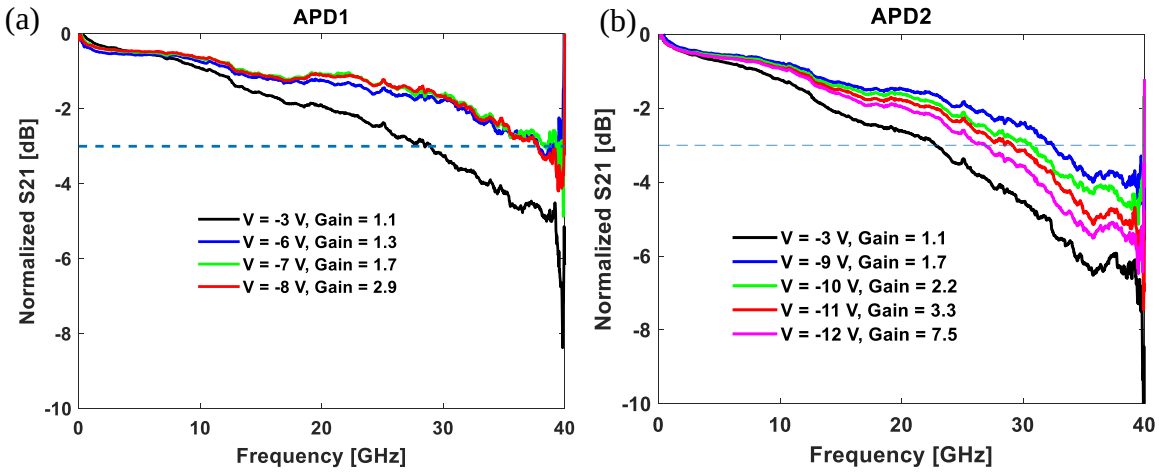

Figure 4.17 Measured small signal bandwidth (S21) of fabricate APD devices under various reverse bias voltage and corresponding gain: (a) APD1; (b) APD2.

Based on the measured frequency characteristics, the -3 dB bandwidth are extracted and plotted against gain in Figure 4.18 (a). The resulting gain-bandwidth characteristics are shown in Figure 4.18 (b) for both APD1 and APD2 devices, achieving >100 GHz gain-bandwidth product for APD1 and 200 GHz gain-bandwidth product for APD2. It should

be noted that the bandwidth characterizations are measured up to 8 V (breakdown at 8.3 V) for APD1 and 12 V (breakdown at 12.5 V) for APD2, indicating that the gain-bandwidth product should be even higher at breakdown points.

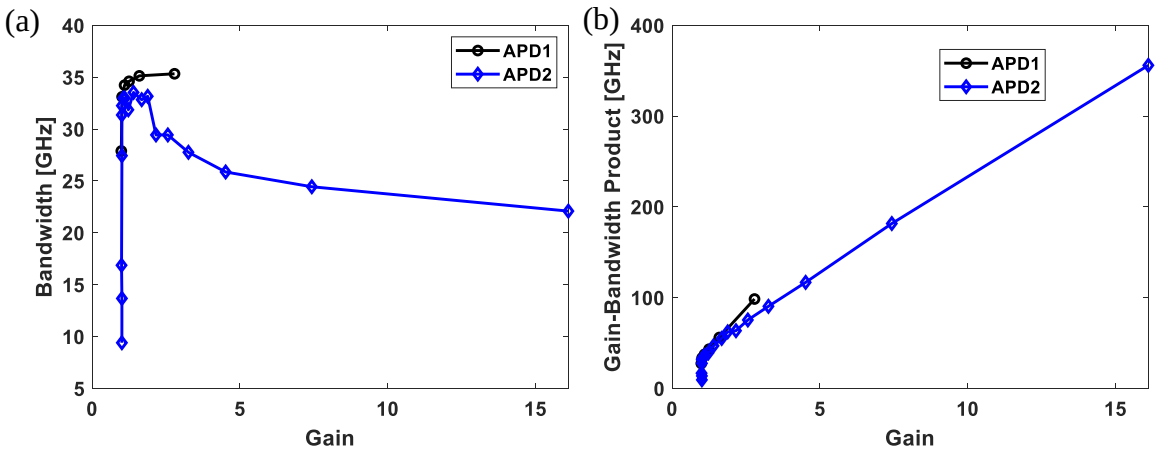

Figure 4.18 Extracted bandwidth (a) and gain-bandwidth product (b) of fabricate APD devices as a function of multiplication gain.

Besides measuring the S-parameters using the Mach-Zehnder modulator and high speed VNA, the bandwidth can also be determined through measuring the impulse responses of the APD devices. A mode locked laser with <100 fs pulse width and 100 MHz repetition rate is used as the optical pulse source. The electric current of the APD is recorded by a 50 GHz digital communication analyzer (DCA) connected via high frequency cable and a Cascade GSG probe card. A bias-T is connected in between the probe card and high frequency cable to apply the bias voltage. The impulse response of APD1 under various bias voltages is shown in Figure 4.19 (a). The negative sign in the recorded voltage is introduced by the reverse voltage applied. The calculated frequency response is plotted in Figure 4.19 (b), showing consistency with the bandwidth results measured with VNA.

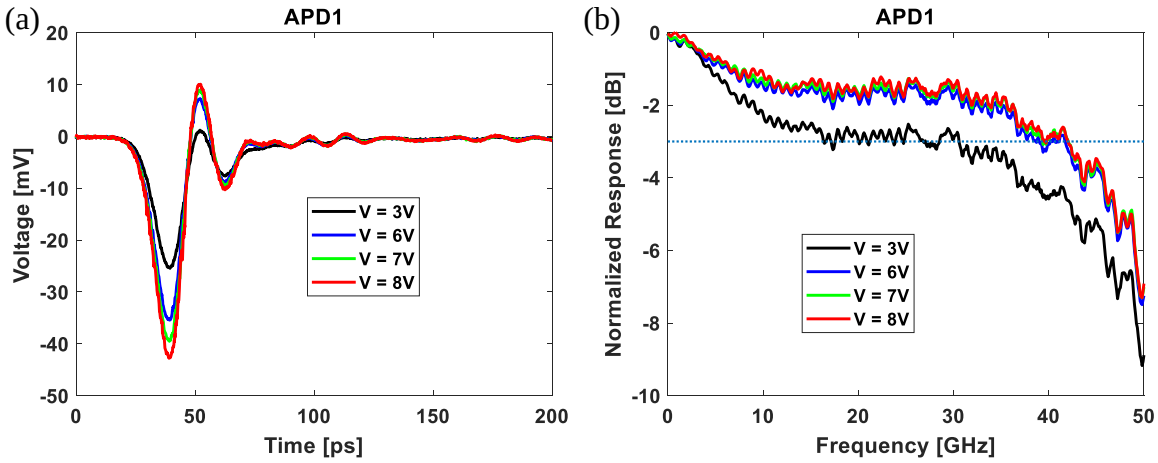

Figure 4.19 Measured impulse response (a) and calculated frequency response (b) of APD1 with various bias voltages.

4.3.3 Excess Noise Performances

The multiplication excess noise performances of the APDs are measured with an electrical low-noise amplifier and electrical signal analyzer (ESA, N9030A PXA Signal Analyzer) with setup connections shown in Figure 4.20. An external cavity laser with low RIN noise is used as the light source and coupled to the APD devices with an VOA to vary the input power. The dominant noise source of the measurement system is the shot noise, which enables accurate excess noise factor extraction.

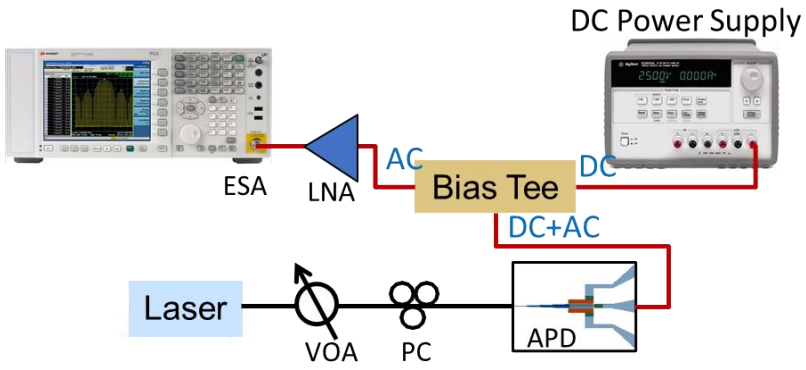

Figure 4.20 Setup for APD noise measurement (LNA: low noise amplifier).

The noise PSD of both dark current and photo current are captured in 700 MHz band with a resolution frequency of 10 kHz and a radio frequency of 1 Hz. The stability of

RIO laser is high, thereby its fluctuation has no effect on the APD noise measurement. There are no control and monitoring of the temperature during the measurement. It is nevertheless desirable to measure the noise and the signal delivered by APDs in relative short time to have the smallest variation of temperature between the two measurements.

The measured noise power is given by Eq. 4-17 in the avalanche multiplication regime, as [83]:

$$N_t = 2q\left[I_{ds} + (I_{db} + I_p)M^2F \right]\Delta f R_t + N_{thermal} + N_{RIN} \qquad 4\text{-}17$$

where q is the elementary charge, I_{ds} is the surface leakage current, I_{db} is bulk leakage current, I_p is the photo current at unit gain, M is the corresponding multiplication gain, Δf is the bandwidth, and R_t is the system impedance. $N_{thermal}$ and N_{RIN} are the thermal noise and laser relative intensity noise (RIN) of the light source, which can be de-embedded with subtraction from measurements under different input power levels at unit gain. The excess noise factor F can be expressed by the gain M and the ratio of the hole-electron ionization coefficients k_{eff}, as in Eq. 4-8 in section 4.1.3.

The measured excess noise factor F as a function of multiplication gain M is shown in Figure 4.21 for APD2. The results are deduced from measurements at 1549.3 nm wavelength with an input optical power of -20 dBm up to a bias voltage of 12.2 V. The effective relative ionization ratio k_{eff} deduced by fitting F with M using Eq. 4-8 is within 0.15 – 0.25. The measured k_{eff} results are less than bulk Ge [66], which is attributed to the localization of the avalanche multiplication (Figure 4.11) [84], resulting in a noise power spectral density reduction by 64% at a gain of 10 with respect to the noise expected for bulk Ge.

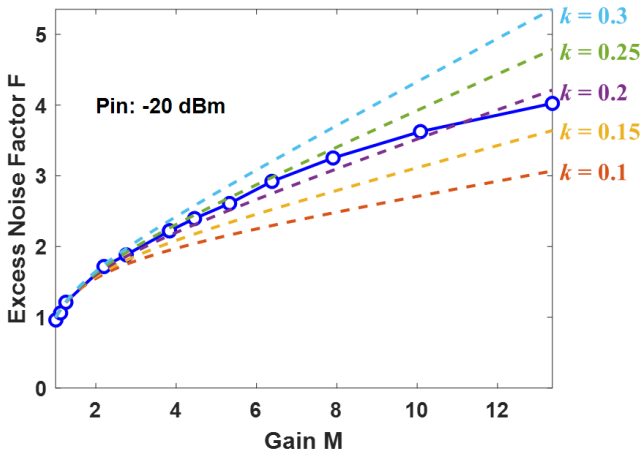

Figure 4.21 Measured excess noise factor plotted as a function of corresponding gain for APD2.

4.4 APD PAM4 Channel Reception Test

In section 4.3 we present the stationary VI-characteristics (dark current, photo current, multiplication gain), the dynamic characteristics (bandwidth), and the excess noise characteristics of the APD devices. This section further investigates the dynamic properties of APDs with TIA-less PAM4 channel reception experiment.

A PAM4 signal uses four signal levels for transmission (Figure 4.22). Within each clock period, two bits of logic information, that is, 00, 01, 11, and 10, can be transmitted. Therefore, under the same baud rate, the bit rate of a PAM4 signal is twice that of an NRZ signal, doubling transmission efficiency and reducing transmission costs.

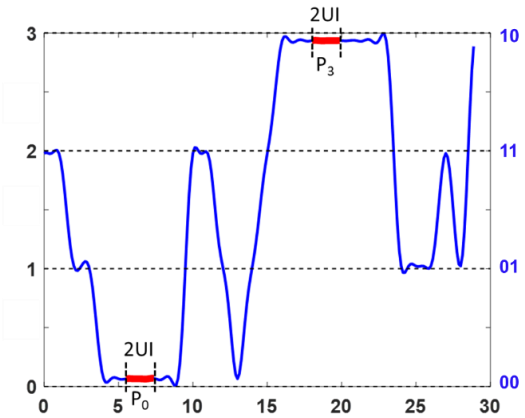

Figure 4.22 PAM4 signal illustration. Marked P0 and P3 are defined by IEEE for OMA test.

The experiment setup is shown in Figure 4.23. No TIA is used during the experiment. The PAM4 test signal is generated by a 64 GS/s digital-to-analog converter (DAC) with 16-GHz bandwidth and is amplified to drive a LiNbO3 Mach-Zehnder modulator (MZM) with a 3-dB bandwidth of 30 GHz. A 1549.3 nm external cavity laser with RIN < -140 dBc/Hz is used for supplying the optical carrier. The output of the MZM is amplified by an erbium-doped fiber amplifier (EDFA) and attenuated by a variable optical attenuator (VOA) for controlling incident power into the APD device. The photocurrent output of the APD is received by an equivalent-time oscilloscope (Keysight 86100C) with 50 GHz bandwidth via a Cascade GSG probe card and a bias-tee, through which the desired reverse bias is applied.

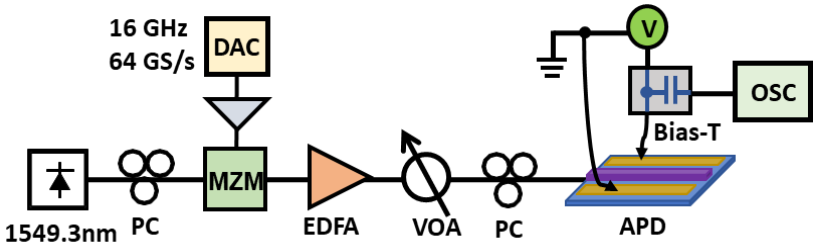

Figure 4.23 PAM4 signal detection setup.

The frequency roll-off response of the transmitter (including DAC, modulator driver and modulator) as well as nonlinear distortions intrinsic to the MZM and driver are measured using a reference 40-GHz photodetector (Discovery Semiconductor DSC-10H), and subsequently pre-compensated for with a 7-tap equalization filter in the digitized samples uploaded to the DAC.

The PAM4 eye diagrams are measured with -3 dBm optical power coupled to the APD device under test, which corresponds to -9.2 dBm optical modulation amplitude (OMA). The OMA parameter is defined as the power difference between the high level (P3 in Figure 4.22) and the low level (P0 in Figure 4.22) as $OMA_{outer} = P3 - P0$.

Figure 4.24 show the received electrical eye diagrams at 32 Gbaud (64 Gbs) with reverse bias voltages of -3 V, -10V, -11 V, and -12 V, which correspond to effective radio-frequency gain of M = 1, 1.6, 2.2, and 2.6 at the -3 dBm input power level, respectively. The recorded eye diagrams are absent of eye level distortion and inter-symbol interference (ISI), suggesting that the APD response remains linear over the bandwidth of the channel (~ 26 GHz).

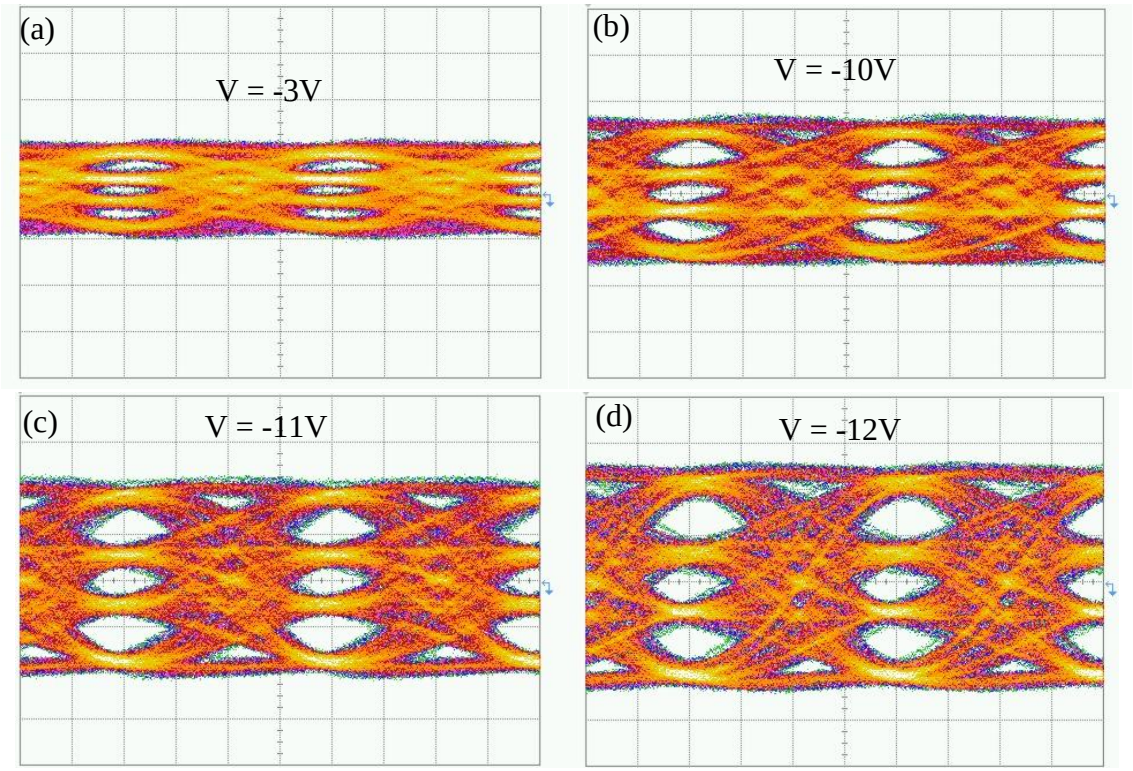

Figure 4.24 Eye diagrams for 32 Gbaud (64 Gbs) PAM4 signal detection experiments at various reverse bias voltages: (a) -3 V; (b) -10 V; (c) -11 V; (d) -12 V.

Figure 4.25 plots the Q-factor and BER results of the received signals as a function of reverse bias voltages at the -3 dBm input power level. The Q-factor is a measure of how noisy a pulse is and provides a qualitative description of the receiver performance, which is defined as the difference of the mean values of the two signal levels divided by the sum of the noise standard deviations at the two signal levels (Eq. 4-18 for PAM4 signals). For

PAM4 signals, the Q-factor can be calculated using Eq. 4-18, where μ_i and σ_i (i = 0, 1, 2, 3) are the mean values and standard deviations of the i level. BER is a measure of the number of bit errors that occur in a given number of bit transmissions.

$$Q = \min\left\{\frac{\mu_1 - \mu_0}{\sigma_1 - \sigma_0}, \frac{\mu_2 - \mu_1}{\sigma_2 - \sigma_1}, \frac{\mu_3 - \mu_2}{\sigma_3 - \sigma_2}\right\} \quad 4\text{-}18$$

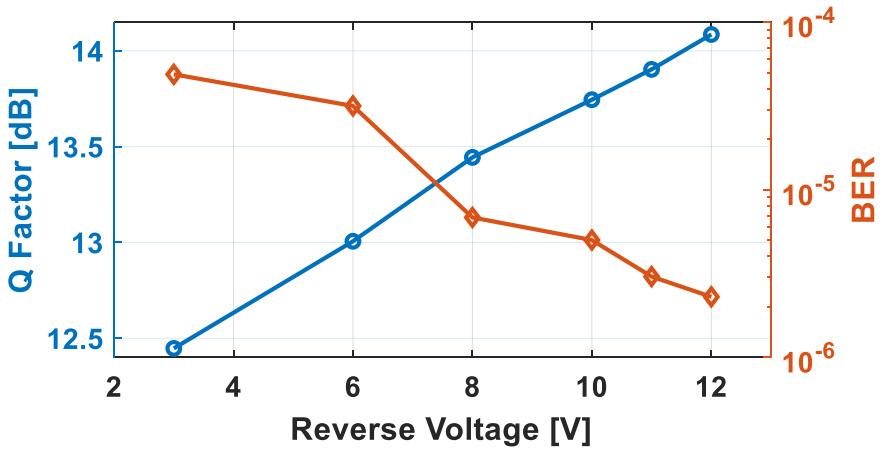

Figure 4.25 Q factor and BER results for 32 Gbaud (64 Gbs) PAM4 signal detection as a function of reverse bias voltages.

As illustrated by Figure 4.25, the multiplication gain of APD provides a 1.7 dB increase in Q-factor over the thermal-noise limited value at M = 1, which indicates the receiver sensitivity improvement with multiplication gain provided by the APD. As we do not apply TIA circuit after detection, the determination of sensitivity is limited by the vertical resolution of the oscilloscope (DCA).

The APD performances for PAM4 signal detection applications are further modeled in the transceiver circuit schematic shown in Figure 4.26 using Lumerical INTERCONNECT. A PAM4 pulse generator fed by a pseudorandom bit sequence (PRBS) generator is used to modulate a CW laser with an MZM. The signal is then fed to a pin photodetector, of which the detected output signal is exported to MATLAB to further

account for the gain nonlinearity of APDs under different input power levels as demonstrated in the 4.3.1 characterization section (Figure 4.26 (a)). After that, the gain-adjusted current signal is imported back to another simulation circuit for APD detection modeling (Figure 4.26 (b)). The APD bandwidth responses under different bias voltages (Figure 4.26 (c)) are taken into effects via the S-matrix object (SPAR_1) with imported data to the simulation circuit. An eye diagram component (EYE) is added to record the detected eye diagrams.

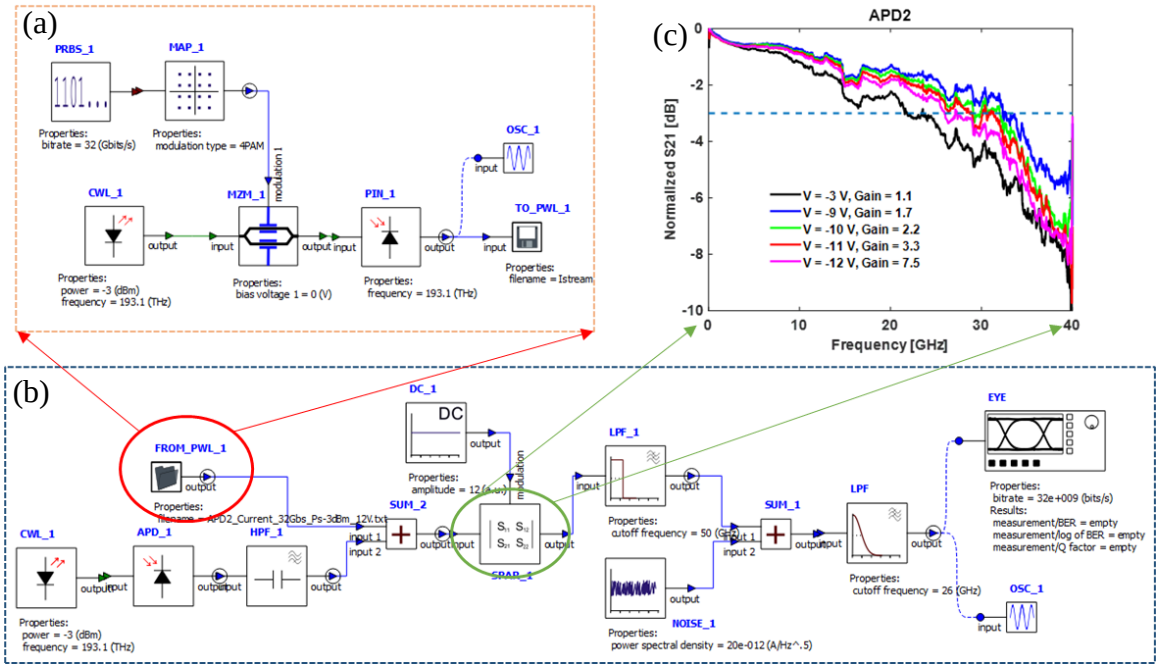

Figure 4.26 Schematic representation of PAM4 signal detection simulation setup in Lumerical INTERCONNECT.

The detection circuit modeling is implemented under identical settings as the experimental conditions, with the gain, excess noise, and bandwidth responses of the APD imported to the circuit using experimentally characterized data. The detected eye diagrams with 32-Gbaud PAM4 data under various bias voltages (-3 V, -10V, -11 V, and -12 V) for APD2 are shown in Figure 4.27 using the same vertical scale, which demonstrate a great consistency with the experiment results shown in Figure 4.24.

To summarize, this section demonstrates the fabricated APD in PAM4 channel reception test. Eye test results indicate that the APD remains linear for 32 Gbaud PAM4 signaling. The 1.7 dB increase in Q-factor with multiplication gain indicates that the APD device is capable of improving the receiver sensitivity.

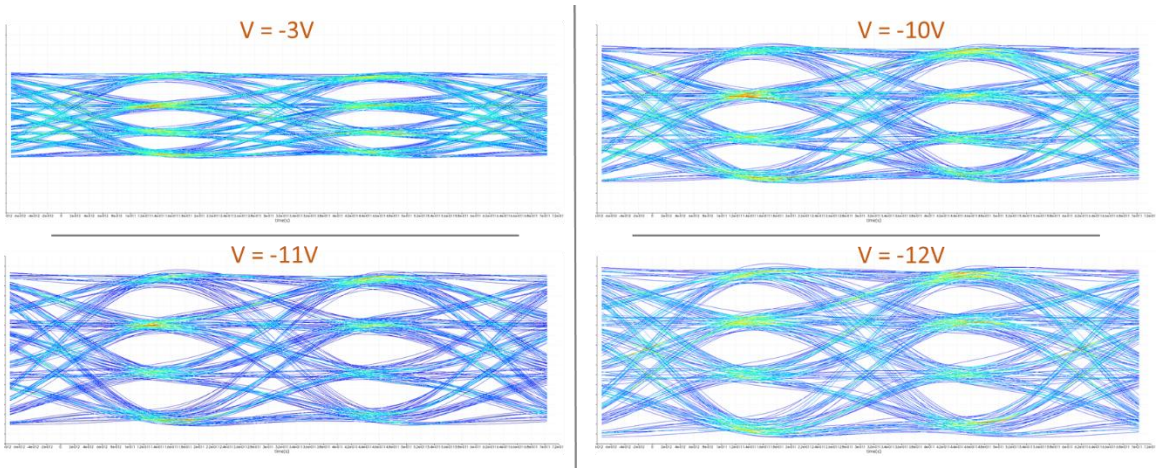

Figure 4.27 Circuit-simulated eye diagrams for 32 Gbaud (64 Gbs) PAM4 signal at various reverse bias voltages of -3 V, -10 V, -11 V, and -12 V, respectively.

4.5 APD Coherent Detection Experiment

Coherent detection with polarization multiplexing, as symbol decisions are made using both the in-phase (I) and quadrature (Q) signals in the two field polarizations, allows information to be encoded in all the available degrees of freedom [85], [86]. Therefore, it further enhances the spectral efficiency than intensity-modulation-direct-detection (IMDD) systems at the same SNR (comparisons summarized in Table 4.3), which provides a scalable path towards Tb/s/wavelength capacity. Moreover, the advancement of digital signal processing (DSP) allows signals to be filtered, delayed, split, and amplified digitally without quality degradation and enables compensation of transmission impairments such chromatic dispersion (CD) and polarization mode dispersion (PMD). Advanced forward

error-correction (FEC) coding may also be implemented to further decrease the bit error ratio (BER).

Considering all these advantages, in this section we study the advancement of APD coherent receiver and present the experimental implementation of our APDs for coherent detection.

Table 4.3 Comparison between coherent detection and IM-DD schemes

	Coherent	IM-DD
Modulation parameter	Amplitude & phase	Intensity
Detection method	Heterodyne or homodyne detection	Direct detection
Carrier phase sensitivity	Yes	No
Polarization sensitivity	Yes	No

Coherent receiver, inside which the signal is interfered with a local oscillator (LO) to extract the complex amplitude (amplitude and phase) information of the signal, usually constitutes of a 90°-hybrid and four photodetectors with each two of them connected in a back-to-back fashion, as illustrated in Figure 4.28. The balanced detection with back-to-back connection is introduced to suppress the DC component and double the beat between the signal and the LO.

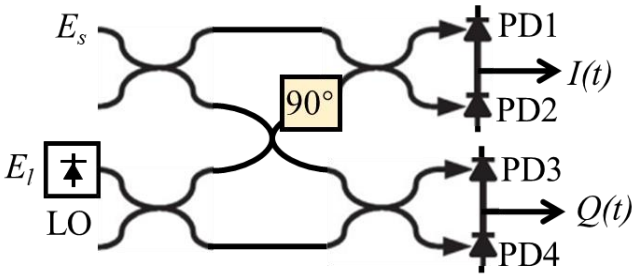

Figure 4.28 Configuration of a coherent receiver.

When the input signal and the LO are co-polarized, the electric fields incident on PD1 and PD2 (Figure 4.28) are given by:

$$E_1 = \frac{1}{\sqrt{2}}(E_s + E_l) \tag{4-19}$$

$$E_2 = \frac{1}{\sqrt{2}}(E_s - E_l) \tag{4-20}$$

where E_s and E_l are the complex electric fields of the signal and LO respectively. E_i $(i = 1, 2, 3, 4)$ is the interferometric electric field coupled to PD_i $(i = 1, 2, 3, 4)$ as illustrated in Figure 4.28. The corresponding output photocurrents are:

$$I_1(t) = \frac{R}{2}\left\{P_s(t) + P_l + 2\sqrt{P_s(t)P_l}\cos\left[\omega_{IF}t + \theta_{sig}(t) - \theta_l(t)\right]\right\} \tag{4-21}$$

$$I_2(t) = \frac{R}{2}\left\{P_s(t) + P_l - 2\sqrt{P_s(t)P_l}\cos\left[\omega_{IF}t + \theta_{sig}(t) - \theta_l(t)\right]\right\} \tag{4-22}$$

Here I_i $(i = 1, 2, 3, 4)$ is the output photocurrent of PD_i $(i = 1, 2, 3, 4)$, R is the responsivity of the photodiode, P_s and P_l are the signal and LO power, $\omega_{IF} = |\omega_s - \omega_l|$ is the intermediate frequency (IF), and θ_{sig} and θ_l are the phase of the transmitted signal and LO respectively.

With the back-to-back balanced detection, the final in-phase output $I(t)$ can be expressed as:

$$I(t) = I_1(t) - I_2(t) = 2R\sqrt{P_s(t)P_l}\cos\left[\omega_{IF}t + \theta_{sig}(t) - \theta_l(t)\right] \tag{4-23}$$

The quadrature output $Q(t)$ for the component follows the same deduction procedure:

$$Q(t) = I_3(t) - I_4(t) = 2R\sqrt{P_s(t)P_l}\sin\left[\omega_{IF}t + \theta_{sig}(t) - \theta_l(t)\right] \tag{4-24}$$

Eq. 4-23 and Eq. 4-24 indicate that the balance-detected output photocurrent is proportional to $\sqrt{P_l}$, meaning that an increase in the LO power effectively provides a gain for the signal photocurrent. It has been found that quantum-noise-limited receiver

sensitivity (also called shot-noise-limited receiver sensitivity) could be accomplished by injecting a sufficiently high LO power into the coherent receiver to combat the circuit noise of the receiver.

This high-power demand on the LO, however, increases the overall power consumption of the coherent detection system and poses challenges in short-reach power-hungry optical interconnects. Leveraging internal gain provided by APDs, coherent receivers built with APDs can improve the sensitivity with a lower optical power or electrical gain than traditional coherent receivers [87], thereby reducing power consumption of such systems.

A coherent receiver built with APDs, with considerations of the internal gain provided by the APDs and various noise sources as stated earlier, results in an ultimate output photocurrent expressed by:

$$I(t) = 2MR\sqrt{P_s(t)P_l}\cos\left[\omega_{IF}t + \theta_{sig}(t) - \theta_l(t)\right] + i_{RIN} + i_{shot} + i_{thermal} \qquad 4\text{-}25$$

where i_{RIN} denotes the response photocurrent of the beating between the LO and the relative intensity noise (RIN) of the LO, i_{shot} represents the shot noise current generated from the coherent receiver, $i_{thermal}$ is the thermal noise current. Shot noise and thermal noise are two fundamental noise mechanisms in an optical receiver. The thermal noise of the coherent receiver can be expressed as [87], [88]:

$$\sigma_{thermal}^2 = (i_T)^2 \Delta f \qquad 4\text{-}26$$

where i_T is the equivalent thermal noise current density in the coherent receiver, including the thermal noise introduced by the following circuitry and the thermal noise introduced by the photodiode. Δf is the effective noise bandwidth of the receiver.

The shot noise of a coherent receiver built with APDs is represented by: [87], [88]

$$\begin{aligned}\sigma_{shot}^2 &= 2q\left(I_{ds} + FM^2(I_i + I_{db})\right)\Delta f \\ &= 2qFM^2\left(R_0P + I_d\right)\Delta f\end{aligned} \tag{4-27}$$

Here q is the fundamental electronic charge, I_{ds} and I_{db} are the surface and bulk dark current of the APD, I_i is the photocurrent at unit gain, F and M are the excess noise factor and multiplication gain of the APD. In the second row, R_0 represents the primary responsivity at unit gain, P is the total power coupled to the APD, and the surface and bulk dark current are gain normalized to I_d.

The RIN noise is expressed as: [87], [88]

$$\begin{aligned}\sigma_{RIN}^2 &= 4M^2R_0^2(E_l \cdot E_{l-RIN})^2 \\ &= 4M^2R_0^2P^2(RIN \cdot 2\Delta f)\end{aligned} \tag{4-28}$$

where E_{l-RIN} is the electrical field of the RIN from the LO, *RIN* is defined as the double-sided spectral density of the RIN from LO, expressed in dB/Hz.

Therefore, the overall SNR of the coherent receiver output can be summarized as [87], [88]:

$$\begin{aligned}SNR &= \frac{2M^2R_0^2P_sP_l}{\sigma_{thermal}^2 + \sigma_{shot}^2 + \sigma_{RIN}^2} \\ &= \frac{2M^2R_0^2P_sP_l}{(i_T)^2\Delta f + 2qFM^2\left(R_0P + I_d\right)\Delta f + 4M^2R_0^2P^2(RIN \cdot 2\Delta f)}\end{aligned} \tag{4-29}$$

Numerical simulations are carried out for analyzing the impacts of gain M on the received SNR in Eq. 4-29. We use parameters that correspond to our APD characterization results in Section 4.3, which are listed in Table 4.4 below.

Table 4.4 Parameters adopted for SNR calculations

Parameters	Values
Effective ionization ratio k_{eff}	0.5
Thermal noise current i_T	18 $pA/\sqrt{Hz}$
Effective noise bandwidth Δf	20 GHz
Primary responsivity R_0	0.9 A/W
RIN	-145 dB/Hz

We adopt an effective ionization ratio k_{eff} of 0.5, and the corresponding excess noise factor F is calculated with reference to Eq. 4-8. The numerical simulation results of the receiver SNR as a function of APD gain M with various LO power is plotted in Figure 4.29. Compared with the no-gain cases with $M = 1$, the SNR is improved with gain provided by APD. In cases where the LO power is high, SNR can show a downward trend with further increasing the gain, caused by the excess multiplication noise added to the system. Moreover, the gain provided by APD effectively lowers the demand on LO power. While a LO power of 0 dBm is required to achieve a SNR of 34 dB, the required LO power to achieve the same SNR drops to -10 dBm with a gain of 5. This 10 times decrease in the required LO power increases the power budget margin of the system and potentially lowers the overall power consumption.

The performance of the fabricated APD in coherent channel detection is characterized using APDs integrated with silicon optical hybrid based on 4×4 MMI coupler, as shown by the SEM image of the coherent detector chip in Figure 4.30. Each of the four output ports of the 4×4 MMI coupler is connected with an APD for signal detection. We

do not have direct back-to-back connections on chip. The subtraction between the constructive and destructive interferences is conducted digitally after detection.

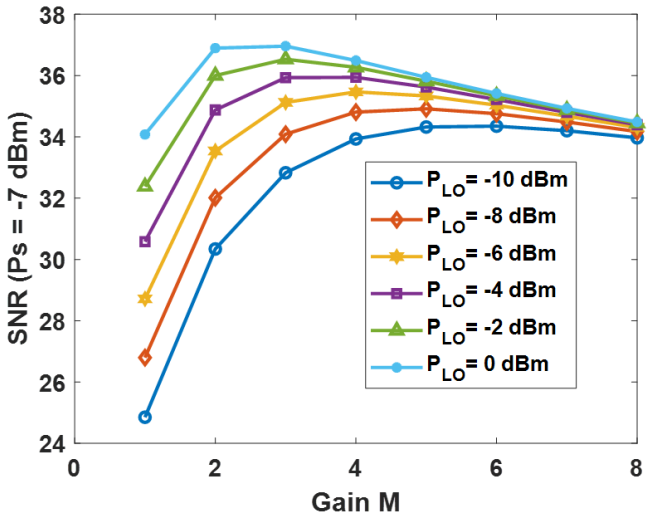

Figure 4.29 Numerical simulation of the receiver SNR as a function of APD gain with various LO power. Parameters used for calculation: k_{eff} = 0.5, *Ps* = -10 dBm, i_T = 20 pA/ √ Hz, $\triangle f$ = 20 GHz, *R* = 0.9 A/W, *RIN* = -145 dB/Hz.

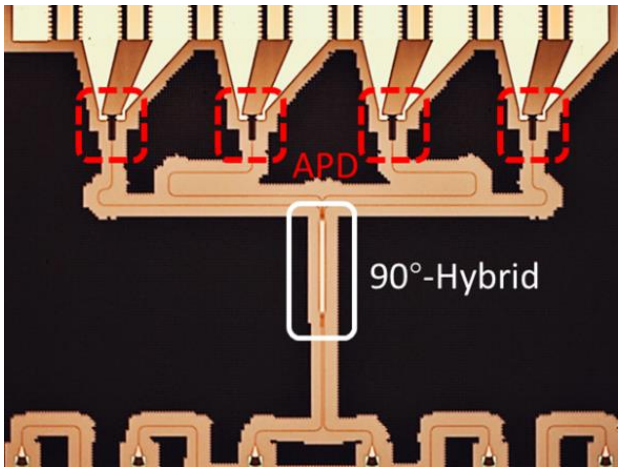

Figure 4.30 SEM picture of the on-chip coherent receiver consisting of an MMI-based 90°-hybrid and 4 APD devices.

The optical hybrid realized by 4×4 MMI coupler provides advantages in design simplicity, device compactness, and performance reliability. The optical phases of the signals in a 4×4 MMI coupler are given by: [34], [35]

$$\varphi_{ij} = \frac{\pi}{16}(j-i)(8+i-j)+\pi \qquad \text{for } i+j \text{ even} \qquad \text{4-30}$$

and

$$\varphi_{ij} = \frac{\pi}{16}(i+j-1)(9-i-j) \qquad \text{for } i+j \text{ odd} \qquad \text{4-31}$$

where i = 1, 2, 3, 4 is the bottom-up numbering of the 4×4 MMI coupler input waveguides and j = 1, 2, 3, 4 is the top-down numbering of the output waveguides (illustrated in Figure 4.31).

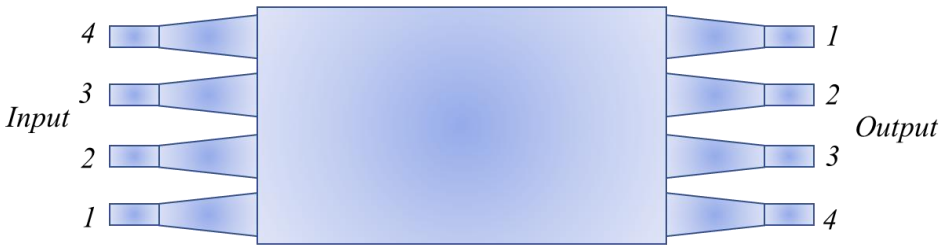

Figure 4.31 Schematic view of a 4×4 MMI coupler.

The calculated phase relations between the four ports of the 4×4 MMI coupler are summarized in Table 4.5, clearly showing the 90° phase relations between ports.

Table 4.5 Phase relations of the general 4×4 MMI coupler

4×4 MMI	j = 1	j = 2	j = 3	j = 4
i = 1	π	$\frac{3}{4}\pi$	$\frac{7}{4}\pi$	π
i = 2	$\frac{3}{4}\pi$	π	π	$\frac{3}{4}\pi$
i = 3	$-\frac{1}{4}\pi$	π	π	$\frac{3}{4}\pi$
i = 4	π	$-\frac{1}{4}\pi$	$\frac{3}{4}\pi$	π

For example, if we introduce the signal at the input port i = 1 and a coherent LO at input port i = 3 with a phase retardation of $\frac{1}{4}\pi$ between each other, then they would interfere constructively in the output j = 4 and destructively in the output port j = 1. Subtraction between the output at ports j = 1 and 4 could get the balance-detected in-phase signal in Eq. 4-23. Similarly, subtraction between the output at ports j = 2 and 3 could get the quadrature signal.

Figure 4.32 illustrates the setup for coherent detection with APDs. The test channel is created from an external cavity laser at 1549.3 nm wavelength with 5 kHz linewidth. A 16-QAM modulation signal at variable baud-rate is imprinted onto the carrier using a nested-MZM with > 30 GHz bandwidth, driven by quad-channel DAC with 64 GS/s sampling rate. The data pattern is shaped by a raised-cosine filter with a roll-off factor of 0.1 to decrease inter-symbol interference (ISI). To allow control of channel optical signal-to-noise ratio (OSNR), a filtered amplified spontaneous emission (ASE) noise source with variable output power is coupled with the 16-QAM channel before entering the receiver, and the OSNR is monitored prior to the device under test. The channel is further filtered to 0.6 nm bandwidth and amplified before being coupled to the signal port of the APD-integrated coherent receiver. The LO is derived from the same laser source powering the test channel via a 50/50 coupler, and subsequently amplified to compensate for fiber-to-chip coupling loss. The photocurrents from the four APDs of the integrated coherent receiver are coupled to the input ports of the real-time oscilloscope (Tektronix DPO72004A), which simultaneously captures the photocurrent from the four channels (via the internal 50Ω load) at 50 GS/s.

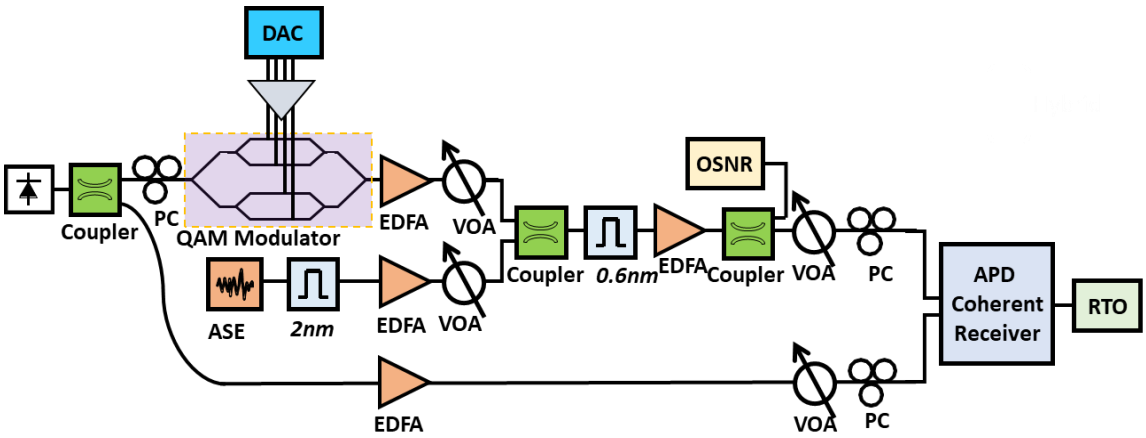

Figure 4.32 Setup for coherent detection.

Pre-compensation of the data pattern is further applied in order to remove the frequency response and nonlinear distortion of the transmitter (nested Mach Zehnder modulator + modulator driver + digital analog converter) and the real-time oscilloscope (RTO) serving as the digitizer. The frequency response and nonlinear distortion of the transmitter and RTO are characterized using a 40-GHz-bandwidth reference coherent receiver constructed out of discrete InP photodetectors (Finisar BPDV2120R) and 90°-optical hybrid. The resulted equalization filter was applied back to the data uploaded to the DAC. As a comparison, Figure 4.33 shows the captured spectra from the optical spectrum analyzer (OSA) before and after frequency roll-off and nonlinear distortion equalization for 32 Gbaud 16QAM modulation, indicating the compensation of the frequency response and nonlinear distortion of the transmitter and digitizer with the least-mean-square (LMS) equalization.

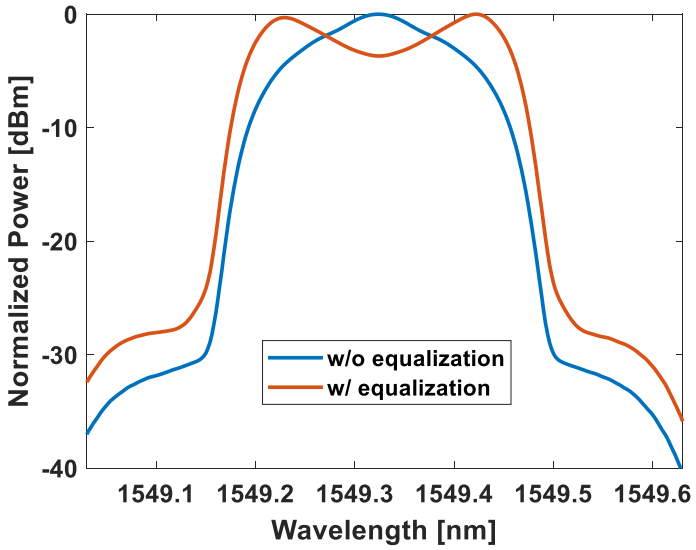

Figure 4.33 Monitored OSA spectra w/ and w/o frequency roll-off equalization.

After the signals from the four individual APDs are grabbed and digitized by the RTO, timing skew between the four ADC channels and carrier phase recovery of the four channels are performed offline in MATLAB to recover the transmitted data. Subsequent characterizations shown in the following text of this section are performed at an averaged signal / LO power of -9 dBm / -7 dBm respectively into each APD, of which the fiber-to-chip coupling loss of 7 dB during experiment and hybrid excess loss of 1 dB are taken into account.

Figure 4.34 depict the constellation diagrams for 40 Gbaud 16-QAM signal detection results under OSNR (@ 0.1 nm) values of 14.2 dB and 19.3 dB and bias voltages of -3V and -11V respectively, clearly illustrating the performance improvement with the APD multiplication gain. There exist very little distortions in the received constellation diagrams, proving that the APD is capable of receiving 40 Gbaud 16-QAM signal without distortion.

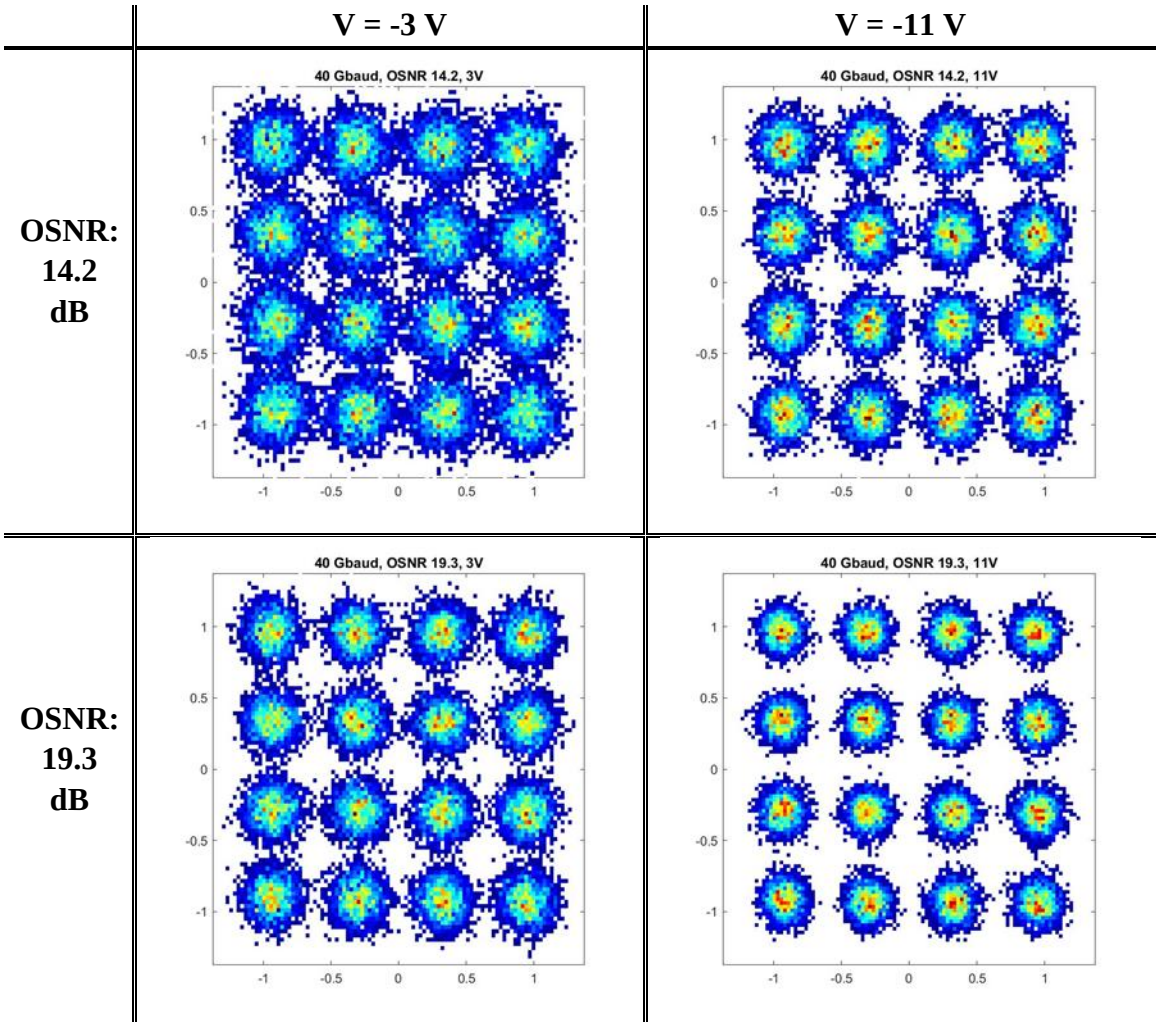

Figure 4.34 Constellation diagrams for 40 Gbaud 16-QAM signal detection results with various OSNR values and bias voltage.

Figure 4.35 demonstrates the sensitivity of the APD-integrated coherent receiver in terms of Q^2 versus OSNR at 0.1 nm for a 40 Gbaud 16-QAM channel when biased at -3V and -11V. The internal gain of the APDs provides a 2-dB improvement in Q-factor over the thermal-noise limited receiver at M = 1, reaching BER = 4.5×10^{-3} (Q^2 = 8.8 dB) at 14.5 dB OSNR which corresponds to error-free reception with the staircase hard decision forward error-correction (HDFEC) coding [89]. Near-theoretic sensitivity and distortion-

free constellation further suggest that no discernible nonlinear distortion (compression and bandwidth modulation due to output current) was present in this coherent receiver.

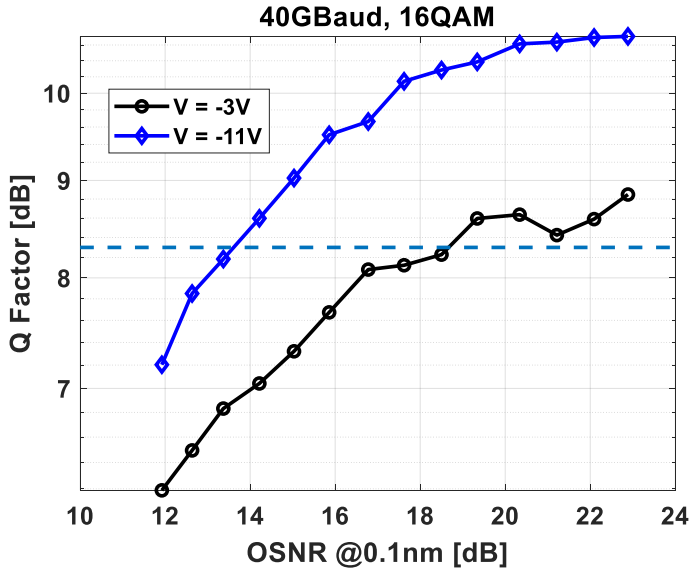

Figure 4.35 Q factor results for 40 Gbaud 16-QAM signal detection as a function of OSNR values under various bias voltage.

To summarize, this section demonstrates the APD coherent receiver implementation, showing 2 dB Q-factor improvement for 40 Gbaud 16 QAM channel reception with the multiplication gain provided by the APD.

4.6 Summary

In this chapter we have demonstrated the design, characterization, and experiment of an APD device using foundry-compatible fabrications.

After reviewing the background physics for carrier impact ionization, the design of the APD device using foundry-provided services are presented with detailed parameter study. The fabricated devices are characterized in DC dark/photo/gain response, small signal S-parameter response, and noise characteristics. Further link detection experiments of the APD devices are demonstrated with 32 Gbaud PAM4 and 40 Gbaud 16QAM data, showing performance improvements with the gain provided by APDs.

Chapter 4, in part, is a reprint of the material as it appears in 2020 Conference on Lasers and Electro-Optics (CLEO), pp. 1-2. IEEE, 2020, titled “High-Speed Low-Voltage Waveguide-Integrated Ge-on-Si Avalanche Photodiodes”, by Jin Zhang, Ana Pejkic, Bill Ping-Piu Kuo, and Stojan Radic. Chapter 4 also contains in part materials accepted for publication as it may appear in the IEEE/OSA Optics Express, titled “64Gbs PAM4 and 160Gbs 16QAM Reception Using Low-Voltage Si-Ge Waveguide-Integrated APD”, by Jin Zhang, Bill P.-P. Kuo, and Stojan Radic. The dissertation author was the primary investigator, and the primary author of these articles.

Chapter 5 Multi-stage Silicon Nonlinear Mixer

5.1 Introduction

The exponential growth of the Internet traffic demands capacity scaling not only in optical communication channel, but, likewise, in networking nodes responsible for traffic routing. Wavelength multicasting, which can transmit original data to multiple destinations via different optical carrier wavelengths simultaneously, is recognized as a fundamental network functionality for synchronous traffic redistribution to multiple nodes through datagram duplication, thereby relieving network capacity demand for applications such as video broadcast and map-reduce type distributed computation [90]. While multicast is conventionally executed in the network layer, its physical layer realization poses an intriguing proposition for further capacity and power savings, particularly in optical networks, since it allows decoupling of the high-rate optical channels from the high latency and power consuming electronic processors.

Physical multicasting requires the device to provide scalable number of signal replicas, to be agnostic to the incoming channel format, and ideally to incur miniscule latency overhead to the traffic. Direct optical multicasting has been demonstrated on a multitude of platforms, with examples including four-photon mixing (FPM) in highly nonlinear fibers (HNLF) [91], cross-channel effects in semiconductor optical amplifiers (SOAs) [92], and more recently photon mixing in silicon waveguides [93]. Among these, the silicon photonic waveguide approach is of particular interest since it offers low optical latency, high theoretical efficiency, and a viable path towards monolithic integration with CMOS processing logic. Demonstrations to date are, however, either incompatible with coherent modulation formats and requires massive integration of laser sources [93], or

impaired by two-photon absorption (TPA) mediated nonlinear loss at high power which limited the number of copies [94].

Therefore, in this chapter, we propose a novel concept for scalable wavelength multicasting based on multi-stage, loss- and dispersion-managed silicon waveguide mixer. The proof-of-concept demonstration in a dual-stage mixer allowed for a successful 9-fold multicasting of a 24 GBaud, 16-Quadrature Amplitude Modulated (QAM) channel using two pumps.

5.2 Silicon Nonlinear Properties

Silicon exhibits a significant third-order nonlinearity, with a Kerr coefficient more than 100 times larger [95] than that of silica glass in the telecommunication band. This feature, together with the tight mode confinement provided by SOI waveguides, make it possible to realize a variety of optical nonlinear functions in silicon waveguides at relatively low power levels through CMOS-compatible technology. Nonlinear optical phenomena such as Raman amplification and lasing, wavelength conversion, and self-phase modulation (SPM) and cross-phase modulation (XPM), have all been demonstrated in SOI waveguides.

As a semiconductor material, Si is of a crystal structure with inversion symmetry. Therefore, the lowest-order nonlinear effects in Si stem from the third-order susceptibility $\chi^{(3)}$, of which the real part is related to the Kerr coefficient n_2 and the imaginary part is related to the two-photon absorption coefficient β_{TPA}, respectively, as:

$$\frac{\omega}{c} n_2(\omega) + \frac{i}{2} \beta_{TPA}(\omega) = \frac{3\omega}{4\varepsilon_0 c^2 n_0^2(\omega)} \chi^e_{1111}(-\omega; \omega, -\omega, \omega) \qquad 5\text{-}1$$

where ω is the angular frequency, c is the vacuum speed of light, ε_0 is the vacuum permittivity, $n_0(\omega)$ is the linear refractive index of silicon at the frequency ω, and χ^e_{1111}

is the degenerate electronic contribution of the third-order susceptibility. The electronic contribution χ^{e}_{1111} stems from oscillations of bound electrons, leading to the optical Kerr effect through intensity-dependent changes in the refractive index. It also leads to TPA effects whenever the energy of photons exceeds the half band gap $E_g\ /\ 2$, where $E_g \approx 1.12\ eV$ for silicon (corresponds to a wavelength of 1.1 μm). Bound electrons in the valence band can be excited to the conduction band through TPA by absorbing two photons with total energy exceeding E_g, resulting in nonlinear absorption loss undesirable for most applications. The TPA process in silicon has to be assisted by phonons to conserve momentum because of the indirect nature of its band gap.

Extensive measurements exist to characterize n_2 and β_{TPA} of silicon semiconductor [95], [96]. The value of n_2 for silicon is found to be more than 100 times larger in the 1.55-μm band than that of silica [95], [96]. However, TPA is also quite large in this spectral region, which is the main drawback for silicon to realize nonlinear functionalities at telecom wavelength, not only because of the extra loss in the process but also because the generated carriers subsequently produce usually undesired free carrier absorption (FCA) and free carrier dispersion (FCD). The relative magnitudes of the Kerr and TPA coefficients are often characterized by a nonlinear figure of merit (NFOM) in silicon defined as $F_n\ = n_2\ /(\lambda \cdot \beta_{TPA})$, where λ is the optical wavelength in vacuum. This NFOM increases with longer wavelengths, mainly due to the decrease of β_{TPA} at longer wavelengths [96]. For wavelengths between 1.2 and 1.7 μm, NFOM has a relatively low value of around 0.2 – 0.4. Therefore, special efforts such as using a reverse-mode p-i-n junction to sweep out the generated free carriers need to be taken to reduce FCA and FCD effects for applications in the communication band.

The nonlinear interactions of optical waves inside silica fibers are well understood and accurately modeled with the so-called generalized nonlinear Schrödinger equation (NLSE) [97]. To model the nonlinear effects in silicon waveguides, a similar theoretical formalism with suitable modifications in account of the unique features can be used.

We start by considering the temporal dynamics, which are modeled by the nonlinear Schrödinger equation under the slowly varying envelope approximation. The approximation simplifies the equation for dispersive wave-packet propagation from being second-order in z to first-order in z, where z is the propagation coordinate. The generalized nonlinear Schrödinger equation is expressed as [97]:

$$\frac{\partial A}{\partial z}+\frac{\alpha}{2}A+\sum_{m=0}^{\infty}\frac{i^{m+1}\beta_{im}}{m!}\frac{\partial^m A_i}{\partial t^m}=i\gamma\left(|A|^2\,A+\frac{i}{\omega_0}\frac{\partial}{\partial T}(|A|^2\,A)-T_R A\frac{\partial|A|^2}{\partial T}\right) \qquad 5\text{-}2$$

where A describes the slowly varying pulse envelope, α is the loss coefficient, β_{im} is the mth-order dispersion parameter defined as $\beta_{im}=\frac{\partial^m}{\partial\omega^m}\beta_i$, γ is the nonlinear parameter defined as $\gamma(\omega_0)=\frac{n_2(\omega_0)\omega_0}{cA_{eff}}$, and T_R is the first moment of the nonlinear response function. Here T is a frame of reference moving with the pulse group velocity v_g in a way as $T=t-z/v_g=t-\beta_1 z$.

For silicon waveguide, it should be included for the loss term both the waveguide linear loss and its dispersion and nonlinear loss induced by free carriers. Assuming that free carriers are generated only optically so that $\overline{N_e}=\overline{N_h}=\bar{N}$, we can write α as a function of $\bar{N}$ and ω_0 as $\alpha(\omega_0,\bar{N})$. Here $\overline{N_e}$ and $\overline{N_h}$ represent the generated free electrons and free holes separately.

For pulses of relative wide width, the last two terms in Eq. 5-2 can be neglected, so is the contribution from the third- and higher-order dispersion terms. Under this condition, we can get the simplified Schrödinger equation as [97]:

$$i\frac{\partial A}{\partial z}+\frac{i\alpha}{2}A-\frac{\beta_2}{2}\frac{\partial^2 A}{\partial t^2}+\gamma\,|A|^2\,A=0 \qquad 5\text{-}3$$

The nonlinear Schrödinger equation in Eq. 5-2 or Eq. 5-3 is solved via numerical approaches as it generally does not have analytic solutions. The method that has been used most extensively to solve the pulse-propagation problem in nonlinear dispersive media is the split-step Fourier method [98], which is also the method we apply for our modeling in the following sections.

The nonlinear Schrödinger equation (Eq. 5-2 or Eq. 5-3) can be split into two parts as denoted by [97]:

$$\frac{\partial A}{\partial z}=\left(\hat{D}+\hat{N}\right)A \qquad 5\text{-}4$$

with $\hat{D}$ the differential operator accounting for the dispersion and losses within a linear medium and $\hat{N}$ a nonlinear operator governing the nonlinear effects. In general, the linear and nonlinear effects act together along the propagation of optical pulses. The split-step Fourier method obtains an approximate solution by assuming that the dispersive and nonlinear effects can be assumed to act independently in propagating over a small distance *s*, which means in the first step only dispersion takes effects, and in the next step the nonlinearity acts alone, as mathematically expressed by

$$A(z+s,T)=\exp(s\hat{D})\exp(s\hat{N})A(z,T) \qquad 5\text{-}5$$

With the advancement of the finite-Fourier-transform (FFT) algorithm, the exponential operator $\exp(s\hat{D})$ is evaluated in the Fourier domain, making the evaluation of

Eq. 5-5 really fast. It is for this reason that the split-step Fourier method is the most common numerical methods for solving the nonlinear Schrödinger equation, as is also the method we applied for our numerical modeling in the following sections.

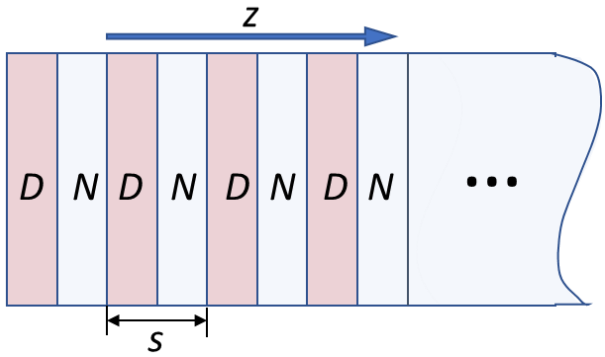

Figure 5.1 Illustration of the dispersion and nonlinearity distributions along the pulse propagation of the split-step Fourier method.

5.3 Silicon Mixer Waveguide Design and Multi-Stage Mixing Modeling

The silicon waveguide used as the parametric mixing platform is designed as a rib structure with 650-nm width and 250-nm etch depth on a SOI wafer with 300-nm device layer thickness (see Figure 5.2 (a)), fabricated in IME A*STAR. The p++ and n++ regions are apart from the waveguide core by 1.2 μm on both sides to prevent the optical field from overlapping with the lossy doped regions, resulting in low waveguide loss of 1.3 dB/cm. The waveguide geometry is chosen to place the zero dispersion wavelength at 1540 nm (Figure 5.2 (c)), thereby facilitating wide-band phase matching for efficient four-photon mixing with a low anomalous dispersion in C-band [97].

Besides dispersion tailoring, the waveguide cross-section is designed to maximize the figure of merit for the efficiency of nonlinear effects, defined by the product of nonlinear coefficient γ, pump power P_0 and effective length L_{eff}. The simulated mode field profile is shown in Figure 5.2 (b). With an effective mode area as small as 0.2 μm^2,

the nonlinear coefficient $\gamma = \frac{n_2(\omega_0)\omega_0}{cA_{eff}}$ is characterized to be 116 $W^{-1}m^{-1}$, which is 3-order of magnitude higher than that of silica fiber.

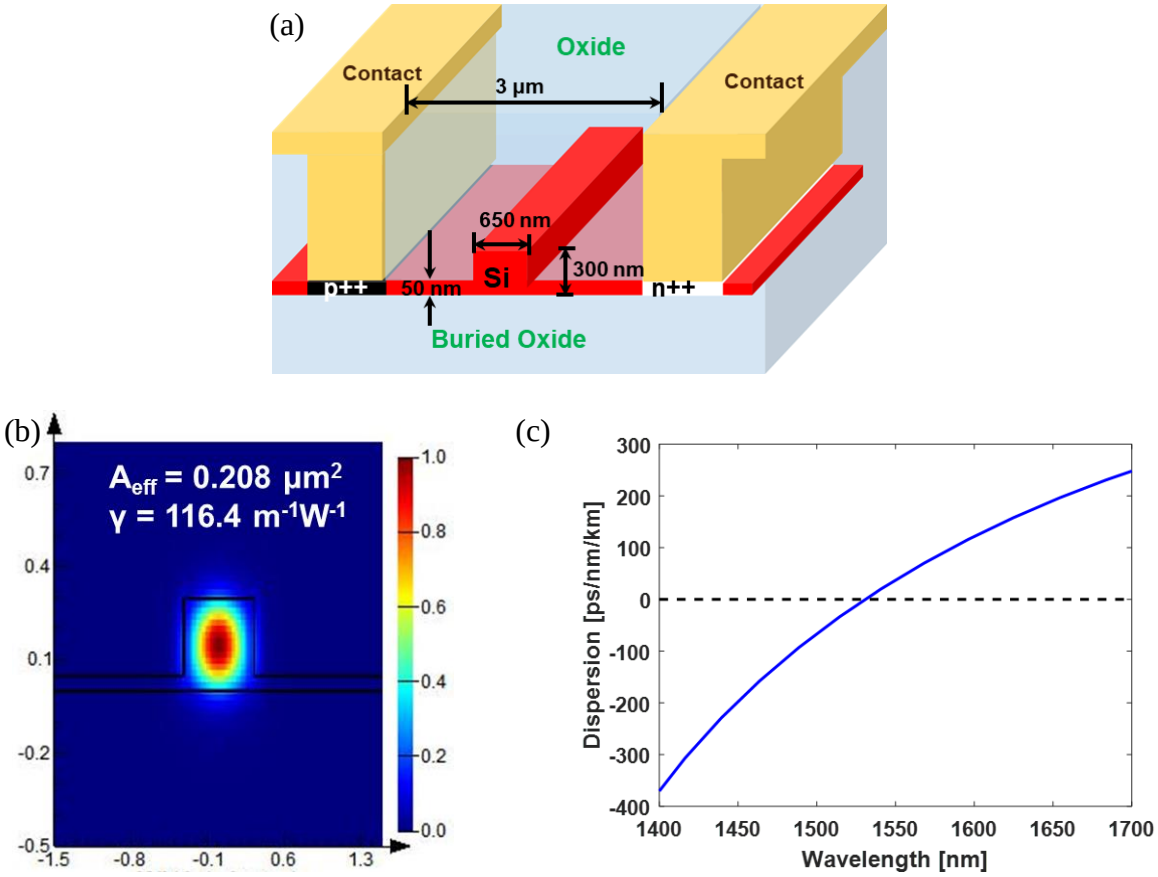

Figure 5.2 (a) Schematic view of the waveguide cross-section; (b) simulated mode profile; (c) the dispersion profile of the waveguide.

The effective length L_{eff} defines the length of the nonlinear interaction region, which is limited by the waveguide loss coefficient α as the optical power inside the waveguide is related to α as $P(z) = P_0 \exp(-\alpha z)$. In order to minimize the loss, a p-i-n structure is incorporated into the waveguide for active removal of free carriers generated by TPA [99]. On the other hand, however, the effective length and thus the mixing efficiency of a single waveguide mixer are ultimately bounded by the non-negligible attenuation of the waveguide. In silicon waveguides, propagation loss is mainly due to

scattering from the roughness at the core-cladding interfaces. In commonly used SOI wafers, waveguide sidewall roughness determined by the lithography and etching processes is typically on the order of a few nanometers. Scattering loss from the sidewall roughness thus constitutes the dominant cause of loss in silicon waveguides, resulting in a typical loss of sub-micron Si waveguides around 1-2 dB/cm.

To study the limitations posed by the attenuation-bounded effective length L_{eff}, we first simulate the nonlinear mixing results of a one-stage silicon waveguide mixer with various lengths. We implement the dual-pump-seeded parametric mixer as it has been identified as an efficient method for wavelength multicasting with sizable number of signal copies [100]. The pump wavelengths are set to be 1555.9 nm (P1) and 1559.1 nm (P2) with 50-mW (17 dBm) power each, and the signal wavelength is at 1557.0 nm (S) with a power of 0.5 mW (-3 dBm). The total input power is thus 20 dBm. The wavelength and power distributions of the input pumps and signal for the numerical modeling are shown in Figure 5.3 (a). As illustrated in Figure 5.3 (b), these three input waves interact via various nonlinear processes of phase conjugation (PC), modulation instability (MI), and Bragg scattering (BS) to generate new idlers [101]. In the meanwhile, high order pumps are further created through nonlinear processes like SPM in the waveguide, resulting in cascaded multicast generation of the input signal.

The numerically-calculated nonlinear mixing results with waveguide lengths of 3 cm, 5 cm, 7 cm, 9 cm, 11 cm, and 13 cm are shown in Figure 5.4, respectively. It can be seen that the mixing output spectrum changes little with the mere increase of waveguide length except for more loss and less output power, indicating the restriction on the effective length posed by the attenuation of the waveguide.

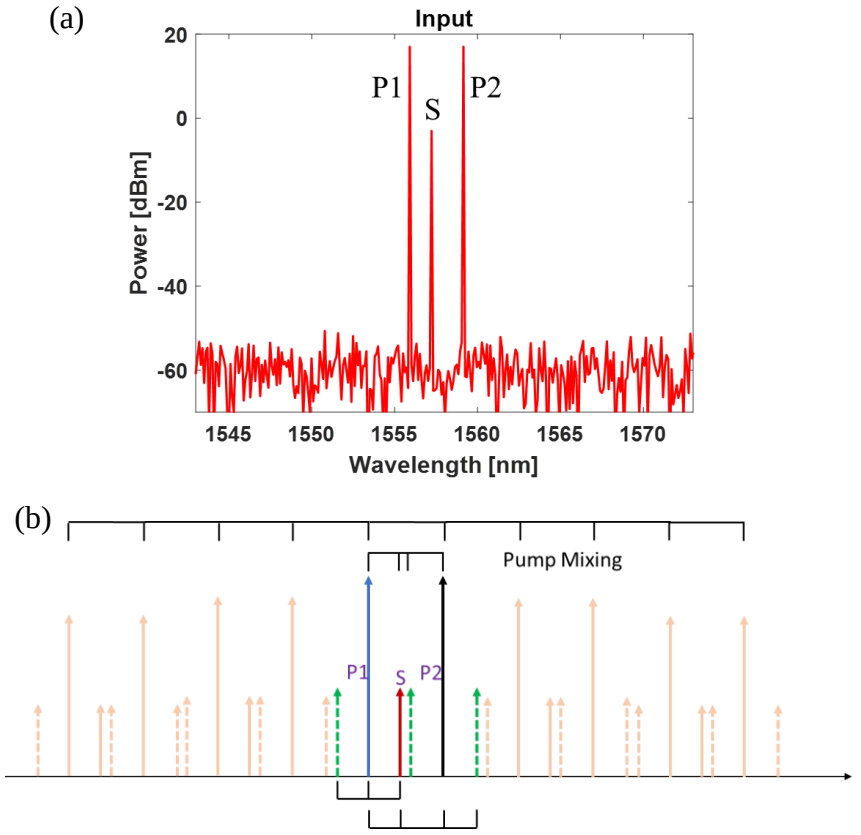

Figure 5.3 (a) Wavelength and power distributions for the numerical modeling; (b) nonlinear mixing principles.

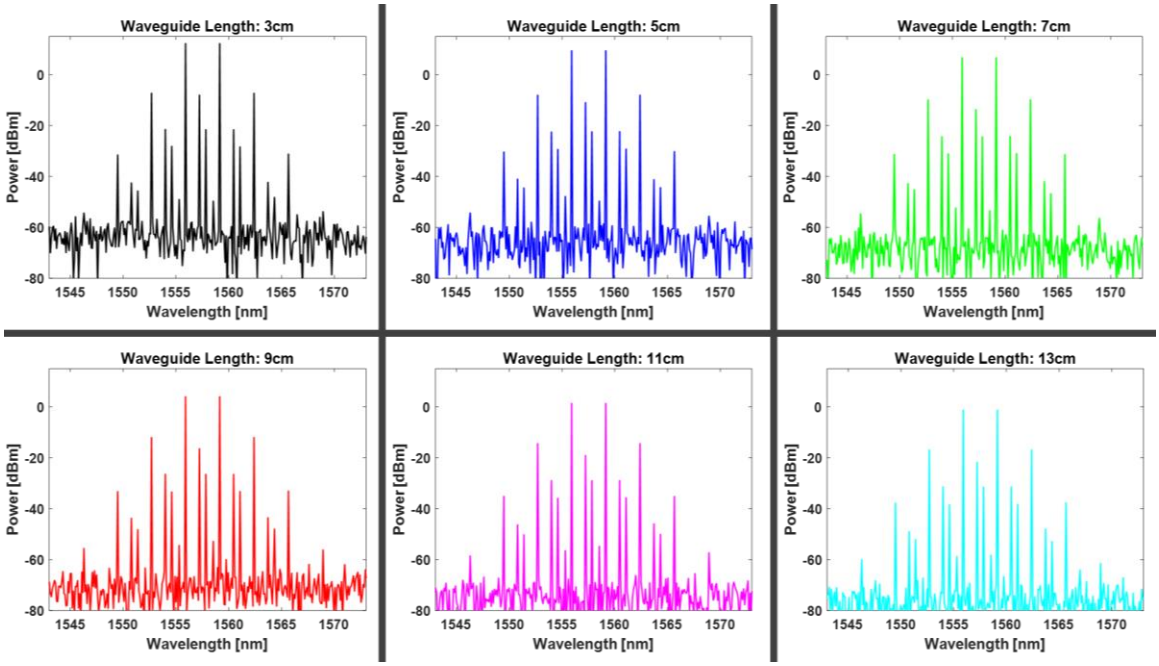

Figure 5.4 Nonlinear mixing output spectra for various waveguide lengths.

To quantify this limitation, we extract the conversion efficiency of the 1st-order idlers (Figure 5.3 (b), P1+P2-S, 2*P1-S, P2-P1+S) and the mixing loss and plotted them as a function of silicon waveguide lengths in Figure 5.5 (a) and (b), separately. The plots show that with waveguide length increasing from 5 cm to 13 cm, the conversion efficiency only improves by 1.8 dB while the loss increases by >10 dB, indicating that nonlinear mixing efficiency cannot be improved purely by elongating the silicon waveguide. Worse, any attempt to compensate for the waveguide loss by increasing the pump power will be negated by corresponding increase of nonlinear loss mediated by TPA and absorption by residual free carriers.

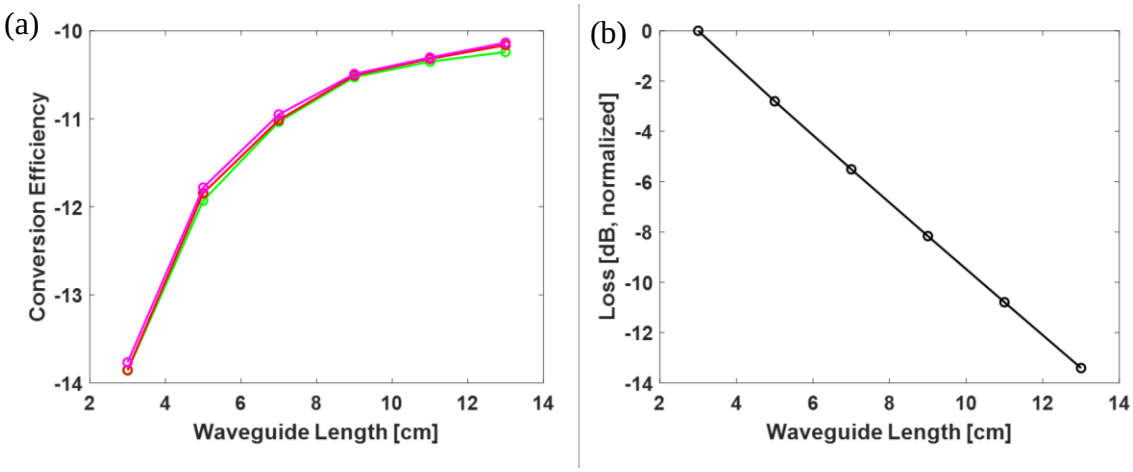

Figure 5.5 Conversion efficiency of the 1st-order idlers (a), and loss (b) versus waveguide length.

Recognizing these challenges, we propose a multi-stage mixer architecture in silicon waveguide which relieves the loss constraint by interstitial re-amplification, and stage-wise dispersion engineering to enhance nonlinear mixing efficiency. The concept is illustrated in Figure 5.6: two distinct pump waves plus the signal initially mix in the first waveguide, immediately followed by a gain block to compensate for the loss inside the first waveguide. Afterwards, a dispersive element is inserted before relaunching it into the second waveguide to realign the phases of all constituent waves, including the pumps,

signal, and idlers generated in the first waveguide, to optimize the generation efficiency for cascaded mixing in the second waveguide. The mixing-reamplification-phase alignment construct can be further cascaded to improve the end-stage mixing efficiency.

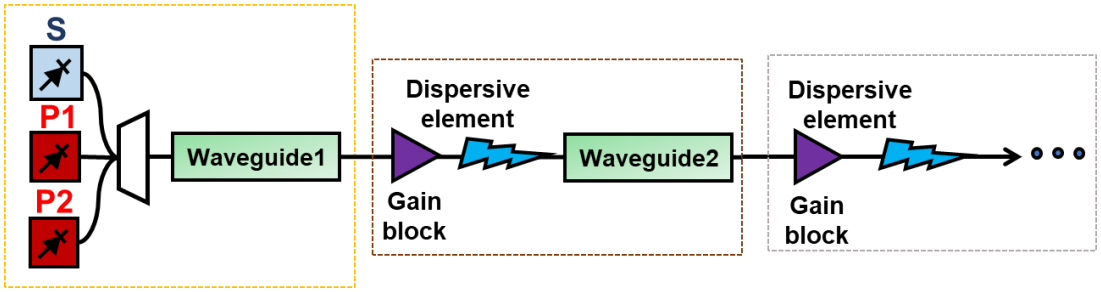

Figure 5.6 Schematic of the proposed multi-stage mixing architecture.

As an illustration of the importance of the inter-stage dispersion engineering, Figure 5.7 (a) and (b) show the simulated output spectra of two waveguide stages (13 cm + 7 cm) without and with dispersion engineering, separately. The input field to the first stage is the same as shown in Figure 5.3 (a). The power is reamplified to 20 dBm before being coupled to the second stage. A clear expansion of output spectral width is observed with the dispersion engineering, as it can aligns the phase of the output from the 1st stage and compress the pulse to reach higher peak power (see Figure 5.8).

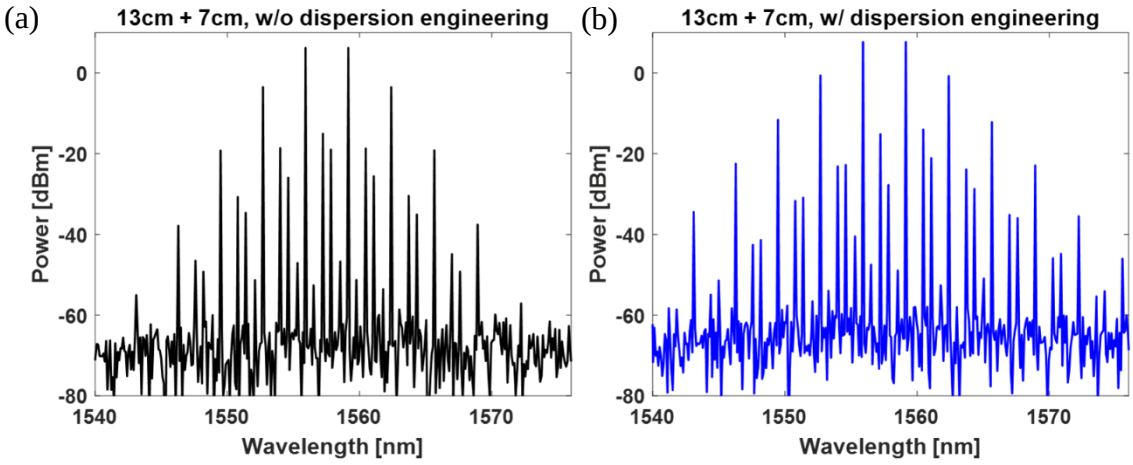

Figure 5.7 Two-stage mixing output spectra w/o (a) and w/ (b) inter-stage dispersion engineering.

As the input pulse propagates in the 1st-stage of silicon waveguide with a nonlinear refractive index, it will encounter nonlinear spectral broadening. With the existence of waveguide dispersion, the temporal profile is also modified. Pulse compression can then be accomplished by using the dispersive element, which compensates for the chirp induced by nonlinear mixing and brings different optical frequency components into synchronism, resulting in both shorter and more intense pulses that facilitate higher mixing efficiency in the following stages. Figure 5.8 plot the time domain pulses with (a) and without (b) dispersion compensation, clearly showing the pulse compression and peak-power improvement with the dispersion engineering.

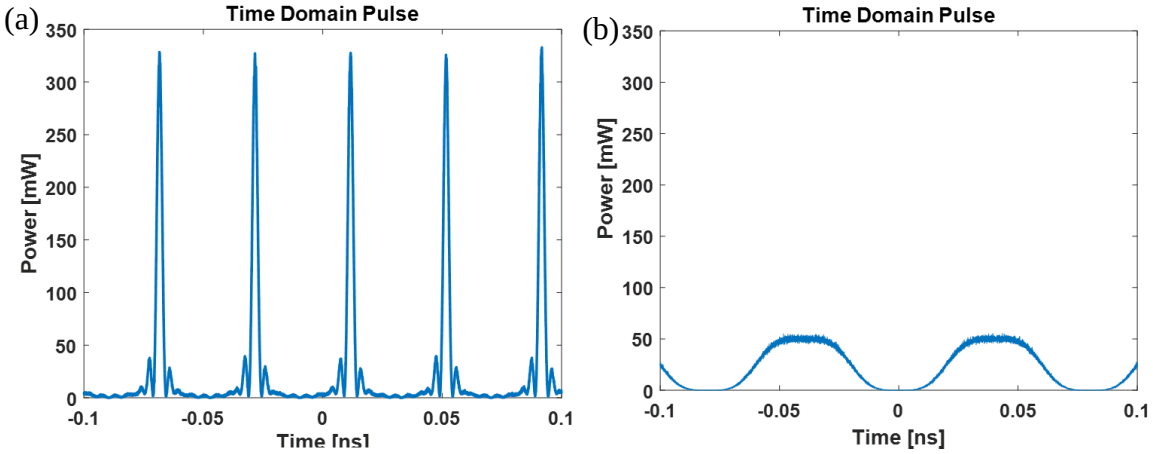

Figure 5.8 Time domain pulses with (a) and without (b) dispersion compression.

To further illustrate the concept of multi-stage mixing, we calculated the output spectrum of various stage constructions from 2 to 5 and plotted the output mixing spectrum in Figure 5.9. For all the calculations, the output of the former stage is reamplified to 20 dBm and dispersion compensated before being coupled into the next stage. Furthermore, we use the 20-dB variation of conversion efficiency as a counting criteria and extract the quantities of the multicast copies. As depicted by the scaling law in Figure 5.9 (b), the

number of copies will keep growing in an exponential fashion with further increase in the number of stages, promising a fully scalable mixing scheme.

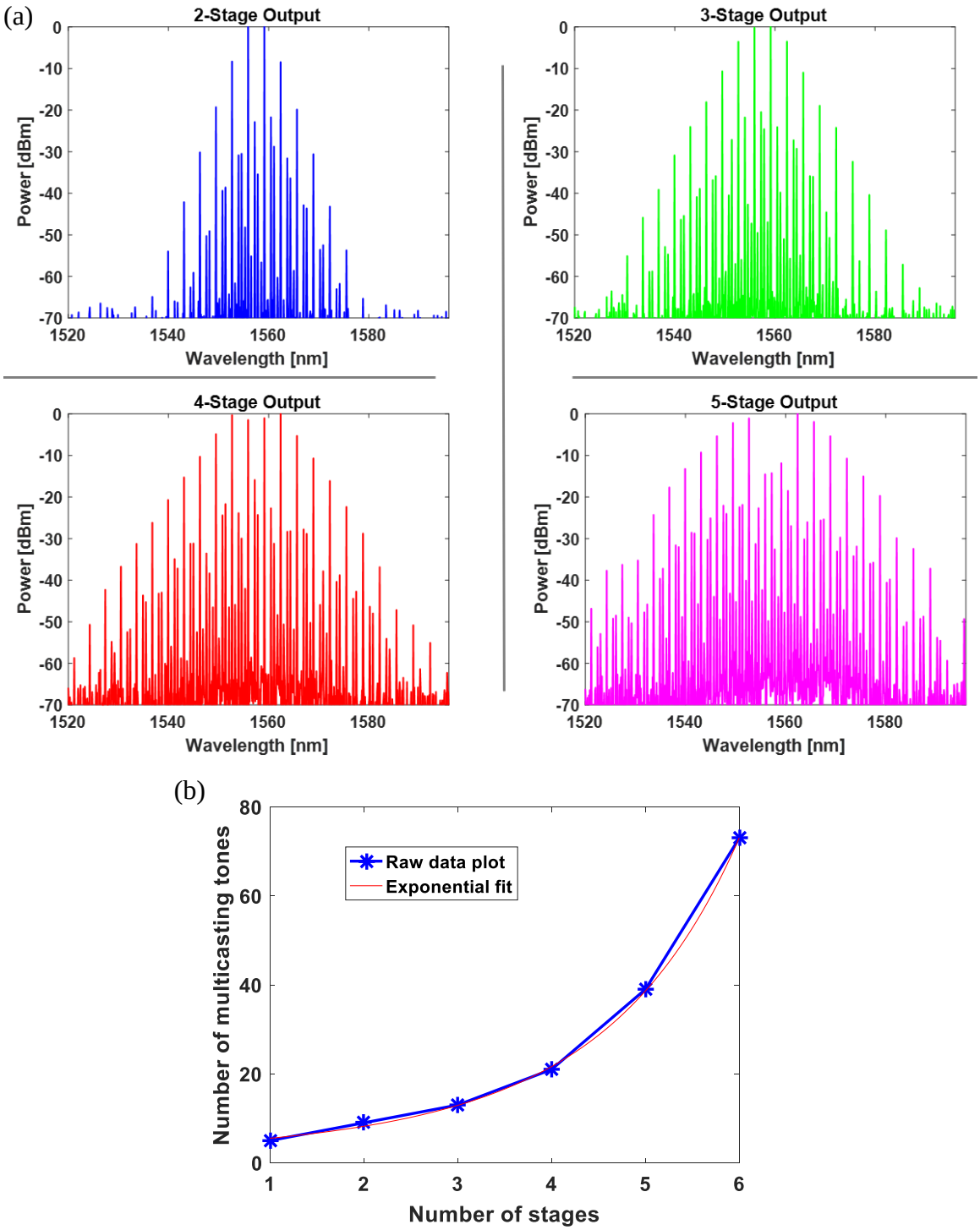

Figure 5.9 (a) Simulation output of the various waveguide stages from 2 to 5; (b) multicast scaling law with stage numbers.

5.4 Experimental Demonstration

The multicast quality is rigorously characterized in a system experiment in the setup shown in Figure 5.10. Two lasers emitting at 1555.9 nm and 1559.1 nm (i.e. identical to the simulation section above) with 15-kHz linewidths are amplified with EDFAs, multiplexed by a WDM multiplexer, and then combined using a 3 dB coupler with a signal laser at 1557.0 nm. The signal is modulated with 24-Gbaud 4/16-QAM data generated using a 64-GS/s DAC to characterize the multicast quality. The input spectrum coupled to waveguide stage 1 is shown in Figure 5.10 as an inset.

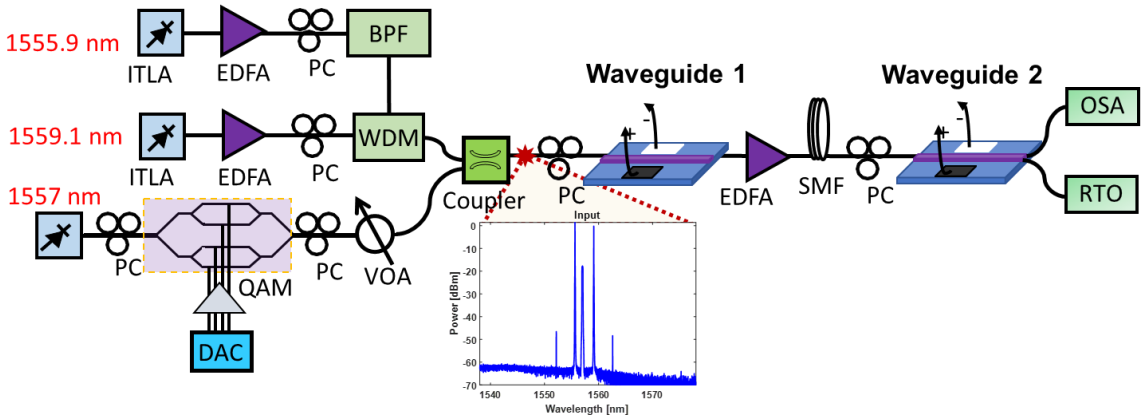

Figure 5.10 Experimental setup (ITLA: integrated tunable laser; PC: polarization controller; BPF: band pass filter; WDM: wavelength division multiplexer; SMF: single-mode fiber; OSA: optical spectrum analyzer, QAM: quadrature-amplitude modulator). Inset shows the spectrum of the input to waveguide 1.

The pumps and signal are coupled into the first-stage silicon waveguide of 13 cm with the aid of a tapered fiber. The waveguide mixers are terminated by inverse tapers at the chip edges for fiber coupling. The fiber-to-chip butt-coupling loss is measured at 5 dB/facet for TE mode. The power coupled to the waveguide per pump is 17 dBm and the coupled signal power is -3 dBm, which are identical to the simulation settings in the former section. The output signal of the first waveguide is amplified using an EDFA to 25 dBm, dispersion compensated by a 5-m-long single mode fiber, and then coupled into the 7-cm

long second-stage waveguide. Taking the 5-dB coupling loss into consideration, the coupled power to the second-stage waveguide is 20 dBm. The p-i-n junctions of both waveguides are reverse biased at 25 V for free-carrier removal to reduce free-carrier induced loss. Finally, the signals are coherently detected relying on a 20 kHz local oscillator and digitized with a real-time oscilloscope. The data are demodulated offline with a standard digital signal processing (DSP) chain using MATLAB [102].

The captures of the experimental spectra at the output of the first stage and the second stage are shown in Figure 5.11 (a) and (b) respectively. The simulation results of the output spectra are plotted on the right side in Figure 5.11 (c) and (d). As apparent from Figure 5.11, the experimental spectra fully coincide with the simulation predictions. The increase in noise level in the second stage is attributed to the significant fiber-to-chip coupling loss, which increases the effective noise figure of the interstitial fiber amplifier correspondingly. The noise can therefore be reduced by replacing the fiber amplifier with a semiconductor optical amplifier (SOA) chip, of which the mode field is better matched with that of the silicon waveguide.

The multicast performance is further quantified in terms of the Q-factors with both 4-QAM and 16-QAM modulation formats for the generated nine idlers (I1-I9 as marked in Figure 5.12 (a)). The extracted Q-factors for the nine multicast copies are plotted in Figure 5.12 (b), showing similar performance variation for both modulation formats, which is a consequence of un-equalized spectral parametric gain, as well as the amplified spontaneous emission (ASE) noise ripple within the bandwidth of interest. The best (Figure 5.13 (a/c)) and worst (Figure 5.13 (b/d)) constellation diagrams in each modulation format (4-QAM or 16-QAM) are shown in Figure 5.13 for a reference.

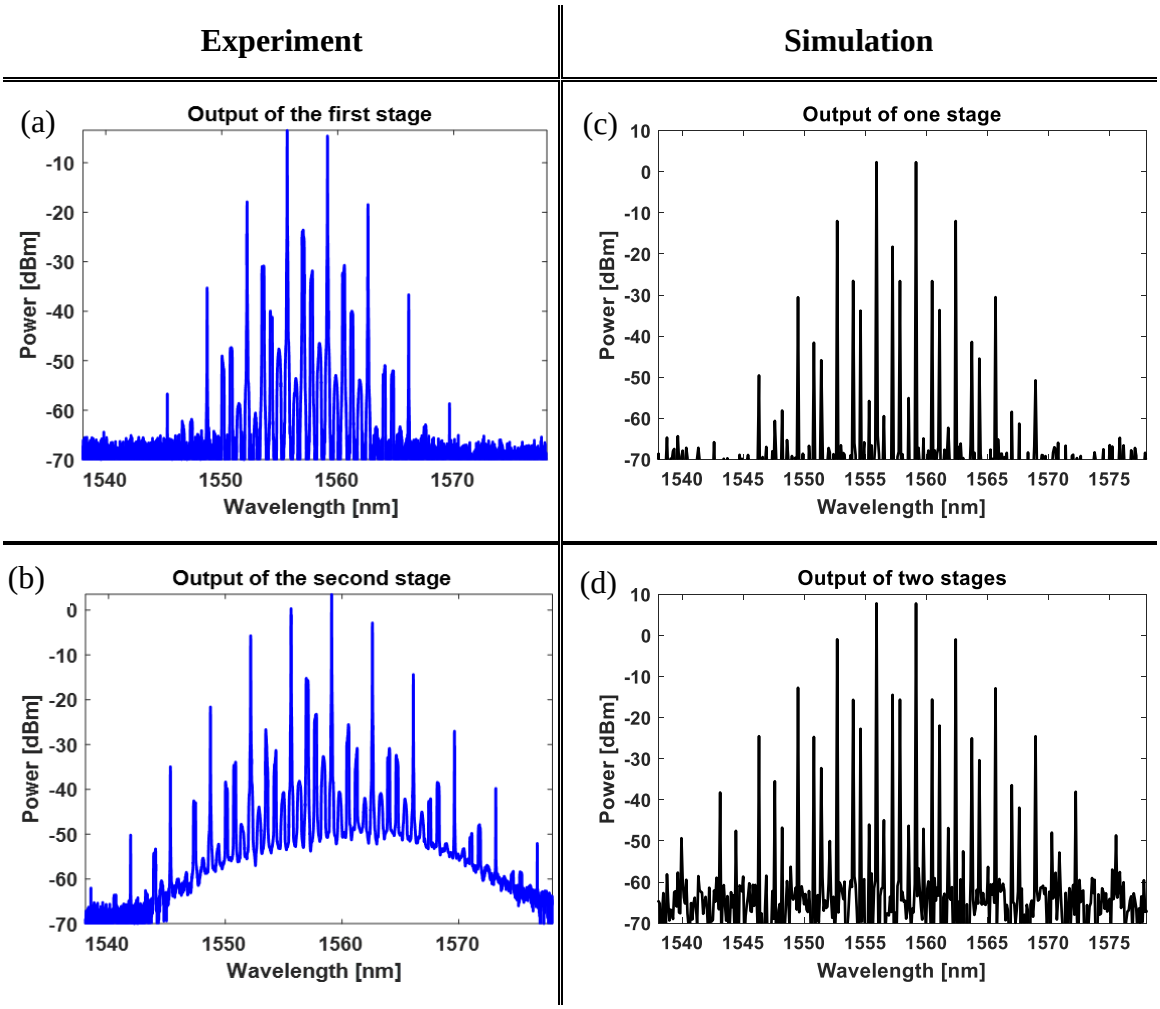

Figure 5.11 Experimental output spectra of the 1st-stage waveguide (a) and the 2nd-stage waveguide (b); modeled output spectra of the 1st-stage waveguide (c) and the 2nd-stage waveguide (d) with the same settings.

To summarize, in this section we have experimentally demonstrated successful QAM multicasting in a silicon-based two-pump multi-stage mixer with inter-stage dispersion management. Nine multicast copies carrying 24-GBaud 4- and 16-QAM data sequences are generated with up to 10 dB variation. While the obtained performance variation requires further device engineering to achieve a more uniform performance [103], it ought to be stressed that, to the best of our knowledge, the presented result represents the first demonstration of a multistage silicon mixer with QAM signals.

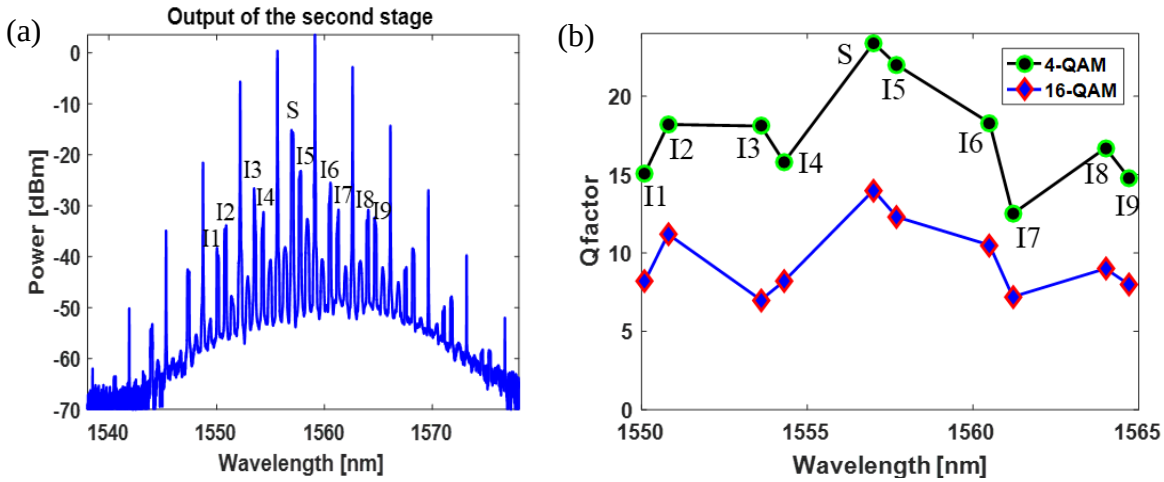

Figure 5.12 (a) Experimental output spectra of the 2nd-stage waveguide with marked idler distributions; (b) Q factors of generated idlers (black: 4-QAM, magenta: 16-QAM).

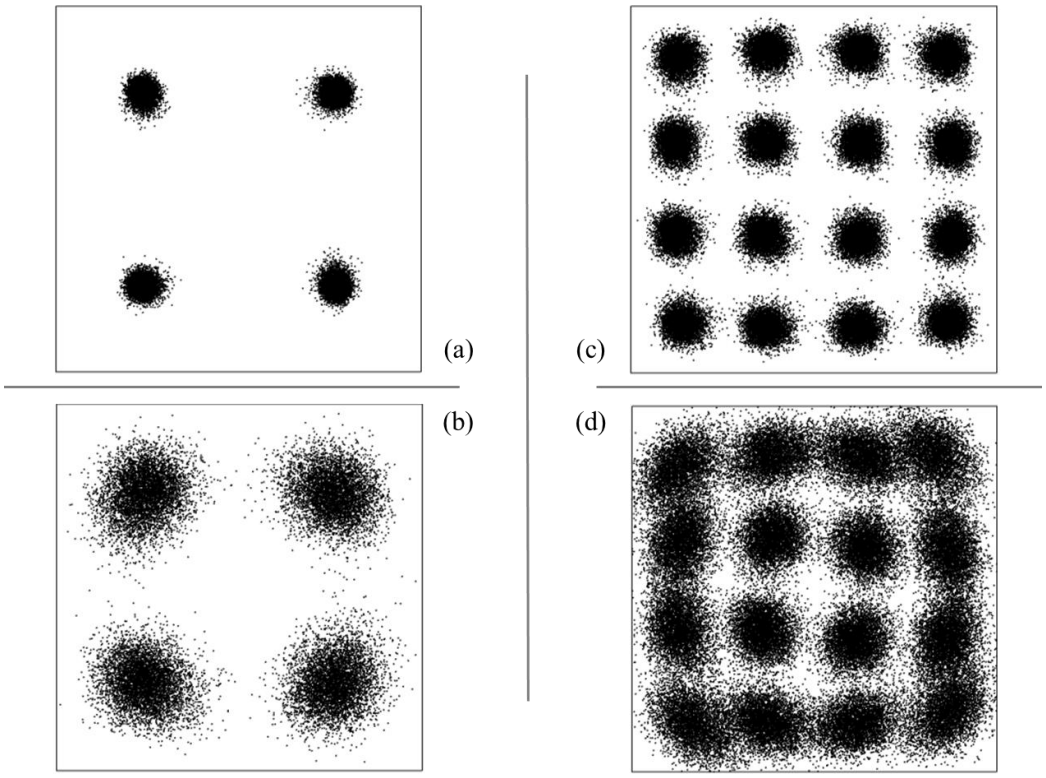

Figure 5.13 The best and worst constellation diagrams for 4QAM and 16QAM modulation.

5.5 Summary

In this chapter we have proposed and demonstrated a novel concept for scalable wavelength multicasting based on multi-stage, loss- and dispersion-managed silicon mixer waveguide. The waveguide design in consideration of nonlinearity and dispersion is introduced, followed by numerical calculations of the proposed multicast concept. Afterwards, we have experimentally demonstrated successful QAM multicasting in a silicon-based two-pump multi-stage mixer with inter-stage dispersion management. Nine multicast copies carrying 24-GBaud 4- and 16-QAM data sequences are generated with up to 10 dB variation. Further comparisons between the experimental results and the numerical simulations show high consistency.

Chapter 5, in part, is a reprint of the material as it appears in Asia Communications and Photonics Conference, pp. ATh2H-5. Optical Society of America, 2016, titled "Wavelength multicasting of 4/16QAM channel in a dual-pump two-stage silicon mixer", by Jin Zhang, E. Temprana, BP-P. Kuo, N. Alic, and S. Radic. The dissertation author was the primary investigator, and the primary author of this article.

Chapter 6 Summary and Outlook

6.1 Summary

As the explosive growth of data traffic continues to increase to drive data centers into the so-called ‘Zettabyte Era’, optical interconnects are becoming more and more attractive for on-chip and short-reach data links. Communication links with high energy efficiency (low power consumption) and high bandwidth density are demanded to meet the requirements for interconnect applications inter- and intra- modern data centers. Silicon photonics based optical interconnects, with the capability to achieve electro-optic co-integration, dense integration, and wavelength division multiplexing, offers a promising solution to achieve a larger bandwidth-distance product, higher interconnect density and better power efficiency compared to their electrical counterparts. This dissertation explores and develops the design and architecture of silicon photonics components for low-power and high-speed optical interconnects.

Wavelength-division multiplexing (WDM) is an important technology enabling multiplication of interconnect capacity, which has been deployed in the current 200GE/400GE port standardizations and is a must for future even-higher rate standards. A WDM system requires, firstly, a multiplexer at the transmitter to join the several signals together and a demultiplexer at the receiver to split them apart. Therefore, a new design of arbitrary ratio multimode interference (MMI) couplers is proposed in Chapter 3 with demonstrated implementations in wideband wavelength multiplexer/demultiplexer (MUX/DEMUX). The limited coupling ratio availability of straight-line MMI couplers is introduced, followed by the theoretical working principle to allow for arbitrary coupling ratio in MMIs. Afterwards, the new design of arbitrary-ratio MMI couplers is proposed,

with dedicated theoretical calculations and numerical simulations showcasing the design optimization process and performance advancements in wavelength and fabrication insensitivity. Multiple chip experimental characterizations with further wavelength and fabrication sensitivity study validate the devices' performance advancements. An application example for wideband wavelength MUX/DEMUX is demonstrated.

An avalanche photodiode (APD) with its internal multiplication gain provides the benefit of improving the sensitivity of the receiver circuits, such that the transmitter power budget is reduced, the transmission distance is elongated, and the demanded gain for the following electric amplifier is relieved, thereby lowing the overall power consumption of the entire link. Together with the capability to support high-bandwidth high-order modulation formats, APD-based receiver offers a potential solution for future interconnect architectures in terms of both energy consumption and bandwidth density. In chapter 4 the design, numerical simulation, and experimental characterizations of APDs are investigated. Furthermore, the APD devices are implemented in transmission link experiments with high-speed high-order modulation formats (32Gbuad PAM4 and 40Gbuad 16QAM), demonstrating performance improvements with APD devices due to the avalanche gain provided.

In Chapter 5, a multi-stage dispersion-engineered wavelength multicast scheme in silicon waveguides is proposed. The waveguide design for nonlinear applications in silicon is introduced, followed by dedicated numerical investigations of a dual-pump-driven parametric mixer in multi-stage silicon waveguides, showing the importance of dispersion synchronization. Experimental demonstrations of a two-stage dual-pump wavelength multicast scheme with 4/16 QAM data modulation further verified the multicast copy

number scalability with multiple waveguide stages and the quality of the multicast copies in terms of Q-factors.

6.2 Future Directions

This dissertation has explored the design and architecture of silicon photonic components, including arbitrary ratio MMI couplers, APDs, and multi-stage silicon waveguide mixer, with demonstrated experimental results facilitating future low-power high-bandwidth optical interconnects; notwithstanding, many open questions yet remain for system-level integration. The sections that follow discuss the possible future directions.

6.2.1 Arbitrary Ratio MMI Couplers

The demonstrations of the newly proposed arbitrary ratio MMI couplers in chapter 3 show advancements in design and fabrication simplicity, broadband working wavelength, and fabrication deviation insensitivity. The application implementations of a two-channel wavelength multiplexer/demultiplexer with two delay stages have been numerically modeled and experimentally demonstrated in section 3.5, however, with only the 29%-8% concatenation scheme in the experimental demonstration. The 71%-92% concatenation circuits with the designed ArMMIs are expected to have a more advanced performances in terms of loss and spectral flatness, thereby need to be further deployed and verified. Moreover, higher-channel-number cascaded Mach-Zehnder wavelength filters with more delay stages also need to be explored to meet the WDM demands.

As for the device design, since the structure of the new design is completely symmetric in the horizontal direction, it is worthy of studying the feasibility of designing the component with a reflected structure from the middle, which, if possible, would further shrink the devices' feature size to half and promise other application potentials.

6.2.2 Ge-on-Si Avalanche Photodiodes

Chapter 4 designs and demonstrates Ge-on-Si APDs with PIN structure that fully rely on the current foundry-provided fabrication process. While the noise of APDs with multiplication gain happened inside Ge is reduced via electric field engineering, it is intriguing to explore the designs with Si serving as the gain material simultaneously with foundry-offered fabrications (without Si epitaxial growth). The structure in Ref [78] serves as a good beginning point, while more efforts need to be taken to distribute the field control layer to achieve a higher bandwidth without damaging the gain performance or posing susceptibility issue of unwanted edge breakdown.

We have demonstrated in section 4.4 for APD PAM4 reception test and in section 4.5 for APD coherent detection experiment, both in a TIA-less fashion. To facilitate applications in an integrated receiver circuit board, a co-designed TIA circuit offers benefits to further improve the receiver dynamic range, whether for PAM4 modulation or for coherent detection.

6.2.3 Multi-stage Silicon Waveguide Mixer

Chapter 5 show the numerically modeled multicast results for the proposed multi-stage silicon mixer, with proof-of-concept experimental demonstrations on a two-stage multicast architect bearing 4/16 QAM modulated data. In our demonstrations, the inter-stage dispersion engineering, which is essential for the efficient and low-noise wavelength multicasting, is realized via off-chip component like single-mode fiber and Bragg grating, as is the gain functionality achieved via off-chip EDFA. This scheme introduces unavoidable coupling loss and is not practically scalable to a large scale. Potential explorations to design on-chip dispersion elements and SOAs (hybrid-integration on

Silicon Photonics) are promising to accomplish fully scalable multicasts with lower noise and less power consumption.

Bibliography

[1] Cisco, “Cisco Annual Internet Report (2018–2023),” Cisco, pp. 1–41, 2020.

[2] Masanet, Eric, Arman Shehabi, Nuoa Lei, Sarah Smith, and Jonathan Koomey. "Recalibrating global data center energy-use estimates." Science 367, no. 6481 (2020): 984-986.

[3] Andrae, Anders SG, and Tomas Edler. "On global electricity usage of communication technology: trends to 2030." Challenges 6, no. 1 (2015): 117-157.

[4] Dhoedt, Bart, Roel Baets, Peter Van Daele, Paul Heremans, Jan Van Campenhout, J. Hall, R. Michalzik et al. "Optically interconnected integrated circuits to solve the CMOS interconnect bottleneck." In 1998 Proceedings. 48th Electronic Components and Technology Conference (Cat. No. 98CH36206), pp. 992-998. IEEE, 1998.

[5] Nagarajan, Radhakrishnan, Masaki Kato, Jacco Pleumeekers, Peter Evans, Scott Corzine, Sheila Hurtt, Andrew Dentai et al. "InP photonic integrated circuits." IEEE Journal of Selected Topics in Quantum Electronics 16, no. 5 (2010): 1113-1125.

[6] Romero-García, Sebastian, Florian Merget, Frank Zhong, Hod Finkelstein, and Jeremy Witzens. "Silicon nitride CMOS-compatible platform for integrated photonics applications at visible wavelengths." Optics express 21, no. 12 (2013): 14036-14046.

[7] Mayer, Aline S., and Blair C. Kirkpatrick. "Silicon photonics." Frontiers in Modern Optics 190 (2016): 189-205.

[8] Thomson, David, Aaron Zilkie, John E. Bowers, Tin Komljenovic, Graham T. Reed, Laurent Vivien, Delphine Marris-Morini et al. "Roadmap on silicon photonics." Journal of Optics 18, no. 7 (2016): 073003.

[9] “LightCounting Integrated Optical Devices Report,” 6th Ed., 2020.

[10] Zhu, Yixiao, Fan Zhang, Fan Yang, Lei Zhang, Xiaoke Ruan, Yanping Li, and Zhangyuan Chen. "Toward Single Lane 200G Optical Interconnects With Silicon Photonic Modulator." Journal of Lightwave Technology 38, no. 1 (2019): 67-74.

[11] Sun, Jie, Ranjeet Kumar, Meer Sakib, Jeffrey B. Driscoll, Hasitha Jayatilleka, and Haisheng Rong. "A 128 Gb/s PAM4 silicon microring modulator with integrated thermo-optic resonance tuning." Journal of Lightwave Technology 37, no. 1 (2019): 110-115.

[12] Vivien, Laurent, Johann Osmond, Jean-Marc Fédéli, Delphine Marris-Morini, Paul Crozat, Jean-François Damlencourt, Eric Cassan, Y. Lecunff, and Suzanne Laval. "42 GHz pin Germanium photodetector integrated in a silicon-on-insulator waveguide." Optics express 17, no. 8 (2009): 6252-6257.

[13] Michel, Jurgen, Jifeng Liu, and Lionel C. Kimerling. "High-performance Ge-on-Si photodetectors." Nature photonics 4, no. 8 (2010): 527-534.

[14] Horst, Folkert, William MJ Green, Solomon Assefa, Steven M. Shank, Yurii A. Vlasov, and Bert Jan Offrein. "Cascaded Mach-Zehnder wavelength filters in silicon photonics for low loss and flat pass-band WDM (de-) multiplexing." Optics express 21, no. 10 (2013): 11652-11658.

[15] Pathak, Shibnath, Michael Vanslembrouck, Pieter Dumon, Dries Van Thourhout, and Wim Bogaerts. "Optimized silicon AWG with flattened spectral response using an MMI aperture." Journal of Lightwave Technology 31, no. 1 (2013): 87-93.

[16] Zhou, Zhiping, Bing Yin, and Jurgen Michel. "On-chip light sources for silicon photonics." Light: Science & Applications 4, no. 11 (2015): e358.

[17] Komljenovic, Tin, Duanni Huang, Paolo Pintus, Minh A. Tran, Michael L. Davenport, and John E. Bowers. "Photonic integrated circuits using heterogeneous integration on silicon." Proceedings of the IEEE 106, no. 12 (2018): 2246-2257.

[18] Griffith, Austin G., Ryan KW Lau, Jaime Cardenas, Yoshitomo Okawachi, Aseema Mohanty, Romy Fain, Yoon Ho Daniel Lee et al. "Silicon-chip mid-infrared frequency comb generation." Nature communications 6, no. 1 (2015): 1-5.

[19] Kuyken, Bart, Takuro Ideguchi, Simon Holzner, Ming Yan, Theodor W. Hänsch, Joris Van Campenhout, Peter Verheyen et al. "An octave-spanning mid-infrared frequency comb generated in a silicon nanophotonic wire waveguide." Nature communications 6, no. 1 (2015): 1-6.

[20] Xu, Yelong, Jiachuan Lin, Raphaël Dubé-Demers, Sophie LaRochelle, Leslie Rusch, and Wei Shi. "Integrated flexible-grid WDM transmitter using an optical frequency comb in microring modulators." Optics letters 43, no. 7 (2018): 1554-1557.

[21] Lin, Jiachuan, Hassan Sepehrian, Yelong Xu, Leslie A. Rusch, and Wei Shi. "Frequency comb generation using a CMOS compatible SiP DD-MZM for flexible networks." IEEE Photonics Technology Letters 30, no. 17 (2018): 1495-1498.

[22] Cheng, Qixiang, Meisam Bahadori, Madeleine Glick, Sébastien Rumley, and Keren Bergman. "Recent advances in optical technologies for data centers: a review." Optica 5, no. 11 (2018): 1354-1370.

[23] Huang, Zhihong, Cheng Li, Di Liang, Kunzhi Yu, Charles Santori, Marco Fiorentino, Wayne Sorin, Samuel Palermo, and Raymond G. Beausoleil. "25 Gbps low-voltage waveguide Si–Ge avalanche photodiode." Optica 3, no. 8 (2016): 793-798.

[24] Zarkesh-Ha, Payman, Robert Efroymson, Earl Fuller, Joe C. Campbell, and Majeed M. Hayat. "5.2 dB Sensitivity Enhancement in 25Gbps APD-Based Optical Receiver Using Dynamic Biasing." In Optical Fiber Communication Conference, pp. Th3J-2. Optical Society of America, 2020.

[25] Cardenas, Jaime, Carl B. Poitras, Kevin Luke, Lian-Wee Luo, Paul Adrian Morton, and Michal Lipson. "High coupling efficiency etched facet tapers in silicon waveguides." IEEE Photonics Technology Letters 26, no. 23 (2014): 2380-2382.

[26] Dangel, Roger, Jens Hofrichter, Folkert Horst, Daniel Jubin, Antonio La Porta,

Norbert Meier, Ibrahim Murat Soganci, Jonas Weiss, and Bert Jan Offrein. "Polymer waveguides for electro-optical integration in data centers and high-performance computers." Optics express 23, no. 4 (2015): 4736-4750.

[27] Subbaraman, Harish, Xiaochuan Xu, Amir Hosseini, Xingyu Zhang, Yang Zhang, David Kwong, and Ray T. Chen. "Recent advances in silicon-based passive and active optical interconnects." Optics express 23, no. 3 (2015): 2487-2511.

[28] Han, Liangshun, Bill P-P. Kuo, Motohiko Eto, Ana Pejkic, Jin Zhang, Nikola Alic, and Stojan Radic. "Silicon Photonic 50GHz Wavelength (De) Multiplexer with Low Crosstalk and Flat Passband." In CLEO: Science and Innovations, pp. STu4B-3. Optical Society of America, 2018.

[29] Fandiño, Javier S., Pascual Muñoz, David Doménech, and José Capmany. "A monolithic integrated photonic microwave filter." Nature Photonics 11, no. 2 (2017): 124-129.

[30] Van Campenhout, Joris, William MJ Green, Solomon Assefa, and Yurii A. Vlasov. "Low-power, 2× 2 silicon electro-optic switch with 110-nm bandwidth for broadband reconfigurable optical networks." Optics Express 17, no. 26 (2009): 24020-24029.

[31] Akihama, Yuta, and Kazuhiro Hane. "Single and multiple optical switches that use freestanding silicon nanowire waveguide couplers." Light: Science & Applications 1, no. 6 (2012): e16-e16.

[32] Marcuse, Dietrich. Theory of dielectric optical waveguides. Elsevier, 2013.

[33] Prinzen, Andreas, Jens Bolten, Michael Waldow, and Heinrich Kurz. "Study on fabrication tolerances of SOI based directional couplers and ring resonators." Microelectronic engineering 121 (2014): 51-54.

[34] Bachmann, Maurus, Pierre A. Besse, and Hans Melchior. "General self-imaging properties in N× N multimode interference couplers including phase relations." Applied optics 33, no. 18 (1994): 3905-3911.

[35] Soldano, Lucas B., and Erik CM Pennings. "Optical multi-mode interference devices based on self-imaging: principles and applications." Journal of lightwave technology 13, no. 4 (1995): 615-627.

[36] Bachmann, M., P. A. Besse, and H. Melchior. "Overlapping-image multimode interference couplers with a reduced number of self-images for uniform and nonuniform power splitting." Applied optics 34, no. 30 (1995): 6898-6910.

[37] Besse, Pierre A., Emilio Gini, Maurus Bachmann, and Hans Melchior. "New 2/spl times/2 and 1/spl times/3 multimode interference couplers with free selection of power splitting ratios." Journal of Lightwave Technology 14, no. 10 (1996): 2286-2293.

[38] Doménech, José David, Javier S. Fandino, Bernardo Gargallo, and Pascual Munoz. "Arbitrary coupling ratio multimode interference couplers in silicon-on-insulator." Journal of lightwave technology 32, no. 14 (2014): 2536-2543.

[39] Leuthold, Juerg, and Charles H. Joyner. "Multimode interference couplers with tunable power splitting ratios." Journal of lightwave technology 19, no. 5 (2001): 700.

[40] Nagai, Shuichi, Goh Morishima, Hirokazu Inayoshi, and Katsuyuki Utaka. "Multimode interference photonic switches (MIPS)." Journal of Lightwave Technology 20, no. 4 (2002): 675-681.

[41] Tseng, Shuo-Yen, Canek Fuentes-Hernandez, Daniel Owens, and Bernard Kippelen. "Variable splitting ratio 2× 2 MMI couplers using multimode waveguide holograms." Optics express 15, no. 14 (2007): 9015-9021.

[42] Saida, Takashi, Akira Himeno, Masayuki Okuno, Akio Sugita, and Katsunari Okamoto. "Silica-based 2/spl times/2 multimode interference coupler with arbitrary power splitting ratio." Electronics Letters 35, no. 23 (1999): 2031-2033.

[43] Feng, David JY, and T. S. Lay. "Compact multimode interference couplers with arbitrary power splitting ratio." Optics Express 16, no. 10 (2008): 7175-7180.

[44] Cherchi, Matteo, Sami Ylinen, Mikko Harjanne, Markku Kapulainen, Tapani Vehmas, and Timo Aalto. "Unconstrained splitting ratios in compact double-MMI couplers." Optics express 22, no. 8 (2014): 9245-9253.

[45] Lai, Q., M. Bachmann, W. Hunziker, P. A. Besse, and H. Melchior. "Arbitrary ratio power splitters using angled silica on silicon multimode interference couplers." Electronics Letters 32, no. 17 (1996): 1576-1577.

[46] Levy, David S., Y. M. Li, Robert Scarmozzino, and R. M. Osgood. "A multimode interference-based variable power splitter in GaAs-AlGaAs." IEEE Photonics Technology Letters 9, no. 10 (1997): 1373-1375.

[47] Lagali, N. S., M. R. Paiam, and R. I. MacDonald. "Theory of variable-ratio power splitters using multimode interference couplers." IEEE Photonics Technology Letters 11, no. 6 (1999): 665-667.

[48] Levy, David S., Y. M. Li, Robert Scarmozzino, and R. M. Osgood. "A multimode interference-based variable power splitter in GaAs-AlGaAs." IEEE Photonics Technology Letters 9, no. 10 (1997): 1373-1375.

[49] Hanfoug, Rabah, L. M. Augustin, Yohan Barbarin, J. J. G. M. Van der Tol, E. A. J. M. Bente, Fouad Karouta, D. Rogers et al. "Reduced reflections from multimode interference couplers." Electronics letters 42, no. 8 (2006): 465-466.

[50] Besse, Pierre A., Maurus Bachmann, Hans Melchior, Lucas B. Soldano, and Meint K. Smit. "Optical bandwidth and fabrication tolerances of multimode interference couplers." Journal of Lightwave Technology 12, no. 6 (1994): 1004-1009.

[51] Hill, Martin T., X. J. M. Leijtens, G. D. Khoe, and M. K. Smit. "Optimizing imbalance and loss in 2× 2 3-dB multimode interference couplers via access waveguide width." Journal of lightwave technology 21, no. 10 (2003): 2305-2313.

[52] Halir, Robert, Günther Roelkens, A. Ortega-Moñux, and J. G. Wangüemert-Pérez.

"High-performance 90 hybrid based on a silicon-on-insulator multimode interference coupler." Optics letters 36, no. 2 (2011): 178-180.

[53] Horikawa, Tsuyoshi, Daisuke Shimura, Seok-Hwan Jeong, Masatoshi Tokushima, Keizo Kinoshita, and Tohru Mogami. "The impacts of fabrication error in Si wire-waveguides on spectral variation of coupled resonator optical waveguides." Microelectronic Engineering 156 (2016): 46-49.

[54] Lu, Zeqin, Han Yun, Yun Wang, Zhitian Chen, Fan Zhang, Nicolas AF Jaeger, and Lukas Chrostowski. "Broadband silicon photonic directional coupler using asymmetric-waveguide based phase control." Optics express 23, no. 3 (2015): 3795-3808.

[55] Forrest, S. R. "Sensitivity of avalanche photodetector receivers for high-bit-rate long-wavelength optical communication systems." In Semiconductors and Semimetals, vol. 22, pp. 329-387. Elsevier, 1985.

[56] Maes, W., K. De Meyer, and R. Van Overstraeten. "Impact ionization in silicon: A review and update." Solid-State Electronics 33, no. 6 (1990): 705-718.

[57] Capasso, Federico. "Physics of avalanche photodiodes." In Semiconductors and semimetals, vol. 22, pp. 1-172. Elsevier, 1985.

[58] Chynoweth, A. G. "Ionization rates for electrons and holes in silicon." physical review 109, no. 5 (1958): 1537.

[59] McIntyre, R. J. "Multiplication noise in uniform avalanche diodes." IEEE Transactions on Electron Devices 1 (1966): 164-168.

[60] Assefa, Solomon, Fengnian Xia, and Yurii A. Vlasov. "Reinventing germanium avalanche photodetector for nanophotonic on-chip optical interconnects." Nature 464, no. 7285 (2010): 80-84.

[61] Hayat, Majeed M., Oh-Hyun Kwon, Shuling Wang, Joe C. Campbell, Bahaa EA Saleh, and Malvin C. Teich. "Boundary effects on multiplication noise in thin heterostructure avalanche photodiodes: theory and experiment [Al/sub 0.6/Ga/sub 0.4/As/GaAs]." IEEE Transactions on Electron Devices 49, no. 12 (2002): 2114-2123.

[62] McIntyre, Robert J. "The distribution of gains in uniformly multiplying avalanche photodiodes: Theory." IEEE Transactions on Electron Devices 19, no. 6 (1972): 703-713.

[63] Kang, Yimin, Han-Din Liu, Mike Morse, Mario J. Paniccia, Moshe Zadka, Stas Litski, Gadi Sarid et al. "Monolithic germanium/silicon avalanche photodiodes with 340 GHz gain–bandwidth product." Nature photonics 3, no. 1 (2009): 59-63.

[64] Emmons, R. B. "Avalanche-photodiode frequency response." Journal of Applied Physics 38, no. 9 (1967): 3705-3714.

[65] Van Overstraeten, R., and H. De Man. "Measurement of the ionization rates in diffused silicon pn junctions." Solid-State Electronics 13, no. 5 (1970): 583-608.

[66] Decker, D. R., and C. N. Dunn. "Determination of germanium ionization coefficients from small-signal IMPATT diode characteristics." IEEE Transactions on Electron Devices 17, no. 4 (1970): 290-299.

[67] Liu, Jifeng, Douglas D. Cannon, Kazumi Wada, Yasuhiko Ishikawa, David T. Danielson, Samerkhae Jongthammanurak, Jurgen Michel, and Lionel C. Kimerling. "Deformation potential constants of biaxially tensile stressed Ge epitaxial films on Si (100)." Physical Review B 70, no. 15 (2004): 155309.

[68] Campbell, Joe C., Stephane Demiguel, Feng Ma, Ariane Beck, Xiangyi Guo, Shuling Wang, Xiaoguang Zheng et al. "Recent advances in avalanche photodiodes." IEEE Journal of selected topics in quantum electronics 10, no. 4 (2004): 777-787.

[69] Tan, Chee Hing, John PR David, J. Clark, Graham J. Rees, S. A. Plimmer, David J. Robbins, David C. Herbert, Roger Timothy Carline, and Weng Y. Leong. "Avalanche multiplication and noise in submicron Si pin diodes." In Silicon-based Optoelectronics II, vol. 3953, pp. 95-102. International Society for Optics and Photonics, 2000.

[70] Huang, Mengyuan, Tuo Shi, Pengfei Cai, Liangbo Wang, Su Li, Wang Chen, Ching-yin Hong, and Dong Pan. "25Gb/s normal incident Ge/Si avalanche photodiode." In 2014 The European Conference on Optical Communication (ECOC), pp. 1-3. IEEE, 2014.

[71] Huang, Mengyuan, Su Li, Pengfei Cai, Guanghui Hou, Tzung-I. Su, Wang Chen, Ching-yin Hong, and Dong Pan. "Germanium on silicon avalanche photodiode." IEEE Journal of Selected Topics in Quantum Electronics 24, no. 2 (2017): 1-11.

[72] Kishino, Katsumi, M. Selim Unlu, J-I. Chyi, J. Reed, L. Arsenault, and Hadis Morkoc. "Resonant cavity-enhanced (RCE) photodetectors." IEEE Journal of Quantum Electronics 27, no. 8 (1991): 2025-2034.

[73] Huang, Zhihong, Cheng Li, Di Liang, Kunzhi Yu, Charles Santori, Marco Fiorentino, Wayne Sorin, Samuel Palermo, and Raymond G. Beausoleil. "25 Gbps low-voltage waveguide Si–Ge avalanche photodiode." Optica 3, no. 8 (2016): 793-798.

[74] Park, Sungbong, Yann Malinge, Olufemi Dosunmu, Gregory Lovell, Seth Slavin, Kelly Magruder, Yimin Kang, and Ansheng Liu. "50-Gbps receiver subsystem using Ge/Si avalanche photodiode and integrated bypass capacitor." In 2019 Optical Fiber Communications Conference and Exhibition (OFC), pp. 1-3. IEEE, 2019.

[75] Wang, Binhao, Zhihong Huang, Xiaoge Zeng, Di Liang, Marco Fiorentino, Wayne V. Sorin, and Raymond G. Beausoleil. "50 Gb/s PAM4 low-voltage Si-Ge avalanche photodiode." In CLEO: Science and Innovations, pp. SM4J-7. Optical Society of America, 2019.

[76] Huang, Zhihong, Binhao Wang, Yuan Yuan, Di Liang, Marco Fiorentino, and Raymond G. Beausoleil. "64Gbps PAM4 Modulation for a Low Energy Si-Ge Waveguide APD with Distributed Bragg Reflectors." In Optical Fiber

Communication Conference, pp. W4G-8. Optical Society of America, 2020.

[77] Yuan, Yuan, Zhihong Huang, Binhao Wang, Wayne Sorin, Di Liang, Joe C. Campbell, and Raymond G. Beausoleil. "Superior Temperature Performance of Si-Ge Waveguide Avalanche Photodiodes at 64Gbps PAM4 Operation." In 2020 Optical Fiber Communications Conference and Exhibition (OFC), pp. 1-3. IEEE, 2020.

[78] Martinez, Nicholas JD, Christopher T. Derose, Reinhard W. Brock, Andrew L. Starbuck, Andrew T. Pomerene, Anthony L. Lentine, Douglas C. Trotter, and Paul S. Davids. "High performance waveguide-coupled Ge-on-Si linear mode avalanche photodiodes." Optics Express 24, no. 17 (2016): 19072-19081.

[79] Lim, Andy Eu-Jin, Junfeng Song, Qing Fang, Chao Li, Xiaoguang Tu, Ning Duan, Kok Kiong Chen, Roger Poh-Cher Tern, and Tsung-Yang Liow. "Review of silicon photonics foundry efforts." IEEE Journal of Selected Topics in Quantum Electronics 20, no. 4 (2013): 405-416.

[80] Melchior, H., and W. T. Lynch. "Signal and noise response of high speed germanium avalanche photodiodes." IEEE Transactions on Electron Devices 12 (1966): 829-838.

[81] Virot, Léopold, Paul Crozat, Jean-Marc Fédéli, Jean-Michel Hartmann, Delphine Marris-Morini, Eric Cassan, Frédéric Boeuf, and Laurent Vivien. "Germanium avalanche receiver for low power interconnects." Nature communications 5, no. 1 (2014): 1-6.

[82] Chen, H. T., Jochem Verbist, P. Verheyen, P. De Heyn, G. Lepage, J. De Coster, P. Absil et al. "High sensitivity 10Gb/s Si photonic receiver based on a low-voltage waveguide-coupled Ge avalanche photodetector." Optics express 23, no. 2 (2015): 815-822.

[83] Teich, M., Kuniaki Matsuo, and B. Saleh. "Excess noise factors for conventional and superlattice avalanche photodiodes and photomultiplier tubes." IEEE journal of quantum electronics 22, no. 8 (1986): 1184-1193.

[84] Hayat, Majeed M., Winslow L. Sargeant, and Bahaa EA Saleh. "Effect of dead space on gain and noise in Si and GaAs avalanche photodiodes." IEEE journal of quantum electronics 28, no. 5 (1992): 1360-1365.

[85] Ip, Ezra, Alan Pak Tao Lau, Daniel JF Barros, and Joseph M. Kahn. "Coherent detection in optical fiber systems." Optics express 16, no. 2 (2008): 753-791.

[86] Kikuchi, Kazuro. "Fundamentals of coherent optical fiber communications." Journal of Lightwave Technology 34, no. 1 (2015): 157-179.

[87] Wen, Ke, Yanli Zhao, Jing Gao, Shibo Zhang, and Junjie Tu. "Design of a coherent receiver based on InAs electron avalanche photodiode for free-space optical communications." IEEE Transactions on Electron Devices 62, no. 6 (2015): 1932-1938.

[88] Zhang, Bo, Christian Malouin, and Theodore J. Schmidt. "Design of coherent

receiver optical front end for unamplified applications." Optics express 20, no. 3 (2012): 3225-3234.

[89] Smith, Benjamin P., Arash Farhood, Andrew Hunt, Frank R. Kschischang, and John Lodge. "Staircase codes: FEC for 100 Gb/s OTN." Journal of Lightwave Technology 30, no. 1 (2011): 110-117.

[90] Sahasrabuddhe, Laxman H., and Biswanath Mukherjee. "Light trees: optical multicasting for improved performance in wavelength routed networks." IEEE Communications Magazine 37, no. 2 (1999): 67-73.

[91] Liu, Lan, Eduardo Temprana, Vahid Ataie, Andreas OJ Wiberg, Bill P-P. Kuo, Evgeny Myslivets, Nikola Alic, and Stojan Radic. "All optical wavelength multicaster and regenerator based on four-mode phase-sensitive parametric mixer." Optics express 23, no. 24 (2015): 30956-30969.

[92] Contestabile, Giampiero, Akihiro Maruta, Shigeaki Sekiguchi, Ken Morito, Mitsuru Sugawara, and Ken-ichi Kitayama. "All-optical wavelength multicasting in a QD-SOA." IEEE Journal of Quantum Electronics 47, no. 4 (2011): 541-547.

[93] Biberman, Aleksandr, Benjamin G. Lee, Amy C. Turner-Foster, Mark A. Foster, Michal Lipson, Alexander L. Gaeta, and Keren Bergman. "Wavelength multicasting in silicon photonic nanowires." Optics express 18, no. 17 (2010): 18047-18055.

[94] Chagnon, Mathieu, Mina Spasojevic, Rhys Adams, Jia Li, David V. Plant, and Lawrence R. Chen. "Wavelength multicasting at 22-gbaud 16-QAM in a silicon nanowire using four-wave mixing." IEEE Photonics Technology Letters 27, no. 8 (2015): 860-863.

[95] Dinu, M., Francesco Quochi, and H. Garcia. "Third-order nonlinearities in silicon at telecom wavelengths." Applied physics letters 82, no. 18 (2003): 2954-2956.

[96] Lin, Qiang, J. Zhang, Giovanni Piredda, Robert W. Boyd, Philippe M. Fauchet, and Govind P. Agrawal. "Dispersion of silicon nonlinearities in the near infrared region." Applied physics letters 91, no. 2 (2007): 021111.

[97] Agrawal, Govind P. "Nonlinear fiber optics." In Nonlinear Science at the Dawn of the 21st Century, pp. 195-211. Springer, Berlin, Heidelberg, 2000.

[98] Stoffa, P. L., Jacob T. Fokkema, R. M. de Luna Freire, and W. P. Kessinger. "Split-step Fourier migration." Geophysics 55, no. 4 (1990): 410-421.

[99] Ong, Jun Rong, Ranjeet Kumar, and Shayan Mookherjea. "Efficient continuous-wave four-wave mixing in SOI waveguides with active carrier removal." In CLEO: 2013, pp. 1-2. IEEE, 2013.

[100] Myslivets, Evgeny, Bill PP Kuo, Nikola Alic, and Stojan Radic. "Generation of wideband frequency combs by continuous-wave seeding of multistage mixers with synthesized dispersion." Optics express 20, no. 3 (2012): 3331-3344.

[101] McKinstrie, Colin J., Stojan Radic, and Andrew R. Chraplyvy. "Parametric amplifiers driven by two pump waves." IEEE Journal of Selected Topics in

Quantum Electronics 8, no. 3 (2002): 538-547.

[102] Savory, Seb J. "Digital filters for coherent optical receivers." Optics express 16, no. 2 (2008): 804-817.

[103] Kuo, Bill P-P., Evgeny Myslivets, Nikola Alic, and Stojan Radic. "Wavelength multicasting via frequency comb generation in a bandwidth-enhanced fiber optical parametric mixer." Journal of lightwave technology 29, no. 23 (2011): 3515-3522.